A VOLTAGE CONTRAST DETECTOR
FOR USE IN THE
SCANNING ELECTRON MICROSCOPE

by

Terry M. Black

A Thesis submitted to the University of Ottawa in candidature for the degree of Masters of Applied Science.

September, 1973

Department of Electrical Engineering
University of Ottawa
Ottawa, Ontario

917.123'04'2 F5707
MacGregor, James G., 1905-
Pack saddles to Tête Jaune Cache/ James G. MacGregor. – Edmonton: Hurtig Publishers, 1973, c1962.
256 p.: maps; 20 cm.
Pioneer life in the foothills of the Rocky Mountains.
ISBN 0 88830 066 2: $7.95
1. Frontier and pioneer life—Alberta.
1. Pionniers et défricheurs—Alberta.
I. Title.
Full name: James Grierson MacGregor.
C73-3368

NL 9-73

"Knowledge is a process of piling up facts: wisdom lies in their simplification."

Martin H. Fischer

This is to certify that the work contained in this thesis has not already been accepted in substance for any degree and is not being concurrently submitted in candidature for any other degree.

....

Terry M. Black

ACKNOWLEDGEMENTS

I would like to thank Professor P. M. Thompson for his liberal guidance as Faculty Advisor throughout my M.A.Sc. Program.

I am also very grateful to Dr. D. A. Shaw for the subject of this thesis and the many hours spent in discussion and guidance during the research portion of my Program.

The assistance and cooperation of the Communications Research Centre throughout my Program is greatly appreciated.

Thanks must also go to Miss Wendy Simmons and Mrs. Pat Braun for typing this thesis.

Finally, I would like to express my sincere appreciation to my wife, Jamie, for the last four years of support and encouragement during my undergraduate and graduate programs.

CONTENTS

CHAPTER ONE

Introduction

1.1 General Introduction

In any complex system the overall behavior can be governed entirely by the properties of a very small part. This applies whether the system is biological, zoological, mechanical or electronic. A great deal of scientific and technological effort today is devoted to the study and understanding of such "microsystems" in an attempt to improve both performance and reliability. This trend is most dramatically observed in the electronics industry. The development of the integrated circuit is a fine example. Devices are becoming smaller and smaller and today a silicon chip a tenth of an inch square may contain well over 1000 seperate electronic components. As the individual devices become smaller the complexity of the integrated circuits becomes greater and the widespread use of large scale integration is just beginning. Design, production and testing on such a microscopic scale has called for new techniques and instruments capable of working within the tolerances required.

As the size of devices decreases, it becomes more difficult to perform voltage measurements on the individual devices to ensure that they are operating correctly. In the case of the smallest devices it is impossible to mechanically contact the device and use conventional measurement techniques.

In this chapter, the techniques presently used by industry to perform such voltage measurements are described. The advantages and disadvantages of these standard techniques are discussed and a new technique using the electron beam of a scanning electron microscope as a measuring probe is also introduced.

1.2 Surface Voltage Measurement Techniques

During the production of an integrated circuit, there are two occasions when an operational check on the performance of the circuit should be carried out. The first is after the pilot-production run to check the design and

and fabrication procedures. The second is on a continuing sample basis to monitor the quality and repeatability of the established product process technique. These measurement are performed presently using very small mechanical probes which are brought into contact with the metallic pads of the circuit.

The process of probing is straightforward in principle. The silicon wafer, containing several hundred dice, or individual circuits, is placed on a mechanical stage and is held in place by a vacuum. The wafer is then oriented and aligned with the axes of the movable stage using a microscope and mechanical adjustment consisting of either micrometers or stepping motors. A separate mechanical support holds up to 20 or more tungsten probes arranged in a pattern corresponding to the contact regions of a single circuit die in the wafer. The tips of these probes are electrolytically etched to a very fine radius a fraction of thousandth of an inch in diameter. When the alignment is correct for a single circuit die, the probes are lowered and brought into contact with the die and the measurements performed. After the measurements are complete, the probe array is lifted and the next ciruit is moved into position and the process repeated. Figure 1.1 shows an example of a multi-probe system.

Probing circuit dice in this way requires the use of sophisticated optical, mechanical and electrical equipment. It is laborious and time consuming and hence expensive. The probes inflict the minimum amount of damage on the contact pads on the die while still maintaining adequate contact pressure and area to ensure reliable measurements. Excessive pressure can result in the metallisation, (which is typically only .5μ thick) being scratched or even removed entirely.

Improper probing can reduce the reliability of the completed circuit because scratches on the metallisation will reduce its effective cross sectional

FIG. 1.1

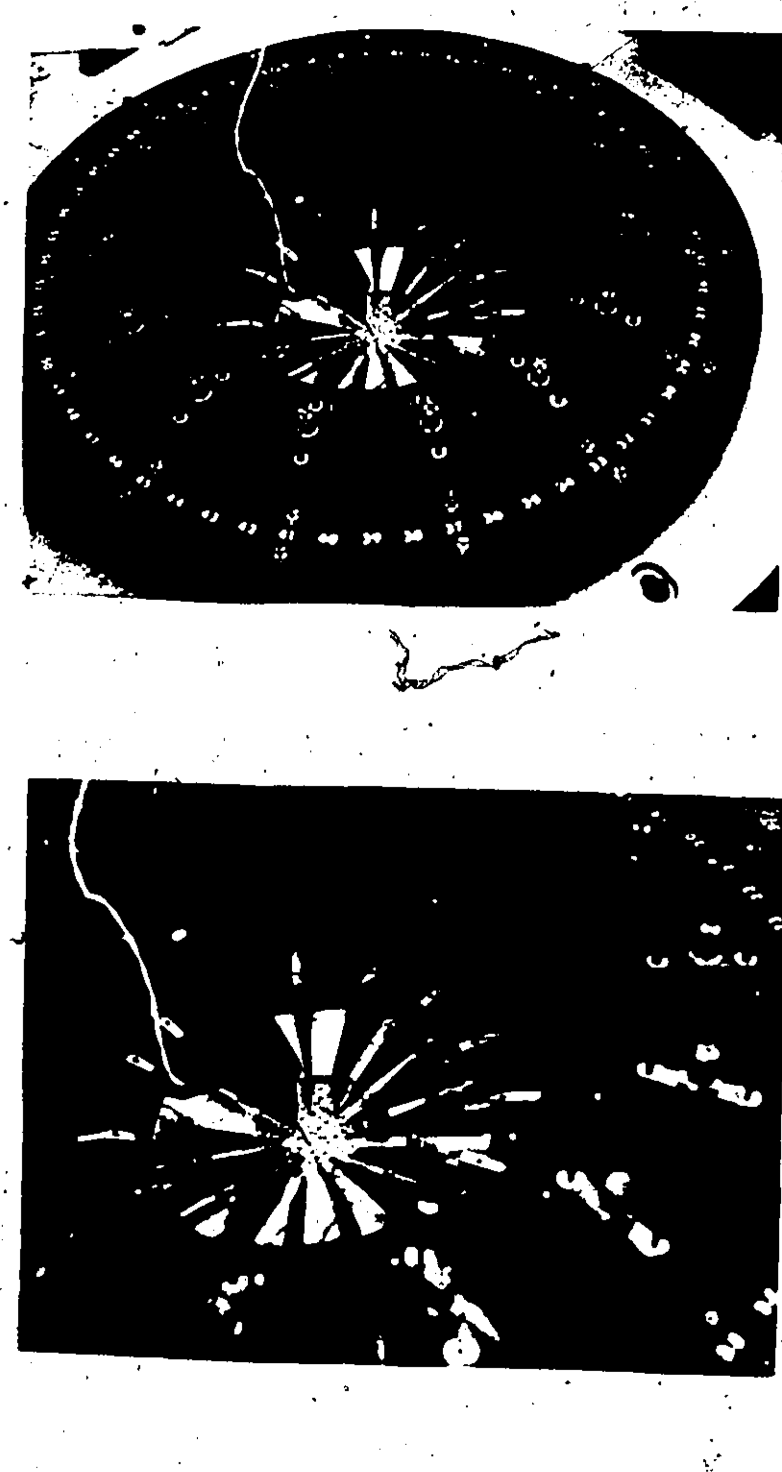

Fig. 1.1

These photographs show typical mechanical probes used to contact the pads of metallization on an I.C. for purposes of measuring the potentials on these pads.

area and, although the circuit may still function normally and pass all electrical tests, the reduced cross section of the metal may lead to overheating due to its higher local resistance. This can increase the rate of electromigration due to increased current density and temperature, leading to premature failure of the device.

Possible damage to the metallization makes it difficult to use a probe to measure potentials on areas other than the bonding pads themselves. It is therefore difficult to obtain operating voltage data for every component in the circuit. Such data would be invaluable for checking that the circuit was operating correctly.

Other problems associated with probing are the usual difficulties of measuring high-frequency characteristics with long leads and large stray capacitances. In addition, the small diameter tungsten probes have an appreciable series resistance and a variable contact resistance to the die being probed. This may result in the erroneous characterization of the packaged circuit or even the rejection of a good die.

1.3 The Use of an Electron Beam as a Measuring Probe

The problems associated with the probing technique are now obvious; the main problems are device damage and the inability to obtain all the important voltage data reliably.

In the production of integrated circuits, the bonding and packaging of the individual die is the most expensive process. It is therefore desirable to measure the performance parameters in the wafer stage of production, before the wafers are cut, mounted, bonded and packaged. An array of probes is therefore needed in order to apply the operating potentials, via the bonding pads, to the unbonded die. If this technique is used with care, then little or no damage will be inflected on the bonding pads. In addition, a moveable probe, capable of being positioned anywhere on the circuit could be used to perform voltage measurements so that all the required data could be collected, not merely the data from the input and output terminals i.e. the bonding pads. It is proposed that an electron beam be used as the moveable probe.

An electron beam can be steered at very high speeds and with great precision by the use of suitable deflection systems. In addition, it cannot inflict mechanical damage on the circuit metallisation. Many signal outputs are generated when an electron beam strikes a metallic or semiconductor target. Among these are, secondary electron emission, backscattered electrons, light, X-rays and internally generated currents. If a suitable detector could be developed to detect variations in surface potential via one of these signal outputs then a very powerful voltage probing system could be produced. The electron beam can be moved through a sequence of measurement points by programming the deflection coil excitation. In this way, the whole process could be computer controlled and a very high throughput of devices attained. It is anticipated that this type of system will eventually be used for production monitoring as well as in the research laboratory.

Such a measuring system must also be designed to meet specifications that are required of any measuring instrument, such as accuracy, linearity, range, sensitivity and response time.

This thesis is concerned with the development of such a "voltage sensitive detection system" which can be used in a scanning electron microscope (SEM). The next chapter describes the operation of the SEM and the various signal outputs generated. Chapter Three reviews the published work on voltage sensitive detectors and introduces the concept of the new detection system which is the main subject of this thesis. The following chapters analyse the operation of the new detector and describe the results obtained from the test units.

CHAPTER TWO

Secondary Electron Emission and the Scanning Electron Microscope

Introduction

In this chapter the structure and general operation of the scanning electron microscope (SEM) are outlined. First of all however, a brief study of electron beam-solid interactions is presented and the emission of secondary electrons and their angular and energy distributions are discussed. This is basic to the description of the SEM and its modes of operation which follow. The chapter concludes by introducing the basic idea of voltage contrast and some of the factors which contribute to it.

2.1 Electron-Solid Interactions

When a high energy electron impinges on a material, it penetrates the surface to a depth dependent on the incident-energy of the electron and the atomic number of the material. As the incident or primary electron enters the specimen lattice, it may take part in an elastic or inelastic collision. If the former occurs, the direction of motion of the primary electron is altered but no energy transfer occurs. The primary electron may be deflected further into the specimen where it will take part in yet another collision, or, it can be deflected out of the specimen and be emitted as a backscattered primary electron with an energy close to or equal to that of the incident electron.

If an inelastic collision occurs, the host atom is ionized and the primary electron looses energy. This process, which generates hole-electron pairs free to drift through the material lattice, is an avalanche process with a great many pairs being produced by one incident electron. The electrons produced can diffuse through the specimen losing energy in further ionization processes until they have insufficient energy to cause further ionization or until they reach the surface. If, upon reaching the surface, an electron has sufficient energy to overcome the surface barrier work function, it can be emitted as a secondary electron with an energy of up to 50 eV or as a tertiary electron with an energy ranging from 50 eV up to the primary electron energy. The value of 50 eV is somewhat arbitrary but is usually chosen as the upper bound of those electrons known as secondary electrons, electrons generated from the ionization process. Figure 2.1 shows this distribution of emitted electrons schematically. Under the influence of a beam of energetic electrons, a volume containing many hole-electron pairs is created. This is called a plasma. Murata et al. (2.1) have theoretically determined the shape of this plasma by tracing the paths of incident electrons as they are scattered through the specimen. These results are shown in Figure 2.2. The effect of specimen atomic number and angle of primary beam incidence on the shape and depth of the induced plasma can be seen. As the specimen atomic number increases, the plasma is generated closer to the surface. Also, as the primary beam incidence angle is varied from 0 to 45^{o}, the shape of the plasma is tilted. These effects are basic to the emissive mode of operation of the SEM which is discussed in section 2.4.

Murata et al. (2.1) have also shown that the number of secondary and backscattered electrons emitted per second is related to their absorption by the specimen. Generally speaking, secondary electrons come from a depth of less than 500 Å and backscattered electrons from a depth of 1000 Å to 1μ. This is shown schematically in Figure 2.3.

2.2 Secondary Electron Emission

This section considers the emission of secondary electrons in more detail. The secondary electron yield, the angular distribution and energy distribution are discussed.

2.2.1 The Secondary Electron Yield

The most widely investigated property of secondary electron emission is the yield as a function of primary electron energy. Secondary electron yield, δ, is defined as the number of secondary electrons emitted per incident primary electron. The graph of δ vs. the primary beam energy, E_p, is known as the yield curve and has the same general shape for most materials, i.e., for low values of E_p, δ is much less than unity; it increases with E_p to a maximum value, δ_m, and then decreases slowly as

FIG. 2.1

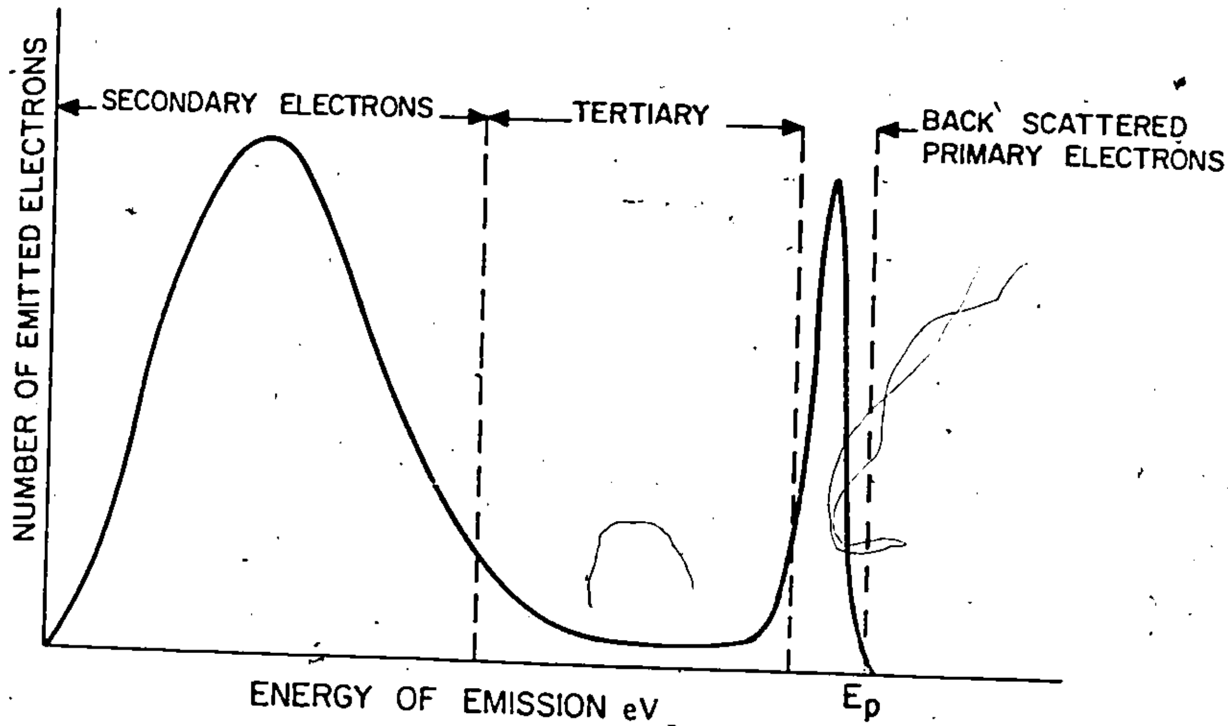
NUMBER OF EMITTED ELECTRONS
SECONDARY ELECTRONS
TERTIARY
BACK SCATTERED PRIMARY ELECTRONS
ENERGY OF EMISSION eV
E_p

Fig. 2.1

This graph shows the energy distribution of emitted electrons created when a high energy beam impinges the surface of a solid specimen.

FIG. 2.2

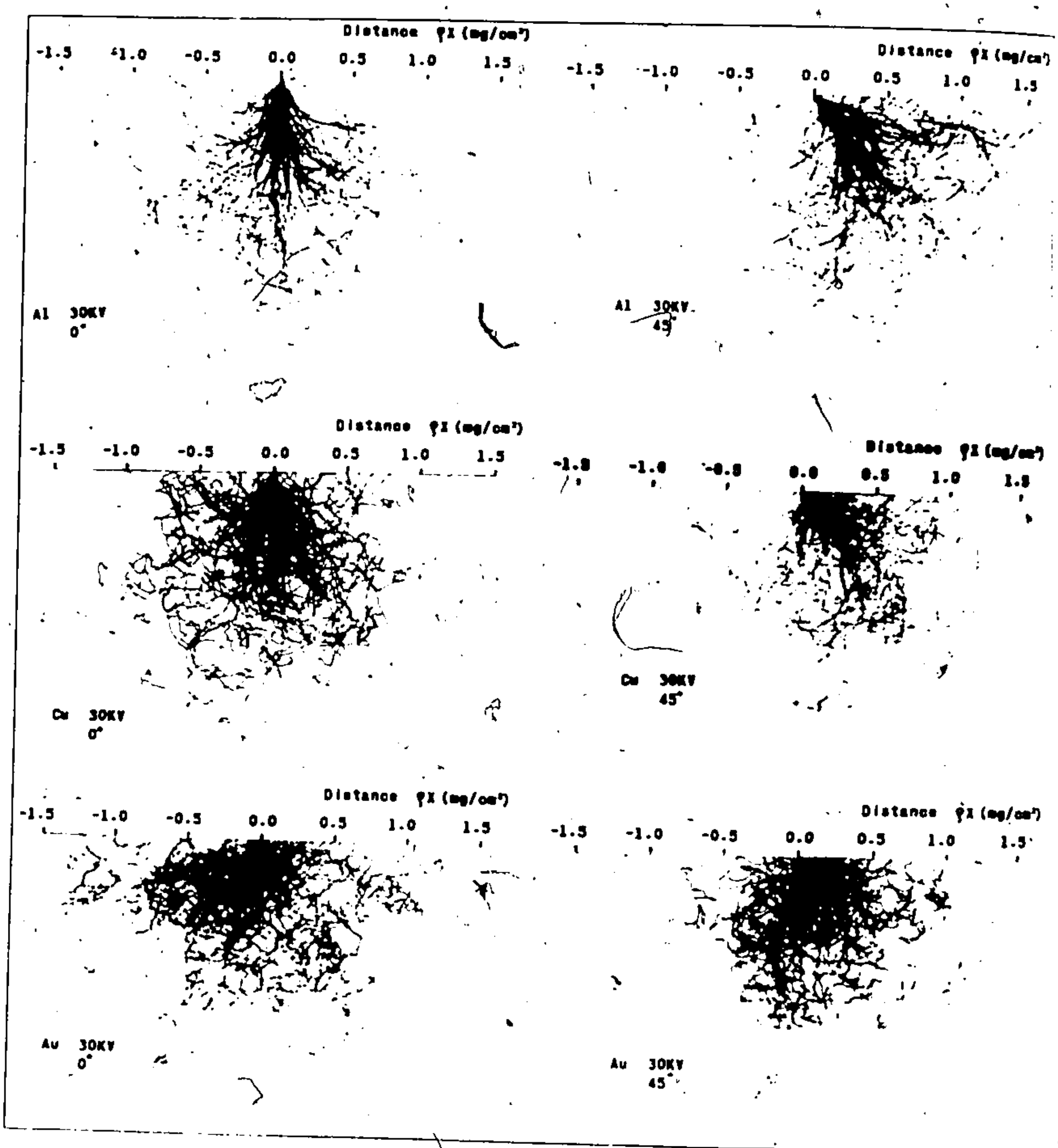
Distance ρX (mg/cm²)
-1.5 -1.0 -0.5 0.0 0.5 1.0 1.5
Al 30KV
0°
Al 30KV
45°
Cu 30KV
0°
Cu 30KV
45°
Au 30KV
0°
Au 30KV
45°

Fig. 2.2

The results obtained by Murata on electron tracing of incident electrons in a solid are shown here. The variations on the plasma shape resulting from variations in primary beam incident angle and specimen atomic number are illustrated.

FIG. 2.3

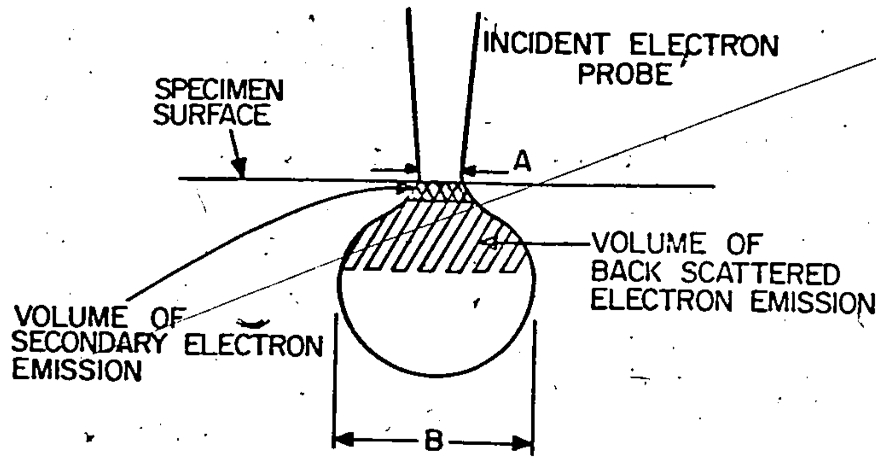

A : EFFECTIVE AREA OF EMISSION OF SECONDARY ELECTRONS
B : " " " " " BACK SCATTERED ELECTRONS

FIG. 2.4

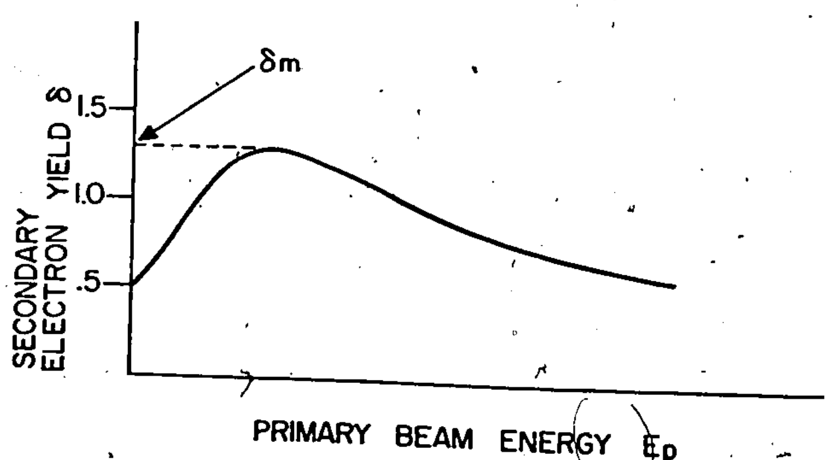

Fig. 2.3

An ionized plasma is created within a solid specimen when irradiated by high energy electrons. The relative depths of generation of the three groups of emitted electrons and the "tear drop" shape of the plasma are evident here.

Fig. 2.4

The number of secondary electrons emitted per primary electron, depends on the energy of the primary electron. This is referred to as the secondary electron yield $\delta(E)$.

E_p is further increased. This is shown schematically in Figure 2.4. The value of δ_m and the primary beam energy at which it occurs, depends on the specimen material and to a greater extent on surface contamination. Many workers have attempted to overcome these problems in the determination of δ_m for different materials but with little success. However, some experimental values of δ_m and the beam energy at which it occurs have been obtained (2.2,2.3,2.4). The value of δ_m for Al is 1.0 and it occurs at an energy of 300 eV while that of Si is 1.1 and it occurs at 250 eV. Two factors which affect the yield of secondary electrons are surface work function and crystal structure.

De Boer and Bruining (2.5) have calculated that changes in surface work function contribute only slightly to changes in secondary electron yield. Experimental results obtained by Sixtus and Troloan (6,7) on surface absorbed layers showed a systematic increase in yield as the surface work function was decreased. Although the results show that the yield does depend on the surface work function, what is most significant is the relatively minor role that work function plays in governing the shape of the yield curve.

Sufficient experimental results have been obtained to show a dependence of the secondary electron yield on the crystal structure of the specimen. Knoll and Theile (2.8) showed that secondary electron yield variations ranging from .1 to 30% occured for changes in specimen crystal structure. Although a relationship has been shown to exist between yield and crystal structure, detailed data on this is lacking.

The majority of electron yield experiments have been conducted using a normal primary beam incidence. However, as mentioned briefly in section 2.1, the yield varies with primary beam incidence angle. As this angle of incidence, θ, measured from the normal increases, secondaries are generated closer to the surface and thus have less chance of being absorbed before they reach the surface. Bruining (2.9,2.10) assumed that secondary electrons are absorbed exponentially with distance. He derived an expression for the secondary electron yield at an incidence angle θ, $\delta(\theta)$ in the form

$$\delta(\theta) = \delta e^{\alpha X_m(1 - \cos\theta)}$$

where δ is the yield at normal incidence, Xm is the mean depth of secondary electron generation and α is the coefficient of absorption of secondary electrons. This expression has been verified experimentally to within 20% and when presented in a normalized form has the shape shown in Figure 2.5.

2.2.2 The Angular Distribution of Secondary Electron Emission

Past and recent work (2.11,2.12,2.13,2.14) on the angular distribution of the number of secondary electrons emitted is in agreement that the number of secondary electrons emitted per unit solid angle is greatest in the direction normal to the emitting surface and decreases with increasing angle of emergence ϕ as cos ϕ. This is independent of the angle of incidence of the primary beam. Based on these references and referring to Figure 2.6, if N' is the number of secondary electrons emitted per unit solid angle in the direction normal to the surface, then the number per unit solid angle at the angle ϕ, $N(\phi)$ is given by

$$N(\phi) = N'\cos\phi.$$

The number emitted between the curves of semi-angle ϕ and $\phi + d\phi$ is given by the product of $N(\phi)$ and the solid angle involved. This is the solid angle subtended at the point of emission by the annular strip of area $2\pi r \sin\phi \, r d\phi$ on the hemisphere of radius r described above the point of emission in Figure 2.6. Hence the solid angle is $2\pi \sin\phi d\phi$ and the number of electrons emitted into it is given by

$$dN = N'\cos\phi . \, 2\pi \sin\phi d\phi.$$

The number emitted into a cone of semi-angle ϕ' is given by

$$N_{\phi'} = 2\pi N' \int_0^{\phi'} \cos\phi \sin\phi d\phi$$

and the total number emitted is found by putting $\phi' = \pi/2$, i. e. Total number emitted $= \pi N'$. From these expressions the number of secondary electrons emitted into any cone angle can be computed.

2.2.3 The Energy Distribution of Secondary Electrons

The energy distribution of emitted secondary electrons has been carefully documented with data obtained for different materials. According to Becker

FIG. 2.5

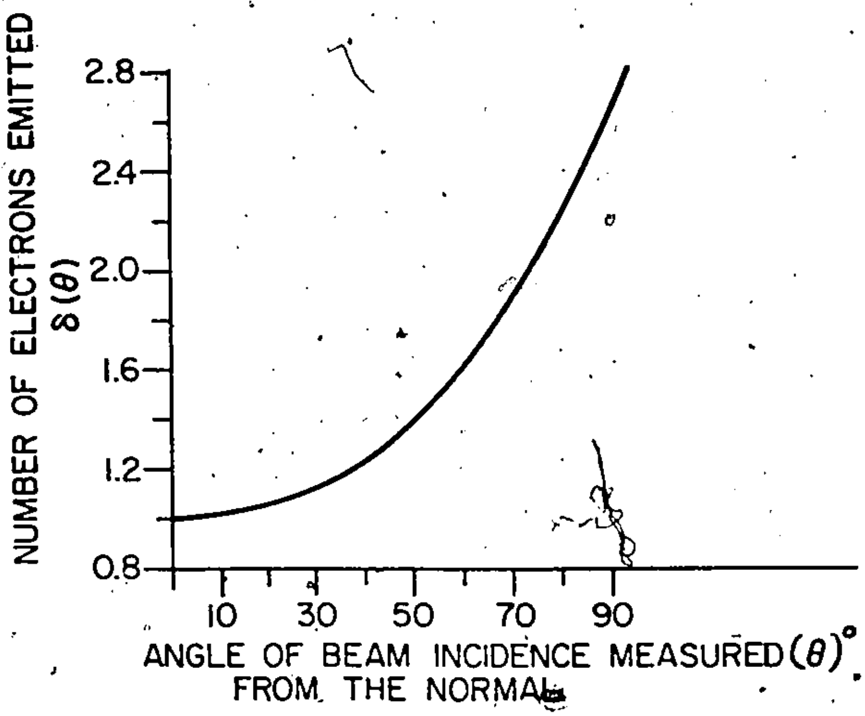
NUMBER OF ELECTRONS EMITTED
δ(θ)
2.8
2.4
2.0
1.6
1.2
0.8
10
30
50
70
90
ANGLE OF BEAM INCIDENCE MEASURED (θ)°
FROM THE NORMAL

FIG. 2.6

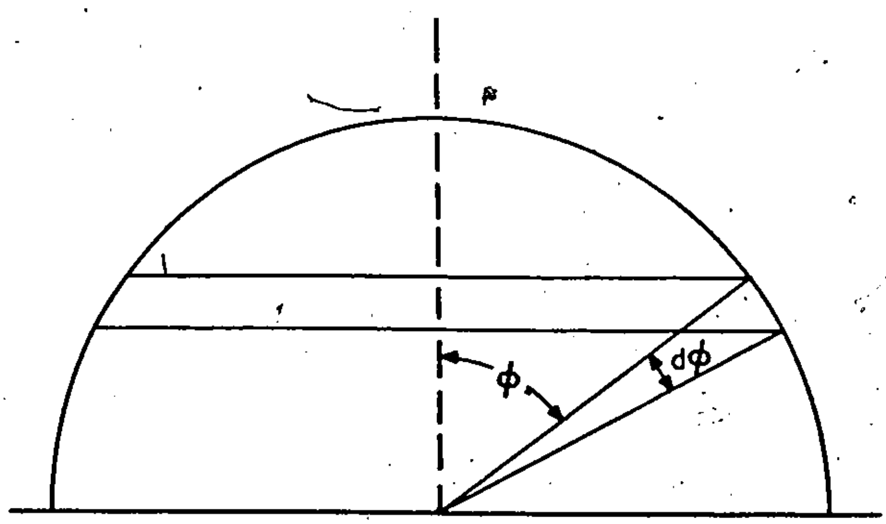
φ
dφ

Fig. 2.5

As the angle of primary beam incidence on the specimen surface varies from the normal, the number of secondary electrons emitted increases. Variations in the angle of primary beam incidence results from topographic changes on the specimen surface.

Fig. 2.6

The number of secondary electrons emitted follows a cosine distribution with the angle of emergence being the parameter.

Brinsmade and others (2.15,2.16), the energy distribution of secondary electrons approaches a Maxwellian form. This is shown schematically in Figure 2.7. Recent experimental work by Amelio (2.17) has confirmed this distribution. He has determined experimental values for E_{max}, the most probable energy of emission for copper and silicon. These values are compared with the theoretical values in Table 2.8. Although specific values of E_{max} have been determined for a range of materials, we shall accept a value of 2 eV for calculation purposes.

This concludes the discussion of the secondary electron emission process. The next section describes the structure and operation of the scanning electron microscope.

2.3 The Scanning Electron Microscope

Figure 2.9 shows the essential components of a scanning electron microscope. There are three basic groups of components, namely, the electron-optical column (and associated power supplies and controls), the vacuum system (including the specimen chamber and stage) and the signal detection and display equipment. Each one of these will be discussed below starting with the electron-optical column. The discussion will be based on the Cambridge Instrument Company's "Stereoscan" scanning electron microscope, which was used for the majority of the work presented in this thesis, and is a typical example of these instruments.

2.3.1 The Electron-Optical Column

High energy electrons, produced in a conventional auto-biased triode electron gun, are accelerated through an electron-optical column consisting of a series of magnetic condenser lenses. Figure 2.9 shows a microscope using a three lens system. The electron beam is demagnified as it passes through the electron-optical column to a final diameter at the specimen surface of approximately 100 Å.

The third lens, which is used to focus the electron beam onto the specimen, contains a set of scanning coils which scan the beam over the specimen surface in a T.V. type raster. In addition, the beam may be scanned in a single line in either the x or y direction or positioned as a spot which is moveable in both the x and y directions.

FIG. 2.7

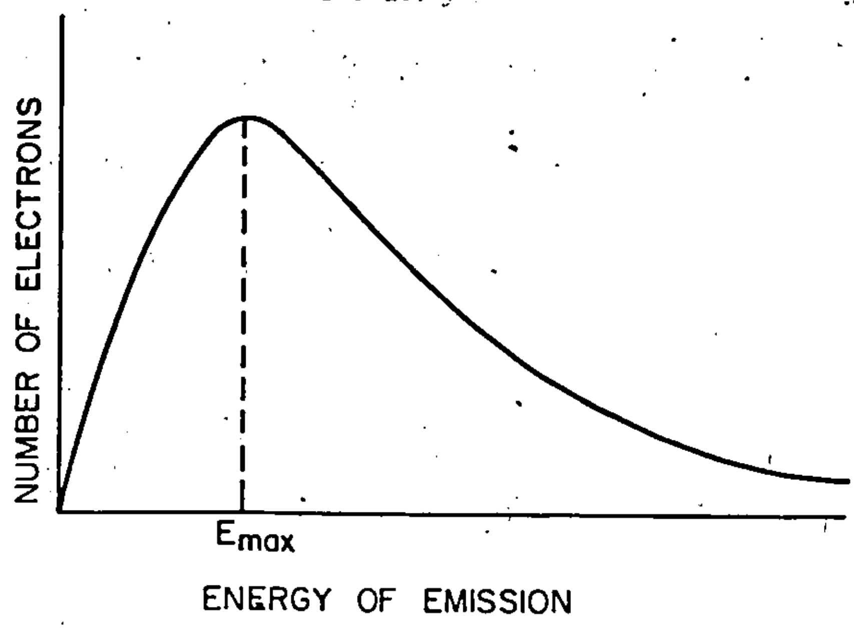

TABLE 2.8

MATERIAL	Emax (MOST PROBABLE)	Emax (EXPERMENTAL)
COPPER	2.5 ev	2.8 ev
SILICON	1.8 ev	1.7 ev

Fig. 2.7

This graph shows the energy of emission of the secondary electrons plotted against the number of secondary electrons emitted. The parameter E_{max} is the energy of emission for the maximum number of secondary electrons emitted.

Table 2.8

The parameter E_{max} varies from specimen to specimen as shown in this table.

FIG. 2.9

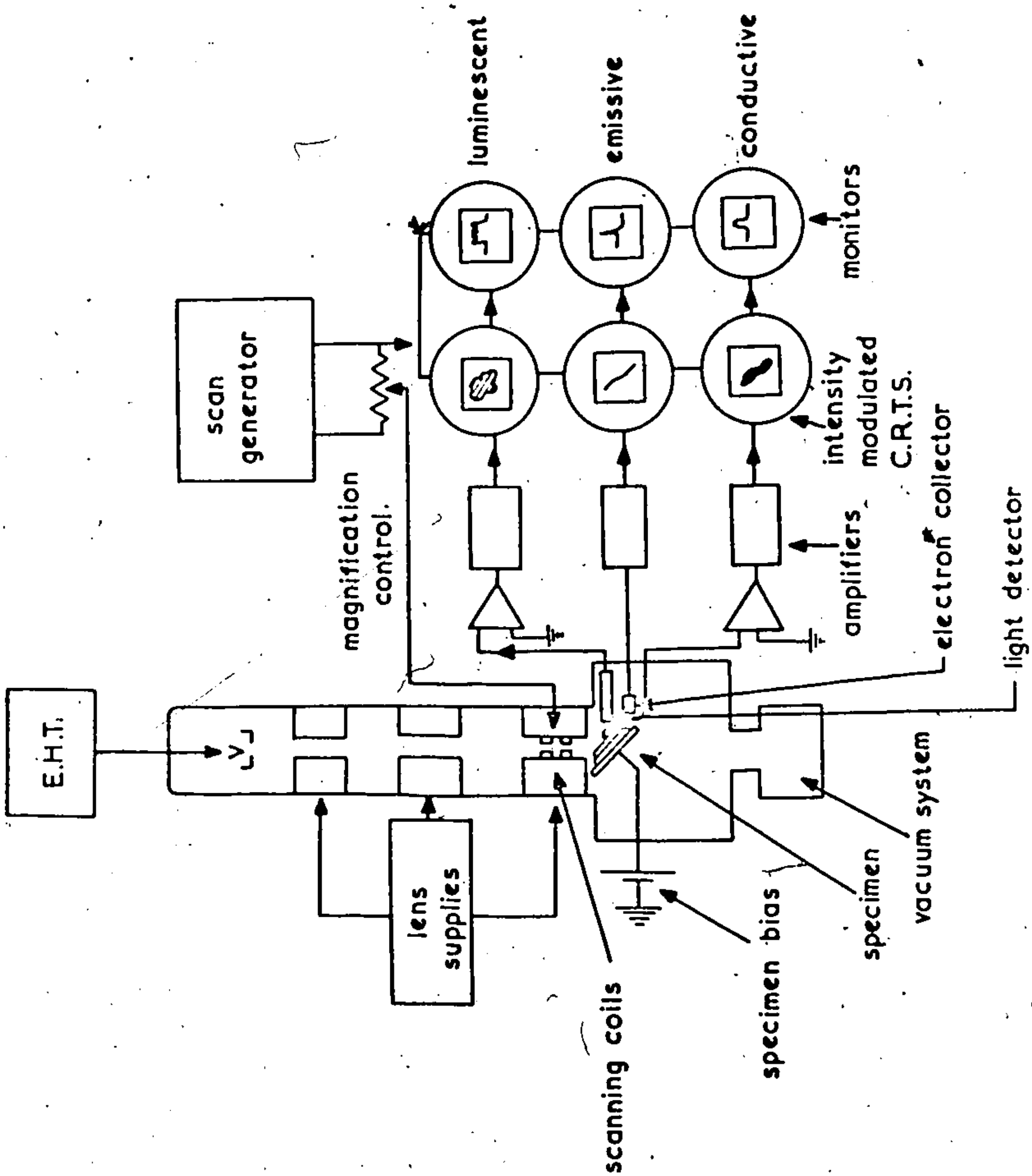

E.H.T.
lens supplies
scanning coils
specimen bias
specimen
vacuum system
light detector
electron collector
magnification control.
scan generator
amplifiers
intensity modulated C.R.T.S.
monitors
luminescent
emissive
conductive

Fig. 2.9

This figure shows a typical SEM layout illustrating the electron optical column on the left, the detector and amplifier systems in the centre and the display system on the right.

The detailed operation and performance parameters of electron-optical columns are beyond the scope of this thesis. This information is well documented in the literature (2.18,2.19,2.20).

2.3.2 The Vacuum System

The specimen to be examined is mounted in a specimen stage which is positioned through the front port of the specimen chamber so that the specimen lies beneath the electron beam. The stage provides movement in the x, y and z axes as well as 360° rotation and 0° to 90° tilt of the specimen with respect to the beam. Electrical lead throughs are also provided on the stage and at the rear of the specimen chamber so that specimens and/or experimental detector systems can be biased. Several extra ports are provided on the stage and at rear of the specimen chamber to allow special detector systems to be mounted.

The chamber and electron-optical column are pumped by means of oil diffusion pumps to an operating vacuum of approximately 10^{-5} torr. The electron-optical column is pumped by a separate pumping system and an isolation valve is used to isolate the column from the chamber. This allows the column to be kept at an operating vacuum while the chamber is brought to atmospheric pressure for specimen changing. The use of such an isolation valve is an aid in obtaining a fast pump down time after a specimen change.

2.3.3 The Signal Detection and Display Electronics

The electron beam is scanned across the specimen surface by means of waveforms applied to the scanning coils from the scan generator. Various interactions occur when the high energy primary beam strikes the specimen surface; some of these have already been described in section 2.1. Any spatial variation in these phenomena can be displayed providing a suitable detector is provided. The signal from such a detector is used to intensity modulate a display CRT which is scanned in synchronism with the primary electron beam. Magnification is obtained by decreasing the drive to the scan coils while keeping the CRT scan excitation constant. In this manner, the area scanned on the specimen is reduced while the display area is maintained constant. The ratio of the two raster sizes determines the magnification, which may be as high as 50 to 100,000 times.

2.4 The Emissive Mode of Operation

The detection and display of the secondary electrons generated by the primary electron beam striking the specimen surface is called the emissive mode of operation of the SEM. The standard detector system used for detection of secondary electrons is the Everhart-Thornley detector (2.21). This is shown in Figure 2.10. The low energy secondary electrons are attracted towards the positively biased Faraday Cage (+ 200 volts). On passing through the grid, the electrons are accelerated towards the scintillator by a +12 kV potential applied to an aluminum coating over the surface of the scintillator. This coating is very thin (≈ 500 Å) and the electrons pass through it with sufficient energy to cause scintillation. The light generated in this process is transmitted down a light pipe to a photomultiplie amplified and the signal used to intensity modulate the display CRT. This method of detection provides a high gain, low noise, broad band-width secondary electron collection and amplification system.

Sources of contrast in the emissive mode have been considered by Everhart, Wells and Oatley(2.22). Figure 2.11 illustrates some of the effects which can lead to contrast in the emissive mode of operation. These effects are the topography of the specimen surface, the atomic number of the specimen and its resistivity. As the angle of incidence of the primary electron beams varies due to topographical changes on the specimen surface, the effective depth of generation of secondary electrons changes as the induced plasma is tilted (see sections 2.1 and 2.2). This results in a variation of the number of secondary electrons which can escape from the surface and thus gives rise to contrast in the emissive mode. A similar variation in the number of emitted secondaries occurs due to changes in specimen atomic number (see section 2.1). In addition, contrast may result from changes in the surface potenti of the specimen with respect to the Faraday cage collector. This effect is discussed in Section 2.6. Figure 2.12 shows some examples of emissive micrographs from the SEM.

FIG. 2.10

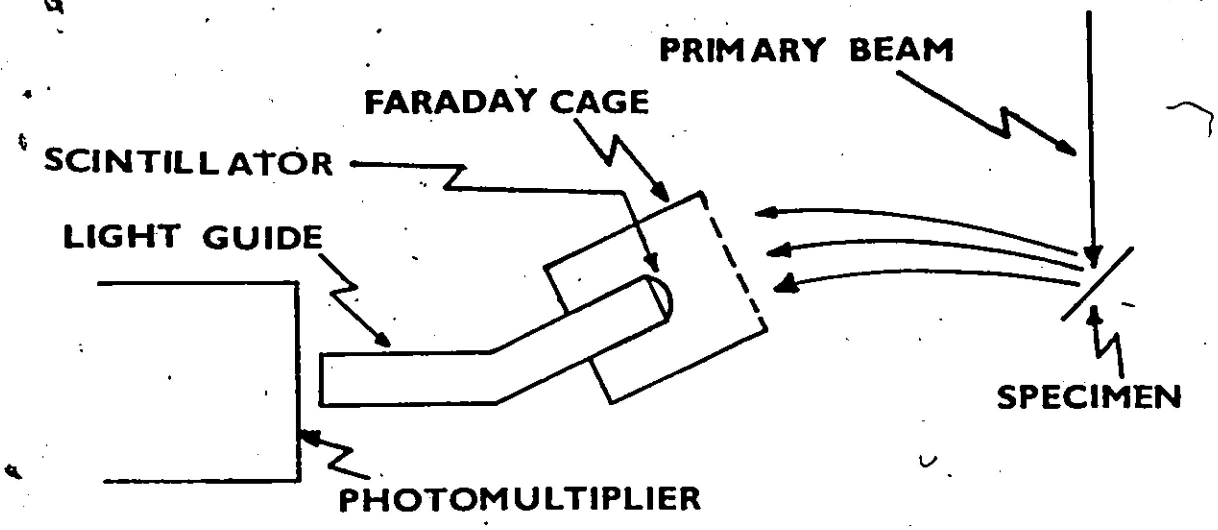

FIG. 2.11

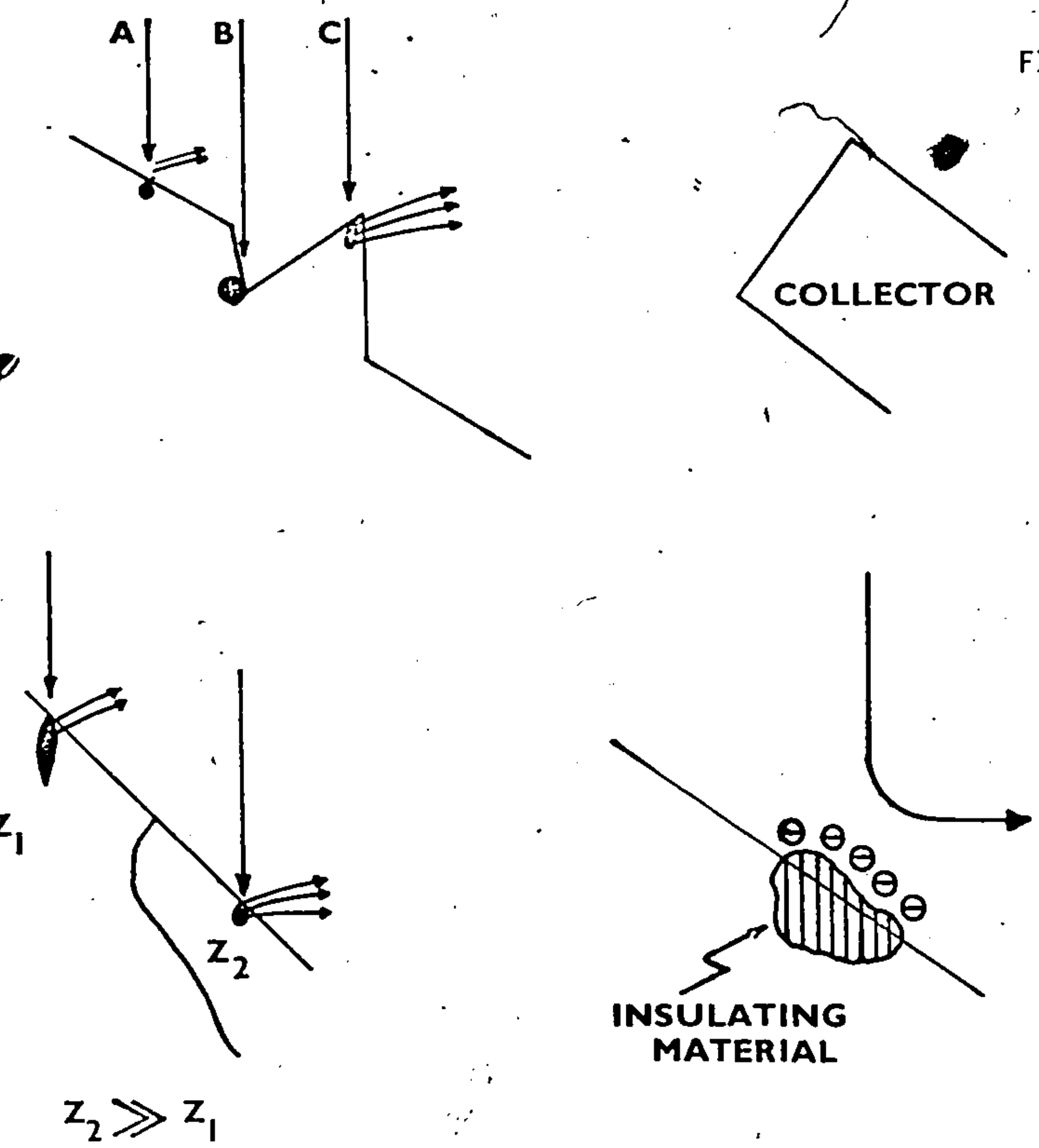

Fig. 2.10

Shows the Everhart-Thornley collector system used in the SEM for the collection and detection of secondary electrons. The three sections of this collector system are the Faraday cage (+ 200 volts), Scintillator (+ 12,000 volts) and light pipe assembly and the photomultiplier.

Fig. 2.11

Examples illustrating the possible sources of contrast in the emissive mode of operation are shown. The three sources are topographical changes, changes in specimen atomic number and regions of insulating material on the specimen surface.

FIG. 2.12

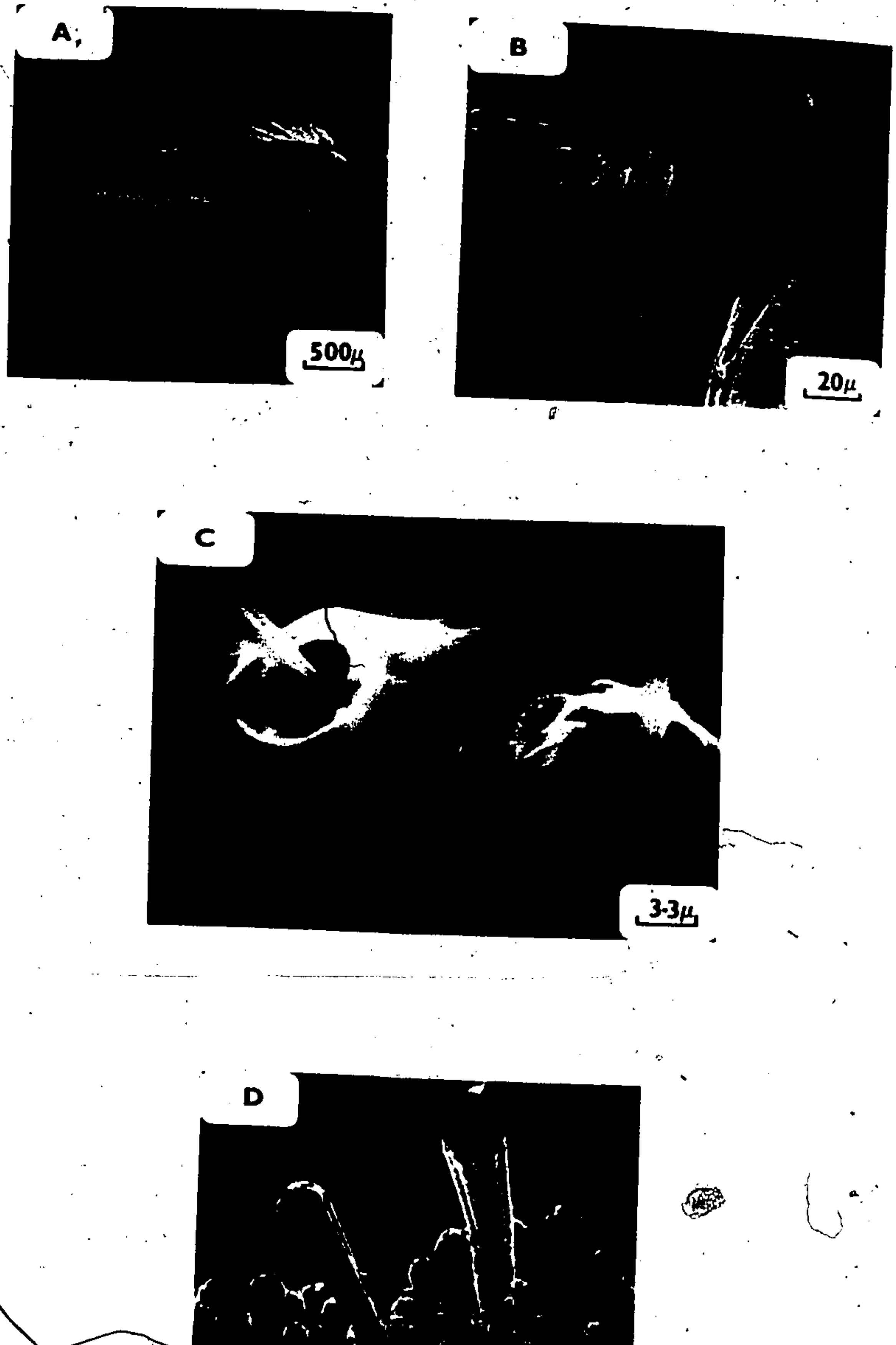

Fig. 2.12

This figure shows emissive micrographs taken in the emissive mode of operation illustrating the depth of focus available with the SEM.

Fig. 2.12(a),(b), and (c) are of insects whereas Fig. 2.12(d) shows a group of boron whiskers grown on sapphire.

Because of the geometry of the final condenser lens pole plate, the specimen,and the electron detector, the detector does not collect only secondary electrons. Some of the other possible sources of signal are illustrated schematically in Figure 2.13. Back-scattered electrons can be detected directly or can cause the emission of secondary electrons from the Faraday cage or pole plate which in turn can be detected. The degree to which back-scattered electrons contribute to the total signal detected is important because a significant back-scattered electron contribution can limit the spatial resolution in the emissive mode of operation.

Resolution in any mode of operation of the SEM (see below) is determined by the area on the specimen from which the signal of interest is emitted. This is always larger than the area of the incident electron beam. In the case of secondary electrons, the diameter of this area is shown as, A, in the schematic diagram, Figure 2.3. For back-scattered electrons, however, the effective area is much larger as these electrons can escape from deeper in the specimen (B in Figure 2.3).

2.5 Other Modes of Operation of the SEM

The backscattered primary electrons (see section 2.1) can be collected and displayed using silicon diode detectors. This mode is called the back-scattered electron or reflected primary mode of operation. Although it is of limited spatial resolution it can provide useful information on atomic number variations in the specimen and it has been applied to the detection and measurement of thin surface films (2.23).

Usually the specimen in the SEM is grounded to prevent it charging up under, the influence of the primary beam.. If the current flow to ground is amplified and displayed it gives a mode of operation called the specimen current mode. This mode gives a low spatial resolution, 1μ, and contains similar information to the backscattere and emissive modes.

The conductive mode of operation relies on the presence of a high field region in the specimen, such as that at a p-n junction in a semiconductor specimen. If the primary electron beam generates hole-electron pairs near such a region, the electrons will drift in one direction and the holes in the opposite direction under

FIG. 2.13

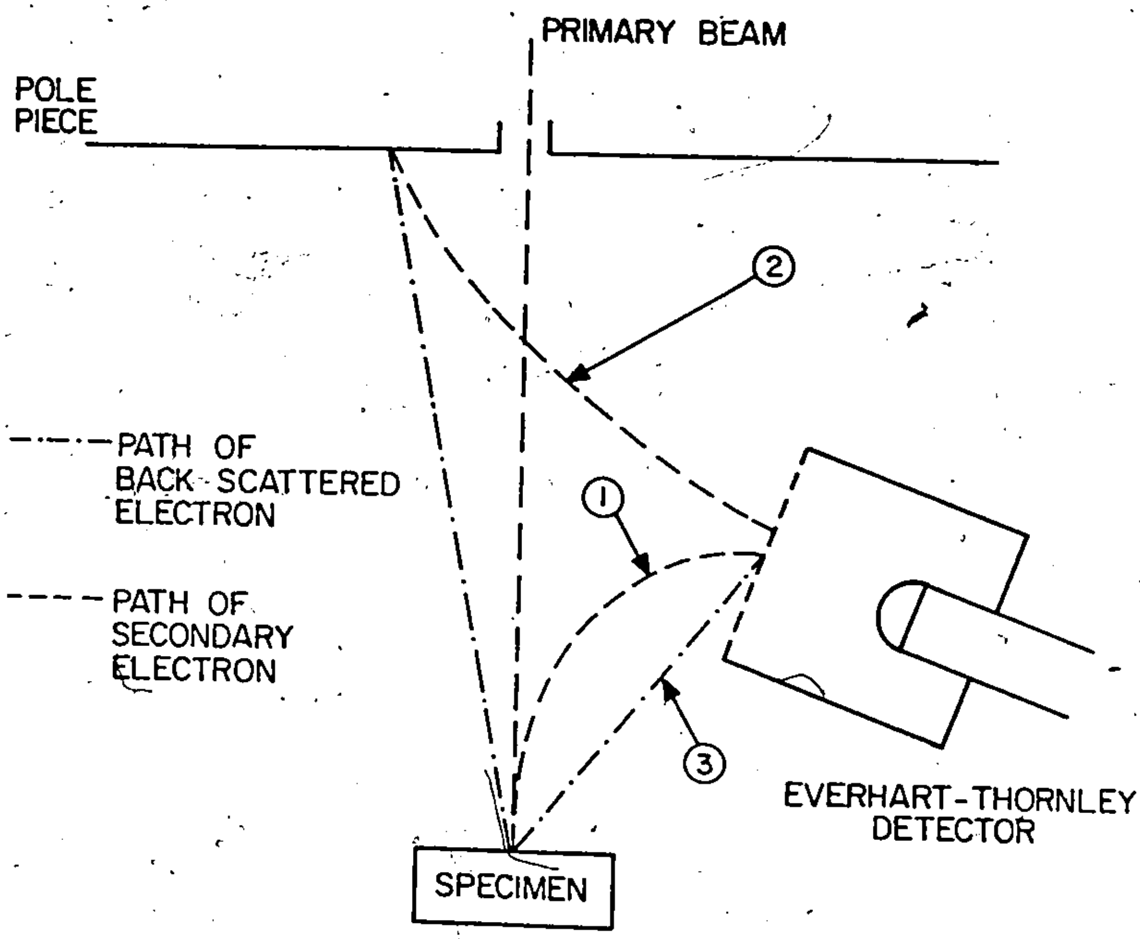
PRIMARY BEAM
POLE PIECE
PATH OF BACK-SCATTERED ELECTRON
PATH OF SECONDARY ELECTRON
1
2
3
EVERHART-THORNLEY DETECTOR
SPECIMEN

Fig. 2.13

This figure shows the possible sources of detected signal in the emissive mode when using the standard Everhart-Thornley detector systems. The possible sources are:

(1) Secondary electrons originating at the specimen surface.

(2) Secondary electrons originating at the pole piece with backscattered electrons acting as a primary beam.

(3) Backscattered electrons emitted from the specimen.

the influence of the high field. This process gives rise to a current in any external circuit connected to the specimen which can be detected and displayed. This mode of operation may be used to study multicontrast specimens such as transistors and complex microcircuits which can be examined under biased conditions. Other effects such as current multiplication, surface inversion layers and localized hot spot formation may also be observed (2.24,2.25).

The hole-electron pairs in the specimen may recombine by the emission of photons of energy. Depending on the specimen material and the recombination processes involved, this emission may lie in the visible, ultraviolet or infra-red region of the spectrum. If this light output signal is detected and displayed, the spatial variations of the recombination processes operating can be studied. This is called the cathodoluminescent mode of operation (2.23,2.26).

X-rays emitted from the specimen can also be detected using either a non-dispersive hi-drift detector or a wavelength dispersive crystal system. The X-ray images provide information on the chemical composition of the specimen and the type, amount and spatial distribution of any impurities (2.27).

Another mode of operation of the SEM is known as the voltage contrast mode. This is a special case of the emissive mode and will be discussed in the next section.

2.6 Voltage Contrast Using the Everhart-Thornley Detector

There are two parameters of importance in discussing the detection of voltage contrast using the Everhart-Thornley detector (see section 2.4). The first is the use of an electrostatic field to attract the low energy secondary electrons towards the detector. The second is that the detector has a finite entrance aperture.

The positive potential applied to the Faraday cage generates an electrostatic field between the cage and the surrounding parts of the chamber and stage, including the specimen. This field accelerates the secondary electrons towards the entrance aperture of the Faraday cage and, depending on the trajectories of the electrons and the size of the entrance aperture of the cage, they may or may not be detected.

If the potential on the specimen is changed then the electrostatic field between the specimen and the detector is changed also. This produces a change in the trajectories of the secondary electrons which can result in a variation in the number collected. Signal arising because of this effect is called voltage contrast signal. An example of this effect is shown schematically in Figure 2.14. Here, the change in the electron trajectories produced by reverse-biasing a p-n junction results in a lower signal being detected from the n-type side of the junction. Figure 2.15 shows a pair of micrographs obtained using a SEM in the voltage contrast mode. The details are discussed in the caption. The situation is, in fact, more complex than indicated above. In the case of a reverse-biased p-n junction, because the p and the n-type materials are at different potentials and are also physically very close, a very strong local electric field exists at and above the specimen surface at the junction itself. These so-called "transverse microfields" affect the detection of secondary electrons and, depending on the relative magnitude of the specimen to collector field and the transverse microfield, different images may be obtained. These effects are discussed in detail in the next chapter.

2.7 Summary

In this chapter some of the processes which occur when an energetic electron beam strikes a solid target have been described. The mechanism of secondary electron emission and the angular and energy distribution of the emitted electrons have been discussed with reference to the published literature. It was shown how secondary electrons are used in the scanning electron microscope to form an image of the specimen surface and how contrast arises due to topographic detail. In addition, the other modes of operation of the scanning electron microscope were described briefly.

The final section of the chapter introduced the concept of voltage contrast using the Everhart-Thornley detector system. In the chapter that follows, the mechanism of voltage contrast is examined in more detail and a review of the published work on detectors designed to optimise this contrast is presented.

FIG. 2.14

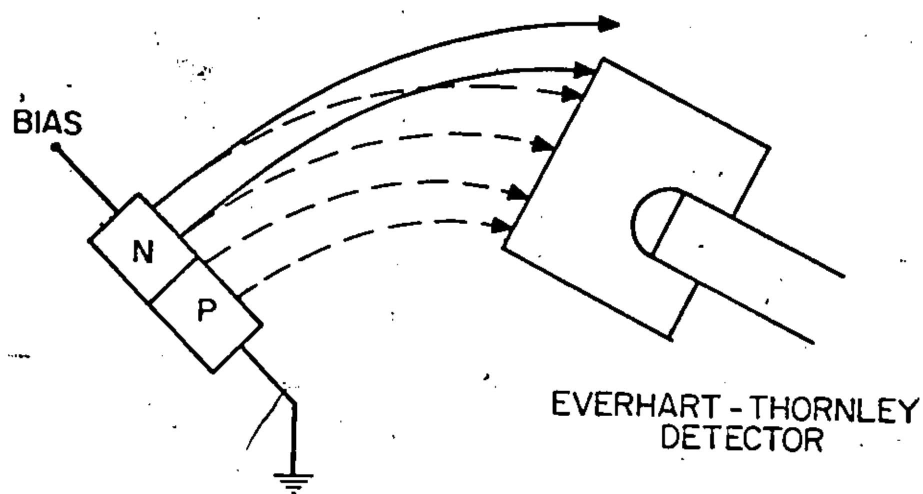

- - - - TRAJECTORY OF ELECTRONS FOR UN-BIASED SPECIMEN
——— " " " " BIASED SPECIMEN

Fig. 2.14

Shows how contrast results from biasing a P-N junction when the Everhart-Thornley detector is used. Such contrast is termed "Voltage Contrast".

FIG. 2.15

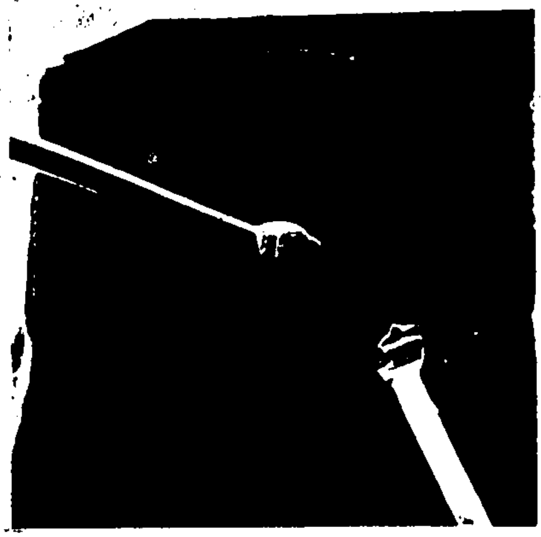

(a)

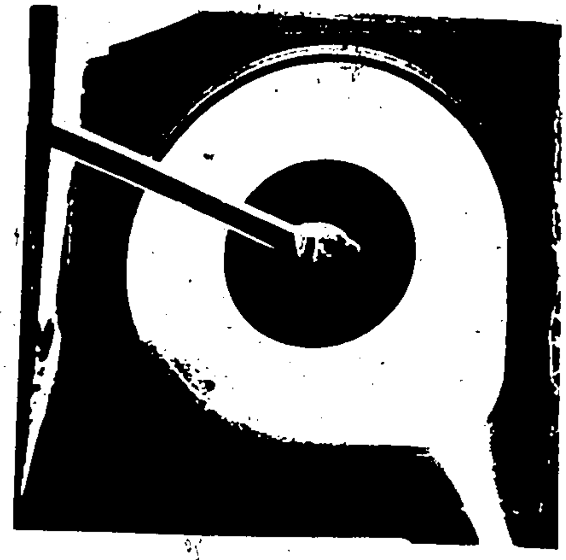

(b)

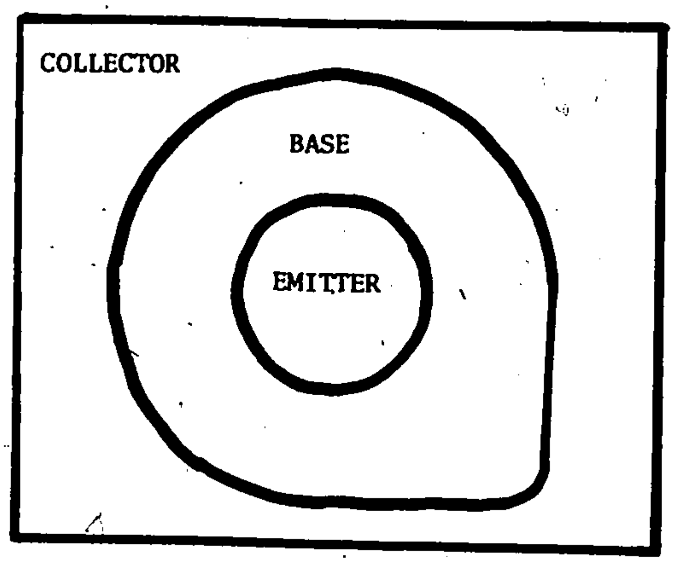

(c)

Fig. 2.15

Micrographs (a) and (b) show a 2N1893 transistor in an unbiased and biased state (0 volts and -5 volts on the base) showing detected voltage contrast.

CHAPTER THREE

The Detection of Voltage Contrast

Introduction

It is important that the surface potential of a specimen be directly related to the output signal of the SEM so that variations in this signal can be unambiguously related to changes in the surface potential. It is therefore desirable that the relationship between the specimen potential and the output signal be linear, it is imperative that it be monotonic. This is not the case for the commonly used Everhart Thornley electron detector as will be seen in section 3.3.

Several research workers have produced secondary electron detectors designed to give a near linear voltage contrast characteristic. Although all the detector designs make use of the change in energy of the secondary electrons produced as a result of a change in the specimen potential, the detailed approach used allows a classification of the detectors into two groups: namely, energy analyzer detectors and trajectory sensitive detectors.

The first type of detector system analyzes the energies of the emitted secondary electrons and relates changes in this energy to surface potential. The second type utilizes the variation in the secondary electron trajectories, caused by a change in their energy to produce a change in the number of secondary electrons collected. These variations in the number of secondary electrons collected are then related to specimen potential.

This chapter presents a review of the published work on voltage contrast detectors. Finally, using this review as a basis, the design criteria for a new voltage contrast detector are developed.

First of all, however, the co-existence of voltage contrast and field contrast due to transverse micro-fields is discussed.

3.1 Transverse Fields and Field Contrast

On specimens such as integrated circuits, there will, in general, be areas at many different potentials. Because of this, local transverse micro-fields will exist at the specimen surface. The observation of voltage contrast, i.e. changes in detected signal resulting from changes in the net specimen to collector field, may be complicated or obscured by field contrast resulting from these local field regions near the specimen surface. Information about these transverse fields is carried by the slow secondary electrons since they are strongly influenced by these fields.

Saparin et.al. (3.1) have analysed this situation in the case of a p-n junction. They assumed that the electron density distribution in the plane of the Everhart-Thornley detector was Gaussian, and that the microfield merely displaced this distribution and did not distort it. The situation is shown schematically in Figure 3.1. The shift in this distribution was calculated for electrons emerging at right-angles to the specimen surface into a transverse microfield which was assumed to decrease exponentially with distance from the specimen surface. The normal and parallel components of the transverse fields, E_y and E_x respectively are thus given by:

$$E_x = E_{ox} \exp(-y/2d)$$

and

$$E_y = E_{oy} \exp(-y/2d)$$

where E_{ox} and E_{oy} are the field components at the point of emission which is also the origin of the coordinate system and 2d is of the order of the width of the p-n junction. Using this analysis, Saparin determined that the type of image obtained would depend on the relative strength of the components of the microfield and on the normal component of the collection field at the specimen surface, E_a. If E_y was opposed to E_a and if E_y was sufficiently large, then secondary electrons could be reflected back into the specimen surface by the microfield and not be collected. Defining a critical field E_y', at which secondary electrons are just collected, it was shown that for parts of the specimen where $E_y > E_y'$ a dark area would be observed. Similarly when E_a and E_y are additive a bright area was predicted. In the case of a p-n junction either a dark band, a light-band or a multiple band was predicted depending on the details of the local electric field

FIG. 3.1

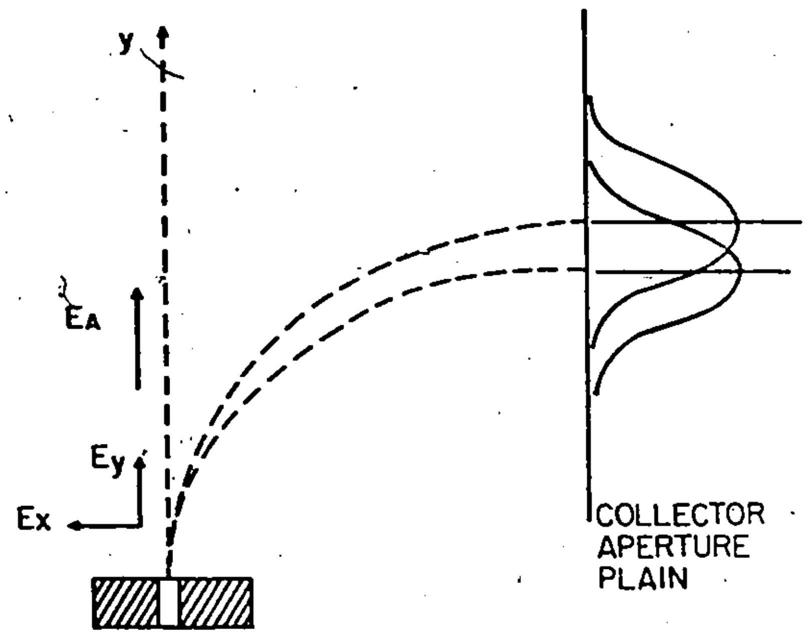

Fig. 3.1

Saparin et.al. analysis assumed a shift in the Gaussian electron density distribution in the aperture plane of the Everhart-Thornley detector, this shift resulting from microfield components E_x and E_y.

component. Many of the cases predicted have been observed in practice.

Plows and Nixon (3.2) have analysed the p-n junction using field plotting techniques. They also predict the co-existence of surface field contrast and voltage contrast and show, theoretically and experimentally, that the surface field contrast gives rise to a "shadow" or dark band adjacent to the junction. Their reasons for this are in agreement with those proposed by Saparin (see above). Plows and Nixon also show that if the normal component of the collection field is increased, the width of the dark shadow is reduced and the effects of surface field contrast are minimised. This technique is used in many of the detector designs described below.

3.2 Energy Analyser Voltage Contrast Detector

It is possible to measure the energy of secondary electrons emitted from a specimen surface and to relate changes in that measured energy to surface potential variations. Many workers have used this technique to perform surface voltage measurements; the techniques and detector designs will be described in this section.

3.2.1 The Plows-Nixon Detector

The detector designed by Plows and Nixon (3.2) uses an arrangement of three planar parallel grids followed by a scintillator and photomultiplier, Figure 3.2. This arrangement forms a retarding field energy analyzer with grids 1 and 3 held at several hundred volts positive with respect to the specimen and grid 2 near to the specimen potential. The first grid applies a high normal electric field at the specimen surface, the second acts as a velocity filter, and the third shields the velocity filter grid from the high scintillator potential.

The operation of this retarding field analyzer may be explained as follows. If we consider a single secondary electron of emission energy E_e, it will be accelerated from the specimen surface by the electric field generated between the first grid and the specimen surface. If a potential of V_{G1} is applied to grid one, then the electron energy at grid one, E_1, will be given by

$$E_1 = E_e + eV_{G1} \qquad \text{eq. 3.1}$$

FIG. 3.2

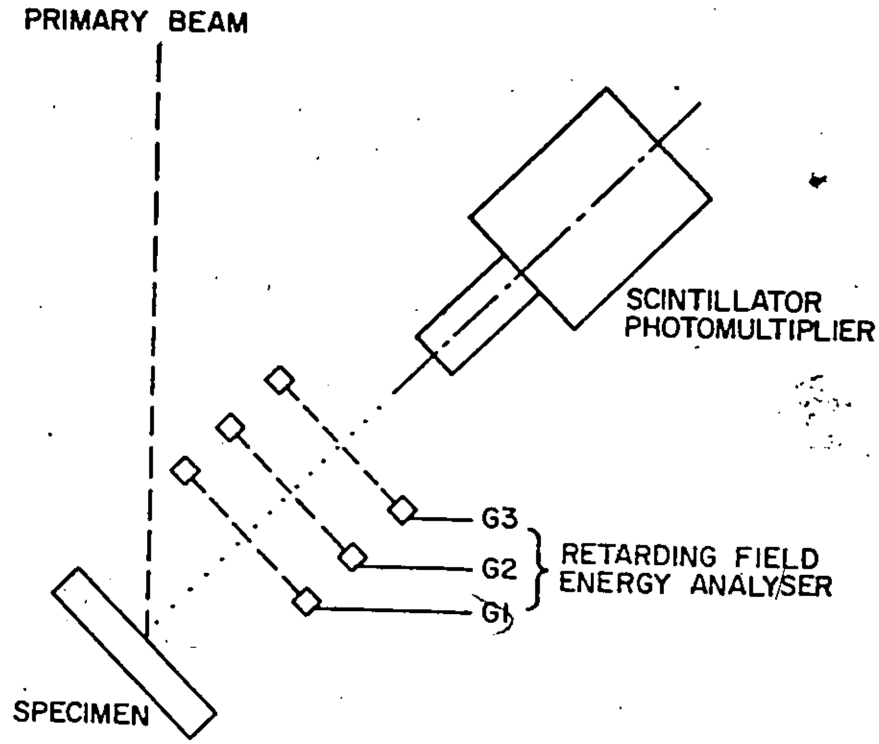
PRIMARY BEAM
SCINTILLATOR
PHOTOMULTIPLIER
G3
G2
G1
RETARDING FIELD
ENERGY ANALYSER
SPECIMEN

Fig. 3.2

This figure shows the three grid energy analyzer designed by Plows and Nixon.

G1: applies a high normal electric field at the specimen surface.
G2: velocity filter grid.
G3: Screen grid.

The electron will have this energy as it enters the retarding field between grids one and two. This retarding field is generated by applying a potential of V_{G2} to grid two, where $V_{G2} << V_{G1}$. This retarding field decelerates the electron, reducing its kinetic energy by the amount $e(V_{G1} - V_{G2})$ so that when it passes through grid two its kinetic energy E_2 is given by

$$E_2 = E_1 - e(V_{G1} - V_{G2}). \qquad \text{eq. 3.2}$$

If the values of V_{G2} and V_{G1} are chosen so that E_2 becomes zero, i.e. $E_1 = e(V_{G1} - V_{G2})$ then E_e becomes a critical value of emission energy. In reality there is a spread or distribution of emission energies, in this case those electrons with emission energies greater than E_e will be transmitted through grid two (E_2 positive) and those with energies less than E_e will be reflected back towards grid one (E_2 negative).

The electrons which pass through grid two are accelerated towards the third grid and the scintillator by a potential of V_{G3} applied to grid three, where $V_{G3} >> V_{G2}$.

This process of energy analysis may be likened to a moveable energy partition applied to the secondary electron emission energy distribution curve. Figure 3.3 shows this schematically.

If in equation 3.2, we substitute for E_1 from equation 3.1 then we obtain

$$E_2 = E_e + eV_{G2} . \qquad \text{eq. 3.3}$$

Thus the energy of an electron at grid two depends only on its emission energy and the potential on grid two. If the specimen is held at a potential V_s then the equation 3.3 becomes

$$E_2 = E_e + e(V_{G2} - V_s). \qquad \text{eq. 3.4}$$

If the specimen potential, V_s, is varied then the effective energy of emission of a secondary electron is varied also. The effect of this is to shift the energy distribution of secondary electrons with respect to the energy partition thus producing a change in the number of electrons transmitted through the analyzer and detected. The number transmitted and detected is the integral of the distribution

FIG. 3.3

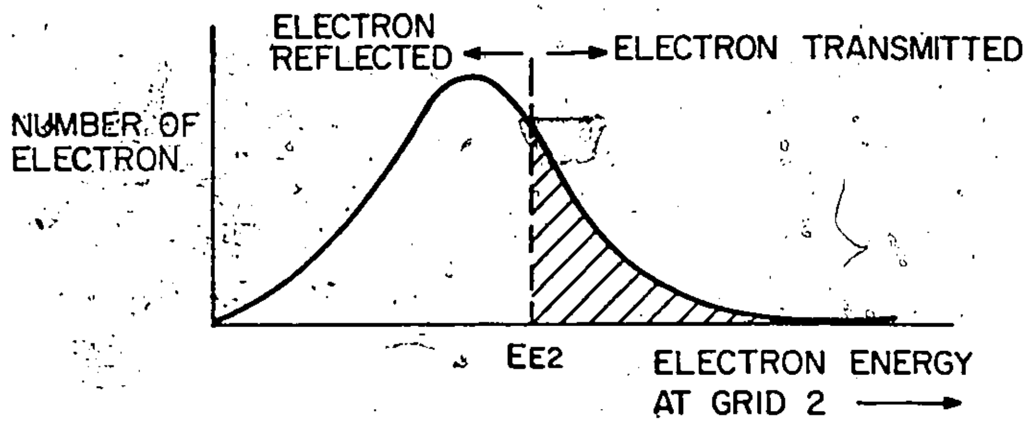

ELECTRON REFLECTED
ELECTRON TRANSMITTED
NUMBER OF ELECTRON
EE2
ELECTRON ENERGY AT GRID 2

FIG. 3.4

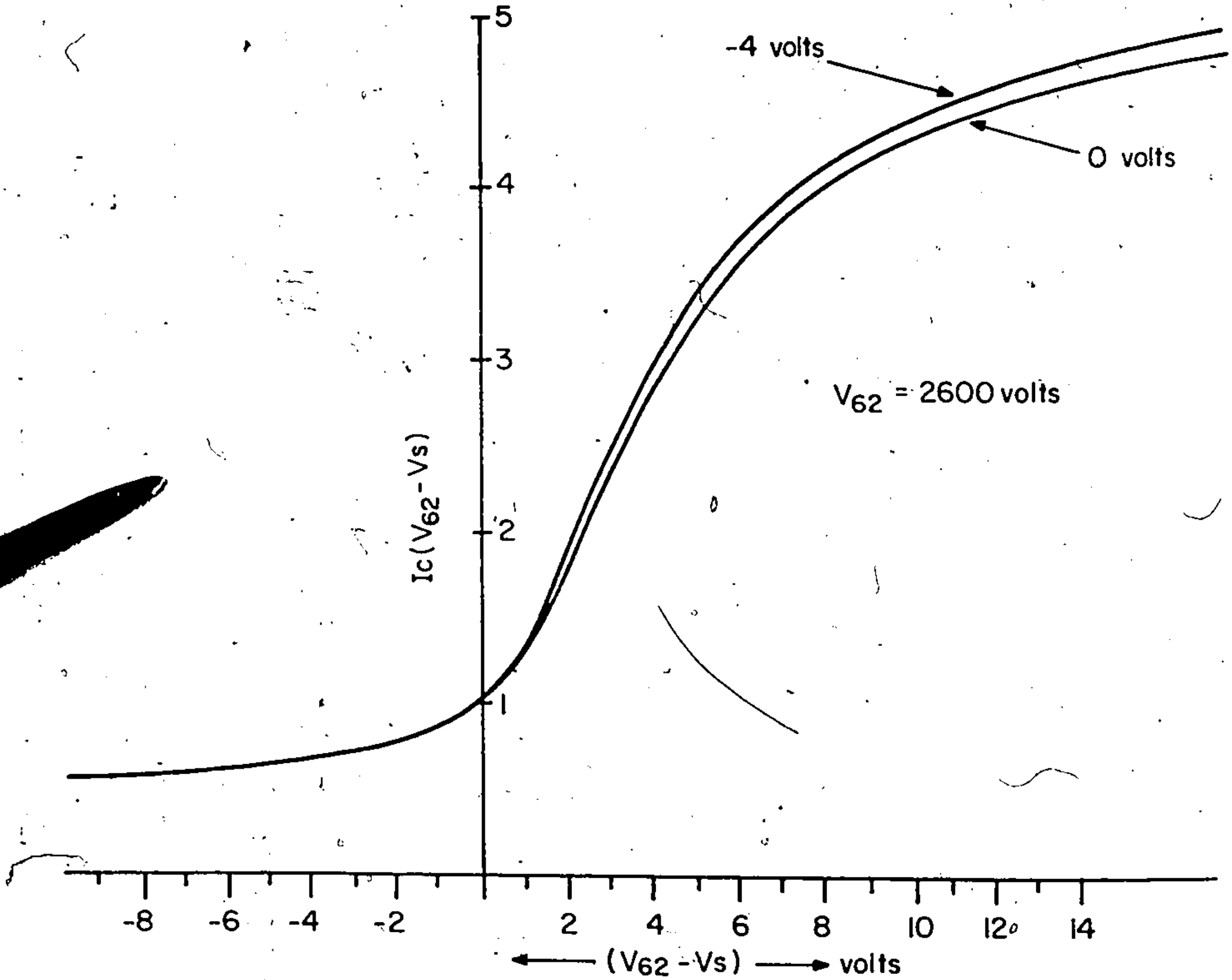

-4 volts
0 volts
V62 = 2600 volts
Ic(V62 - Vs)
1
2
3
4
5
-8
-6
-4
-2
2
4
6
8
10
12
14
(V62 - Vs) volts

Fig. 3.3

The concept of a movable energy partition used to describe the operation of the Plows-Nixon detector and other such retarding field energy analysis detectors is shown.

Fig. 3.4

This graph shows collected electron current I_c versus specimen potential a, grid two potential difference $(V_{G2} - V_S)$ for the Plows and Nixon detector.

function from the energy partition up to $+\infty$. If the energy partition always lies on the right of the peak emission energy then this integral is a continuous monotonic function. In this case, the output of the detector is a continuous, monotonic function of the specimen potential, V_S.

Plows and Nixon determined that an operating potential of 2.6 kV on the first grid was sufficient to reduce the effects of transverse fields at the specimen surface so that useful voltage contrast information could be observed. This work was carried out using an interdigitated transistor structure as a specimen. By plotting the detector output versus $(V_{G2} - V_S)$ they obtained characteristics of the form shown in Figure 3.4.

Assuming that the characteristic is linear in the region of maximum slope, Plows and Nixon estimate that for a one volt change the measurement error would be of the order of 1%, for a two volt change 11%, and for a four volt change 17%. They go on to show that by sacrificing sensitivity the linearity can be improved.

If a sinusoidal voltage is applied to the control grid along with a D.C. voltage, V_{G2}, then the operation of the detector can be understood from Figure 3.5. Using the same nomenclature as Plows and Nixon, when the mean grid two voltage $\overline{V}_{G2}$ equals V_{GQ}, the point of maximum slope of the unmodified characteristic then, assuming linearity within this region, the detected current $i_Q(t)$ will depart negligibly from a sinusoid provided that the peak to peak sinusoid, V_{OP} is sufficiently small. Hence the mean collected current $(\overline{i}_c)_Q$ will equal the unmodified value of collected current. If $\overline{V}_{G2} = 0$ however, $(\overline{i}_c)_P$ lies above the unmodified value while if $\overline{V}_{G2} = V_{GR}$ then $(\overline{i}_c)_R$ lies below the unmodified value. If the frequency of the voltage applied to grid two is higher than the bandwidth of the detector amplifier then $i_P(t)$, $i_Q(t)$ and $i_R(t)$ are integrated and the output of the amplifier is proportional to the mean values. If this mean collected current is plotted against $(V_{G2} - V_S)$, with peak-to-peak value of the grid two sinusoid as parameter, the family of curves shown in Figure 3.6 is obtained. The slope of the linearised characteristic is less than that of the unmodified characteristic resulting in a decrease in the voltage sensitivity.

FIG. 3.5

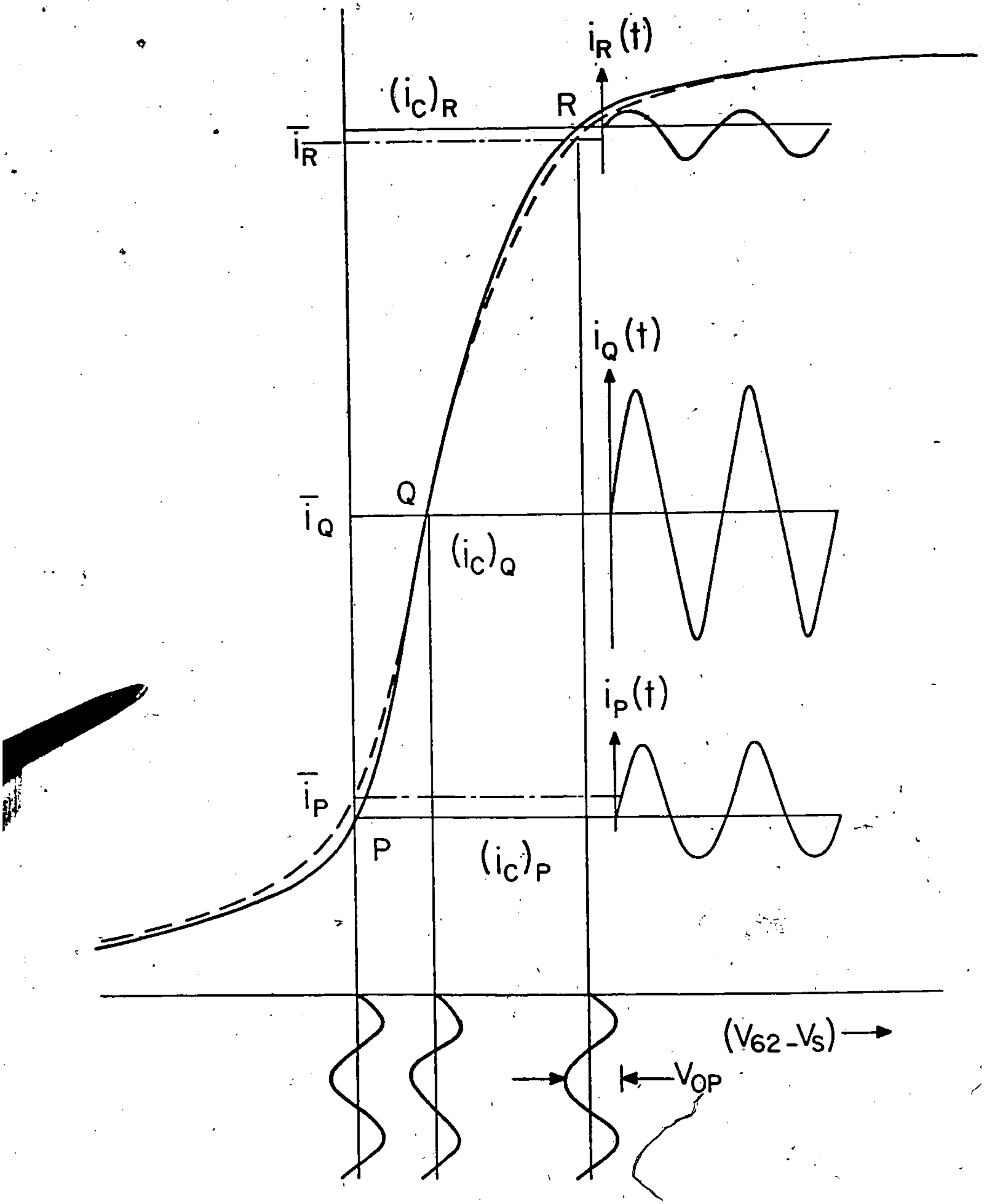

$i_R(t)$
$(i_C)_R$
R
$\overline{i_R}$
$i_Q(t)$
Q
$\overline{i_Q}$
$(i_C)_Q$
$i_P(t)$
$\overline{i_P}$
P
$(i_C)_P$
$(V_{62}-V_S)$
V_{OP}

Fig. 3.5

Shows the linearization technique used by Plows and Nixon. See text of description.

FIG. 3.6

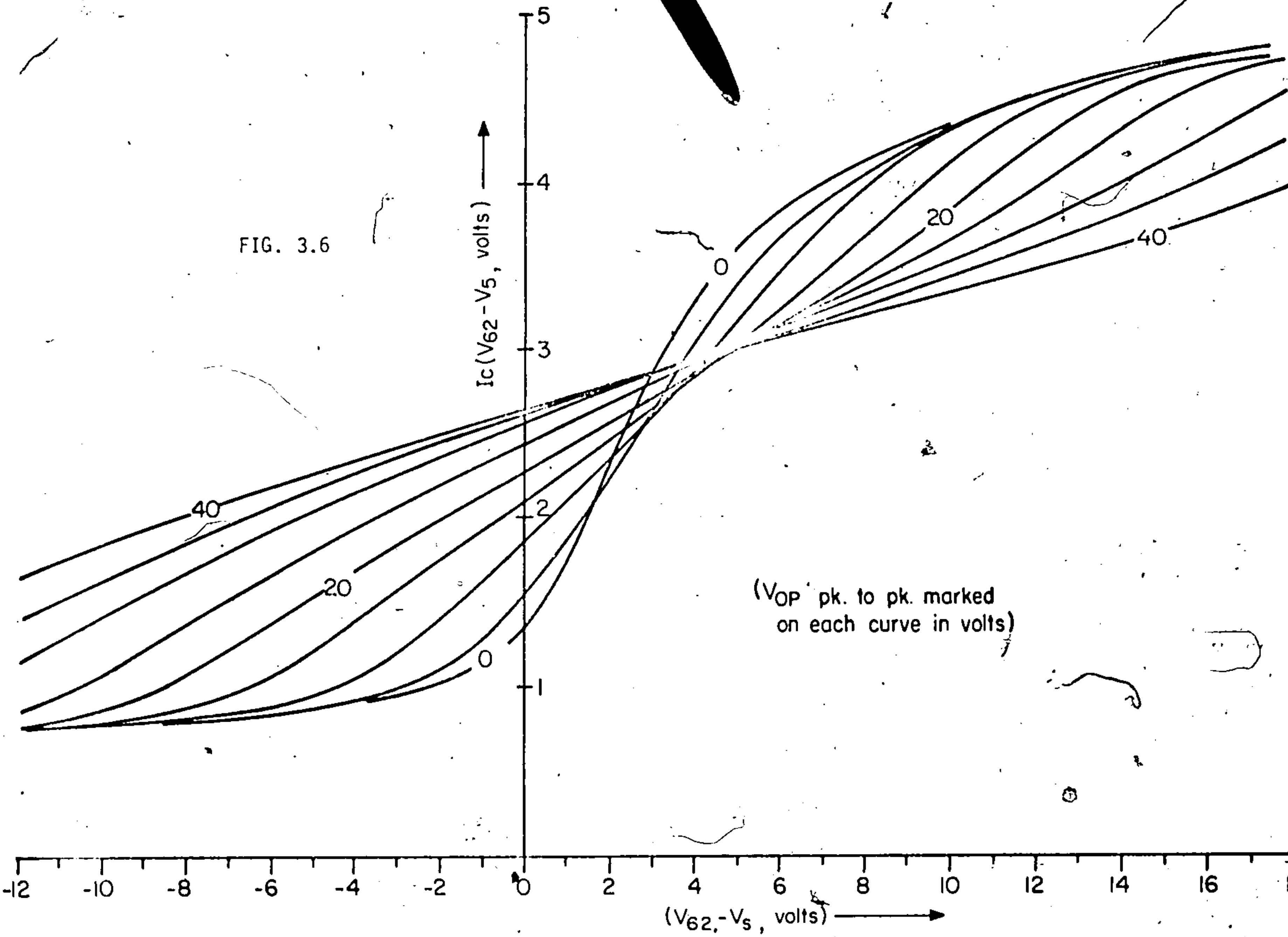

Ic(V62-V5, volts)
5
4
3
2
1
40
20
0
(VOP pk. to pk. marked
on each curve in volts)
-12
-10
-8
-6
-4
-2
0
2
4
6
8
10
12
14
16
18
(V62,-Vs , volts)

Fig. 3.6

The family of "Voltage Contrast Characteristic" curves obtained using Plows-Nixon linearization technique is shown here. The parameter here is the peak-to-peak value of V_{op}.

3.2.2 The Flemming-Ward Detector

Flemming and Ward (3.3) have described a voltage sensitive system using a standard Everhart-Thornley detector with two additional grids. The system is shown in Figure 3.7. The inner mesh is used to provide a high normal field at the specimen surface to reduce the effects of transverse fields. According to the authors, the second mesh reduces the energy of the electrons to facilitate their collection. In fact, this arrangement is an energy analyser similar to the one described by Plows and Nixon (see above).

In the present case, a feedback control loop is used to stabilise the operating point of the secondary electron detector in order to linearise the specimen potential versus output signal characteristic. If the specimen potential changes causing the detector output to change (at point D, Figure 3.7) then the control loop reacts to shift the specimen potential to maintain the output of the detector constant. In this way, the detector always operates at one point on its characteristic and the relationship between specimen potential and feedback control voltage, the voltage at point C, becomes almost linear. The voltage at point C is used as the detector output.

The characteristic obtained with the control loop open is shown in Figure 3.8. The general shape obtained is similar to that obtained by Plows and Nixon. Although no characteristic was shown with the control loop in use, the authors claim that a potential difference of 5 volts applied to the specimen could be measured to within a few percent from the change in the detector output signal. No definitive sensitivity or linearity data was provided. The authors conclude that their results were not critically dependent on mesh voltages, amplifier gain or the position of the operating point on the detector characteristic. In addition, they noted that a potential of 1 kV on the inner mesh was sufficient to minimise the effects of transverse fields.

FIG. 3.7

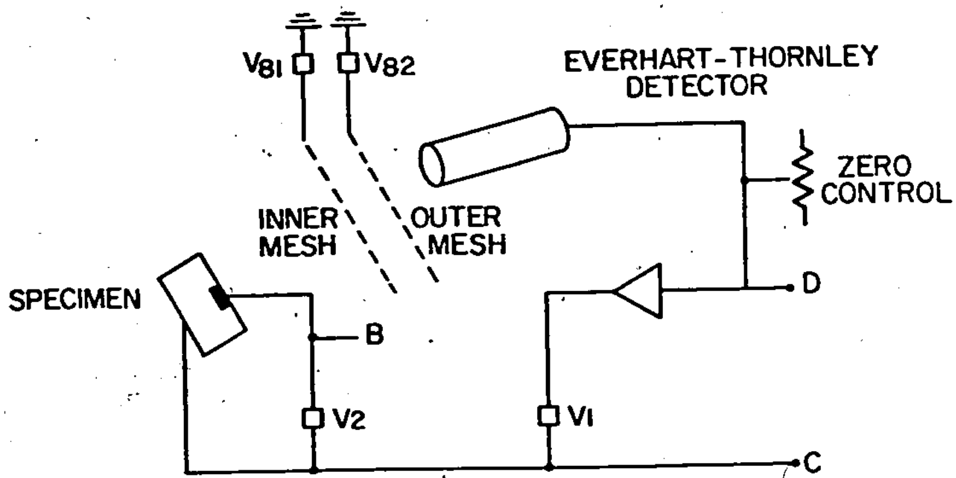
V81
V82
EVERHART-THORNLEY
DETECTOR
ZERO
CONTROL
INNER
MESH
OUTER
MESH
SPECIMEN
B
D
V2
V1
C

FIG. 3.8

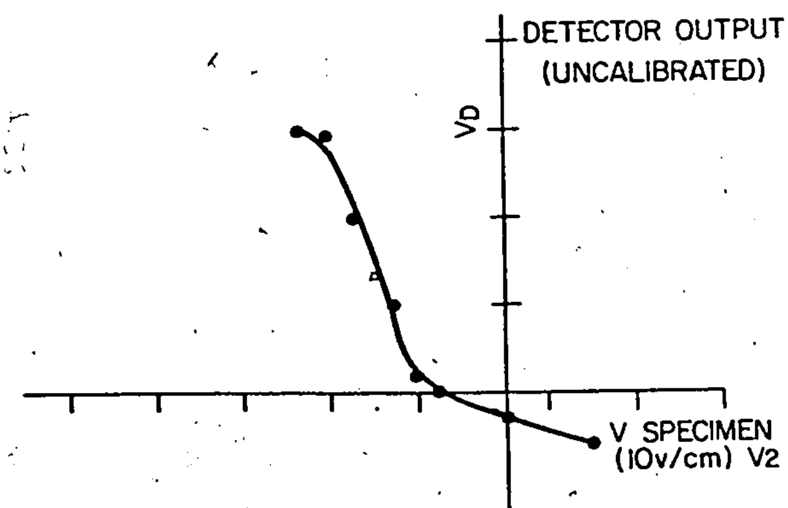
DETECTOR OUTPUT
(UNCALIBRATED)
VD
V SPECIMEN
(10v/cm) V2

Fig. 3.7

The detector design developed by Flemming and Ward using a two mesh system in conjunction with an Everhart-Thornley detector is shown.

Fig. 3.8

This shows the voltage contrast characteristic for the open-loop system of Flemming and Ward's.

3.2.3 The Gopinath-Sanger Detector

Gopinath and Sanger (3.4) describe a detector similar in operation to those of both Plows and Nixon, and Flemming and Ward except that a normal field is not used at the specimen surface to suppress the effects of transverse fields. These authors avoid the use of such a field in the belief that it may cause distortion of the local specimen potential, affecting the voltages to be measured. In addition, they were unwilling to run the risk of high voltage flashovers damaging delicate specimens.

In order to control the local electric field components at the specimen surface and to direct the electrons towards the collector, a specimen cage is used, see Figure 3.9. This type of cage was first suggested by Banbury and Nixon (3.7), see section 3.3.1. By adjusting the cage base, back and grid potentials the secondary electron trajectories are directed towards the entrance aperture of the collector.

The detector system is a retarding grid analyser of the type described above and it is used in a feedback loop similar to the one described by Flemming and Ward (3.3) except that the potential of the control grid (grid two) is varied to maintain a constant detector output instead of the specimen potential as was the case in Flemming and Ward's design. The control system is shown in Figure 3.10. The operation of the system is briefly as follows. If the energy of the secondary electrons increases, caused for example, by the primary electron beam moving into a more negative part of the specimen, then the output at A in Figure 3.10 would tend to increase also. However, because of the feedback loop, the voltage on the control grid would be decreased thus reducing the number of electrons transmitted through the analyser which would hold the output A constant. The detector characteristic is obtained by plotting the specimen potential against the control grid voltage which is the linearised detector output.

The performance of their linearised detector is illustrated by scanning the primary beam across the anode to cathode gap of a Gunn diode. This gap was assumed to have a linear resistance profile in the direction of the scan. The

FIG. 3.9

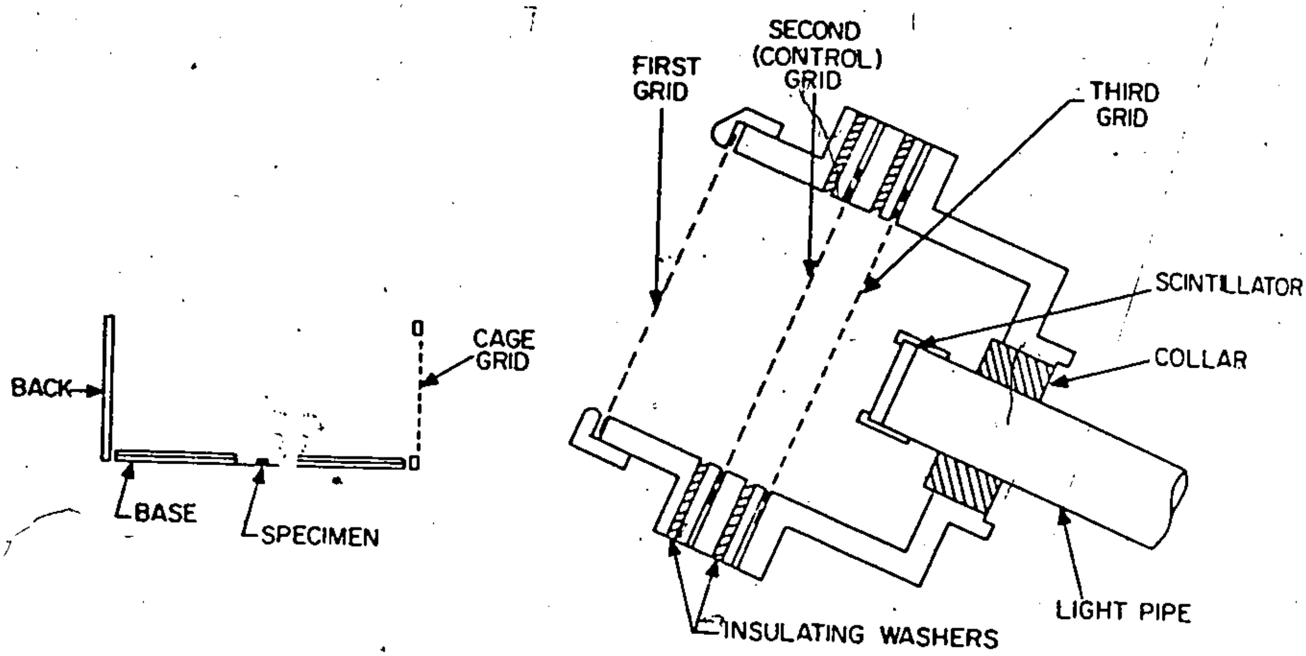
BACK
BASE
SPECIMEN
CAGE GRID
FIRST GRID
SECOND (CONTROL) GRID
THIRD GRID
SCINTILLATOR
COLLAR
LIGHT PIPE
INSULATING WASHERS

Fig. 3.9

The Gopinath-Sanger detector system combining an electrostatic cage with a Plows-Nixon energy analyzer is shown.

FIG. 3.10

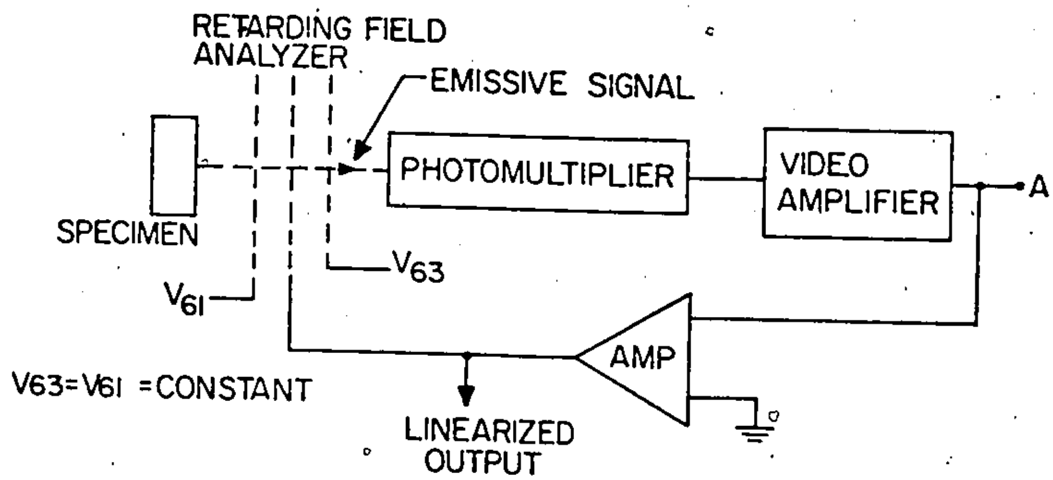

RETARDING FIELD
ANALYZER
EMISSIVE SIGNAL
PHOTOMULTIPLIER
VIDEO
AMPLIFIER
A
SPECIMEN
V63
V61
AMP
V63=V61 =CONSTANT
LINEARIZED
OUTPUT

Fig. 3.10

The feedback control loop used by Gopinath and Sanger is illustrated. The potential on grid 2 is carried to maintain the output at A constant.

characteristic obtained is shown in Figure 3.11. The bias across the device is 5.5 volts. No linearity, sensitivity or range specifications are given.

3.2.4 The Driver Detector

Driver (3.8) also used a three grid retarding field energy analyzer but of different geometry. The first and second grids are in the form of hemispheres which enclose the specimen, while the third grid forms part of a large aperture Everhart-Thornley detector system. The complete arrangement is shown in Figure 3.12. A potential of +150 Volts is applied to the first mesh and a variable potential of 0 to -30 volts is applied to the second mesh. The potential on the third mesh was set at +500 volts in an attempt to compensate for the asymmetry of the system and equalise the collection efficiency over the whole range of secondary electron energies.

Driver attempted to separate voltage contrast signal from topograph signal by superimposing a 100 KHz sine wave on the specimen potentials. The output signal of the detector is then fed to a band pass filter tuned to 100 KHz with a bandwidth of 10 KHz and afterwards demodulated. In this way, only the voltage contrast signal and that component of the topographic signal with a frequency of 100 KHz ± 5 KHz is detected. This is discussed further in section 3.4.

No conclusive results are given in the paper except that the author notes a degradation of the signal to noise ratio of a factor of ten. The linearity, sensitivity and range of the system as a voltage sensitive detector are not specified.

3.2.5 The Wells and Bremer Detector

Wells and Bremer (3.9) have reported the use of an 84° deflection electrostatic cylindrical mirror energy analyser in conjunction with a slightly modified Everhart-Thornley detector to measure surface potentials. The system is shown in Figure 3.13.

Secondary electrons are accelerated towards the entrance aperture of the analyser by an electrostatic field generated between the lower electrode of the analyser, which is held at +40 volts, and the specimen, which is biased at -17 volts for some of the experiments described. Having passed through the entrance aperture,

FIG. 3.11

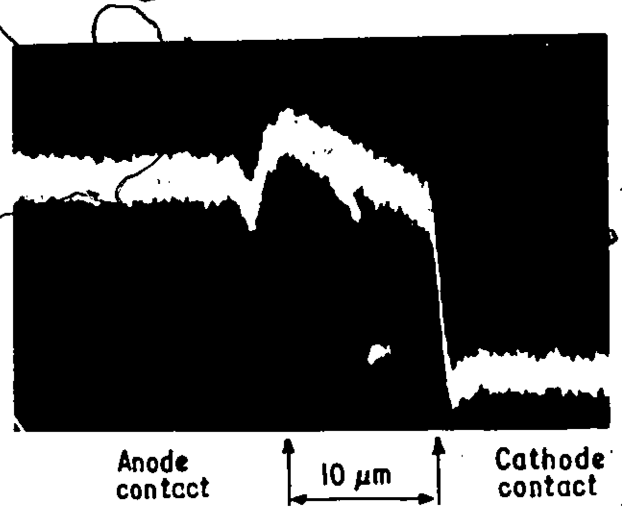

Fig. 3.11

The voltage contrast characteristic for the Gopinath-Sanger detector is shown here, obtained by scanning the primary beam across the anode to cathode gap of a Gunn diode.

FIG. 3.12

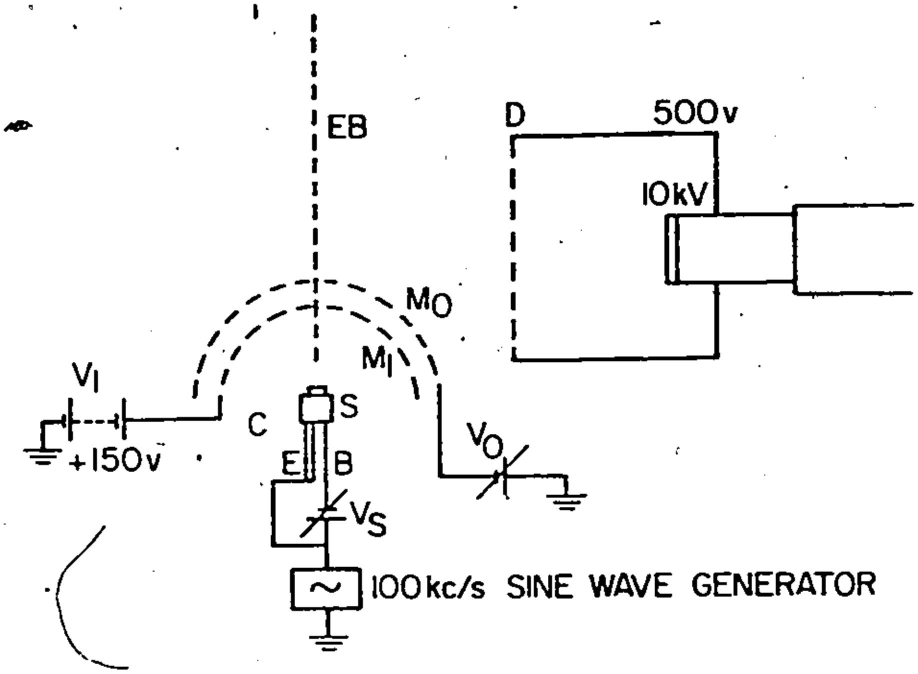

FIG. 3.13

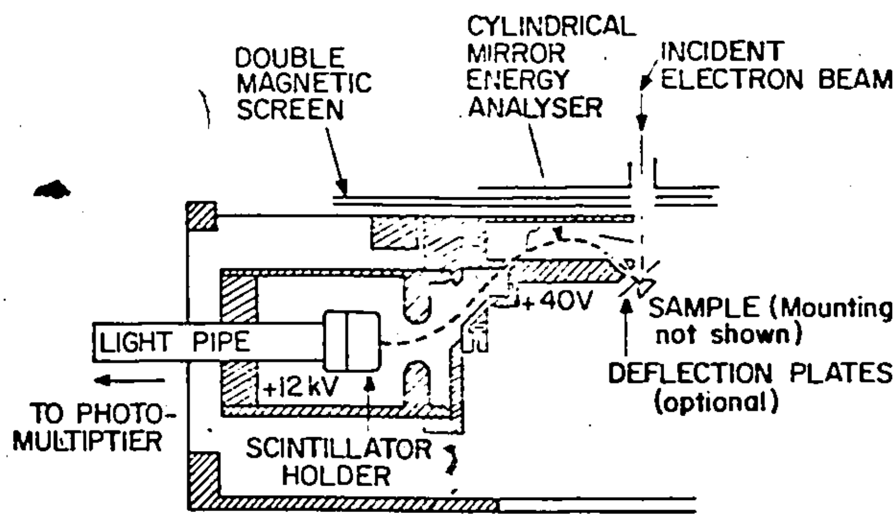

Fig. 3.12

Shows the hemispherical mesh design developed by Driver with energy analysis being performed on the emitted electrons. A large aperture Everhart-Thornley detector system is used as a collector.

Fig. 3.13

Shows Well's and Bremer's 84^{o} deflection electrostatic cylindrical mirror energy analyzer.

the low energy secondary electrons are deflected by the electrostatic field between the upper and lower section of the analyser towards the exit aperture. Depending on the energy of the electrons and the potentials on the analyser, the electrons may pass through the exit aperture and be collected by the scintillator of the modified Everhart-Thornley detector. The energy resolution of this type of analyser is determined by the stability of the electrostatic fields and the size of the exit aperture.

Specimen potential measurements are made by locating the peak of the secondary electron distribution and observing the shift in this peak. As pointed out by the authors, changes in the analyser operating characteristics produce changes in both the apparent electron energy spread and in the position of the peak. For this reason, they suggest that the specimen potential should be varied so that the operating characteristic of the analyser can be maintained constant. However, the results discussed in the paper are not obtained in this manner.

It was observed that the signal to noise ratio is degraded by an order of magnitude when the analyser is used compared to the Everhart-Thornley detector alone. By biasing the deflection plates close to the specimen (see Figure 3.13) an improvement in the signal strength was noted. An improvement of up to five times could be observed in this way.

Wells and Bremer list a number of difficulties with the system including an error due to varying the position of incidence of the primary electron beam on the specimen surface, transverse fields at the specimen surface, specimen contamination effects and similar contamination effects on the analyser plates and stray magnetic fields from the final lens of the electron optical column. In addition, these authors discuss the difficulties associated with performing measurements on specimens that have insulated regions which can charge up under the electron beam. A good example of this problem is the ceramic lead-throughs commonly used on integrated circuit packages.

The system is tested by attempting to plot the reverse characteristics of a p-n junction. Good agreement with the known characteristics was obtained. No detailed data on sensitivity, linearity or range was provided.

3.3 Trajectory Sensitive Voltage Contrast Detectors

In the introduction to this chapter, it was indicated how voltage contrast detectors may be classified into two groups; energy sensitive detectors and trajectory sensitive detectors. The Everhart-Thornley detector, although not specifically designed for the detection of voltage contrast, can be used for this purpose and falls into the trajectory sensitive class.

The characteristic curve of this detector has been measured. This curve, relating detected output to specimen potential is shown in Figure 3.14. The detailed shape of the curve depends on the relative positions of the detector and the specimen. It can be seen that this curve is only linear over a very small range of specimen potential. Outside this range, the detector is very non-linear and is therefore unsuitable for quantitative voltage measurement.

In the remainder of this section, the operation and characteristics of other trajectory sensitive detectors are discussed.

3.3.1 The Banbury-Nixon Detector

Banbury and Nixon (3.7) have described a multi-purpose detector for the scanning electron microscope. This detector consists of the cylindrical arrangement of electrodes shown in Figure 3.15. In a second publication (3.11), these authors have described the use of this detector for the observation of voltage contrast.

Voltages are applied to the electrodes producing electrostatic fields which can exercise a wide range of control over the trajectories of the emitted secondary electrons. By varying these applied voltages, it was possible to overcome the effects of transverse fields of almost any magnitude and orientation. The particular combination of a small retarding field at the specimen surface, produced by a negative bias applied to grid four, and a positively biased collector, grid two, reduced the effects of transverse fields while retaining a useful voltage sensitivity. In addition, this technique provided a symmetrical, monotonic characteristic with the highest sensitivity near to the origin as shown in Figure 3.16. By adjusting

FIG. 3.14

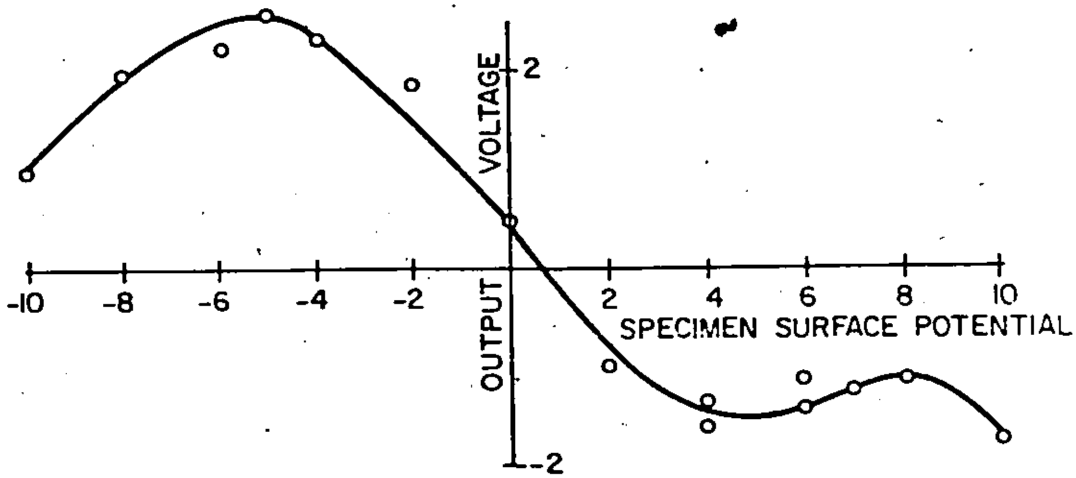

OUTPUT VOLTAGE
2
-2
-10
-8
-6
-4
-2
2
4
6
8
10
SPECIMEN SURFACE POTENTIAL

Fig. 3.14

This figure shows the voltage contrast characteristic for the Everhart-Thornley Detector.

FIG. 3.15

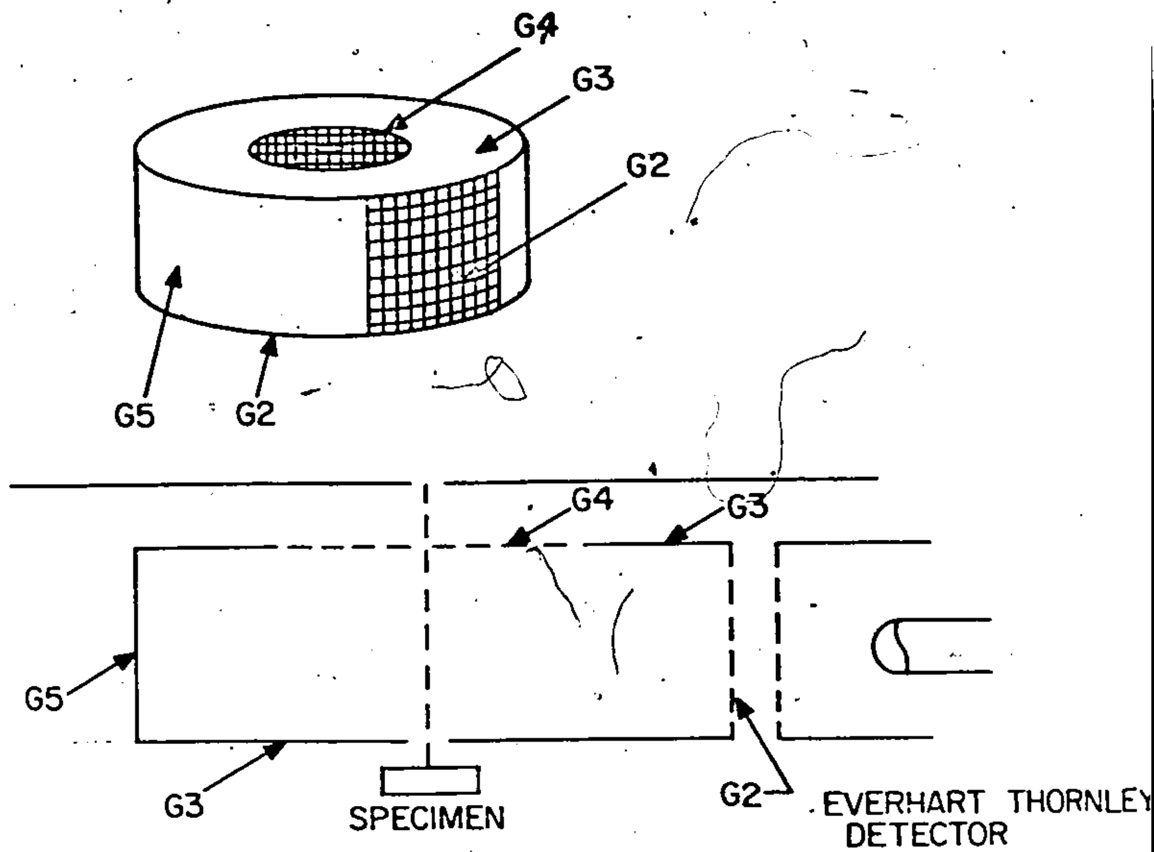

FIG. 3.16

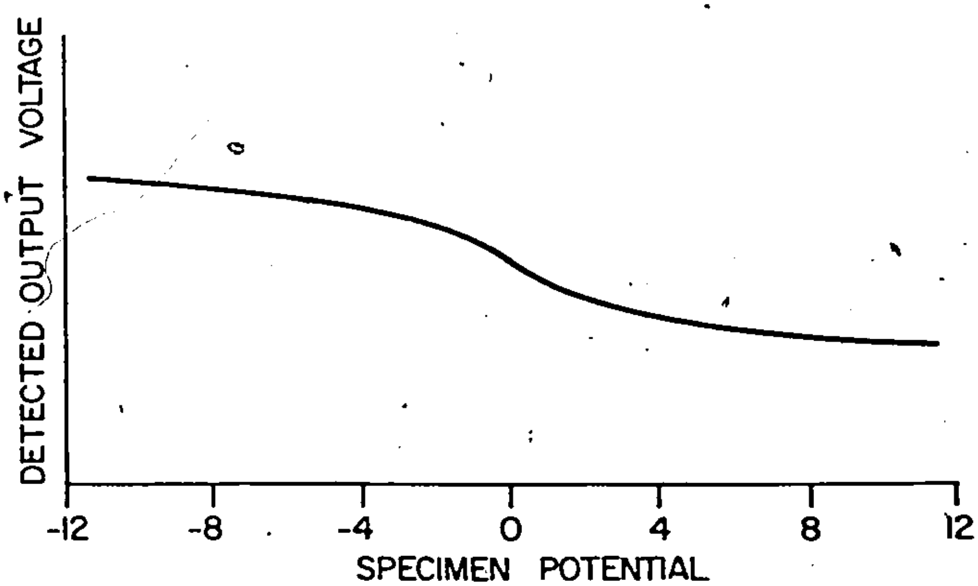

Fig. 3.15

Shows the cylindrical arrangement of detector electrodes developed by Bandbury and Nixon.

Fig. 3.16

Shows the voltage contrast characteristic for the Bandbury-Nixon detector.

the magnitude of the retarding field, a 50% increase in sensitivity could be obtained for a positive specimen bias at the expense of sensitivity in the negative region. The opposite effect could also be produced. A slope of 13% at the origin was achieved in the latter case and 8% in the case of the symmetrical characteristic.

3.3.2 The Beaulieu-Black-Cox Detector

The rectangular arrangement of electrodes shown in Figure 3.17 was developed by Beaulieu et.al. (3.8, 3.9) for the purpose of surface voltage measurements on integrated circuits. In a similar manner to that used by Banbury and Nixon (3.11), the potentials of the back, sides and front mesh (M_1) of the box and the annular electrodes were varied to control the trajectories of the emitted secondary electrons. Mesh M_2 was used as a screen to prevent the high scintillator potential disturbing the potential distribution within the box. The potentials on the electrodes could be chosen so that a nearly normal electric field was produced at the specimen surface. This was verified by plotting the equipotential lines for a two dimensional model of the box using a field plotter. In this way, the effects of transverse fields at the specimen surface were reduced but not entirely eliminated. The specimen potential versus detector output characteristic obtained is shown in Figure 3.18. This characteristic is non-monotonic and in this form is unsuitable for the measurement of voltage contrast.

In order to linearise this characteristic, a feedback control loop was used similar to that described by Gopinath and Sanger (3.10). The detector output is fed back to the first mesh (M_1) which was used as a control grid. Thus, when the surface potential of the specimen is changed, the change in the secondary electron signal output is fed back to the control grid to maintain the input at the photo-multiplier of the Everhart-Thornley type detector system at the same level. A signal processing technique was also used to reduce the topographic content of the detector output signal. This technique is described in section 3.4. The complete arrangement is shown in Figure 3.19.

FIG. 3.17

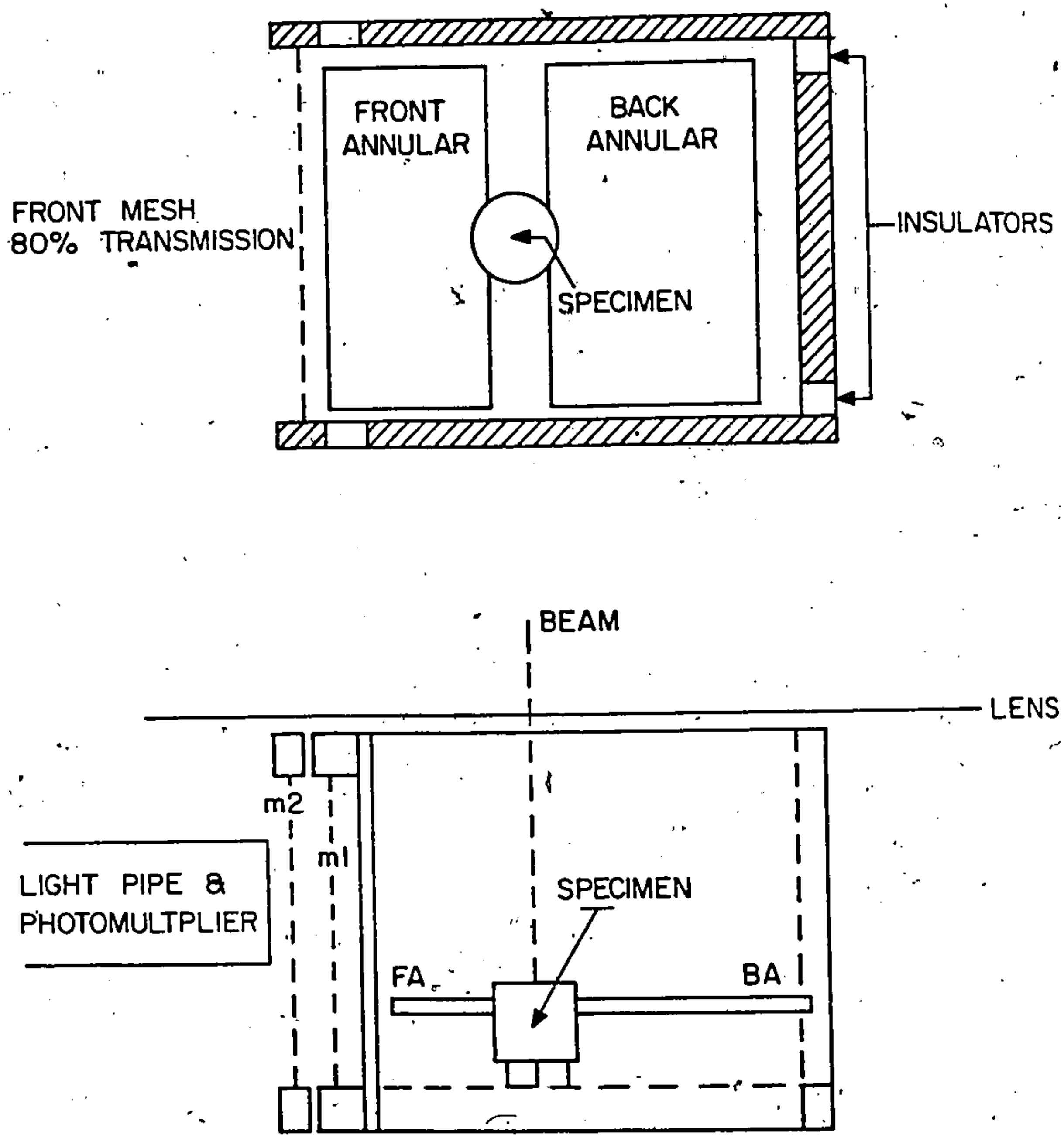
FRONT ANNULAR
BACK ANNULAR
FRONT MESH
80% TRANSMISSION
SPECIMEN
INSULATORS
BEAM
LENS
m2
ml
LIGHT PIPE &
PHOTOMULTPLIER
SPECIMEN
FA
BA

Fig. 3.17

Shows the rectangular arrangement of electrodes designed by Beaulieu, Black and Cox.

FIG. 3.18

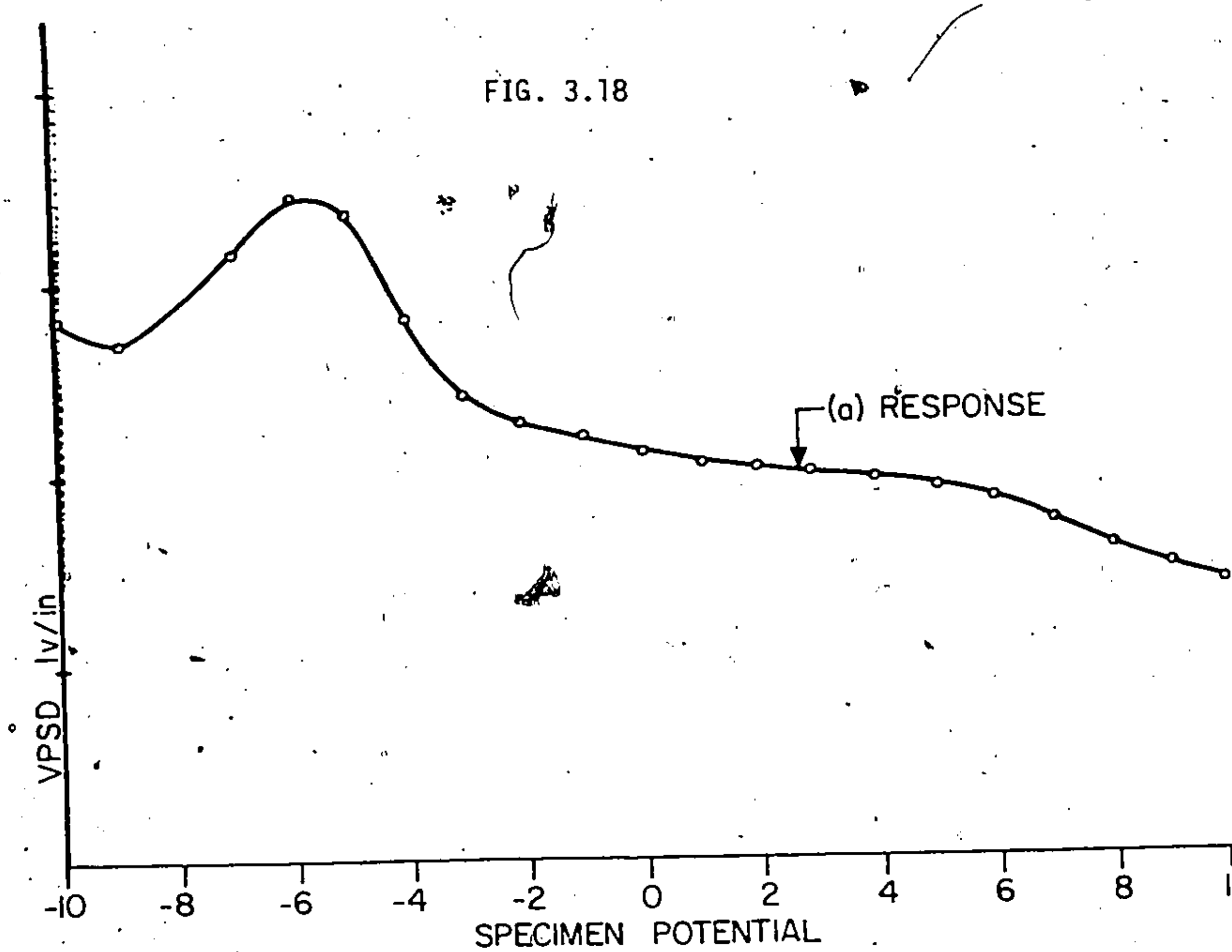

Fig. 3.18

The voltage contrast characteristic for the open loop detector system used by Beaulieu, Black and Cox is shown here.

FIG. 3.19

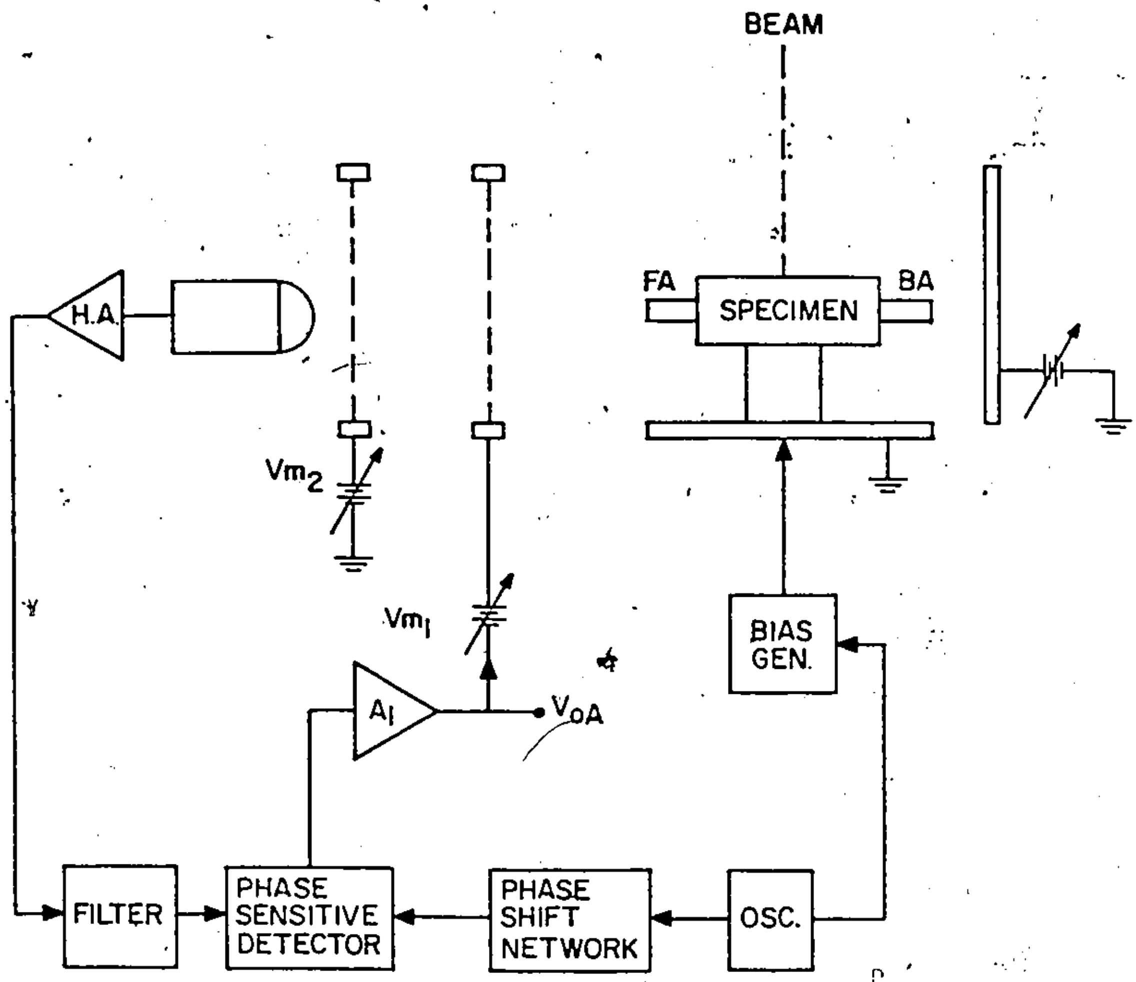
BEAM
FA
SPECIMEN
BA
H.A.
Vm2
Vm1
A1
VoA
BIAS GEN.
FILTER
PHASE SENSITIVE DETECTOR
PHASE SHIFT NETWORK
OSC.

Fig. 3.19

Shows the control loop system used by Beaulieu et. al. A control voltage is applied to the collection mesh (V_{OA}) to linearize the detector signal as the specimen potential varies.

The design of the detector along with the use of feedback leads to a detector characteristic which is nearly linear over a ± 10 volt range of specimen potential. The characteristic is shown in Figure 3.20. This system was used to detect specimen surface potentials as low as 100 mV on a transistor specimen. After calibration, the accuracy of the detector over a range of ± 2 volts was measured. The voltages measured by the detector were consistently low at the ends of this range by as much as 15%. It was suggested that this is due to residual transverse fields as the normal electric field at the surface of the specimen was not sufficiently high to entirely eliminate their effects.

3.4 The Suppression of Topographic Contrast

As discussed in Chapter Two, the secondary electron emission from the specimen in a scanning electron microscope contains a great deal of information on the surface topography of the specimen. However, for surface voltage measurement and the observation of voltage contrast, the variation in the secondary electron signal due to topography must be eliminated if possible as they can hinder, or mask entirely, the effects due to specimen voltage. Gopinath and Sanger (3.10) have suggested a method of reducing the contrast due to topography in the detector output signal. The system is shown in Figure 3.21.

The specimen potential is pulsed at 10 KHz and the detector output signal thus contains both topographic signal and voltage contrast signal during the bias-on periods and topographic signal only during the bias-off periods. The differences between these signals, at 10 KHz, is the required voltage contrast signal alone.

The output of the detector is fed to a band pass filter tuned to 10 KHz which passes the voltage contrast signal only. This signal is symmetric about zero, i.e. the phase or polarity information has been lost. In order to recover this, the symmetric signal is detected using a phase sensitive detector with a reference input derived from the specimen bias pulse circuitry via a phase shifter to compensate for signal delays. Using this technique, the topographic signal is reduced, aiding the observation of the surface voltage contrast component.

FIG. 3.20

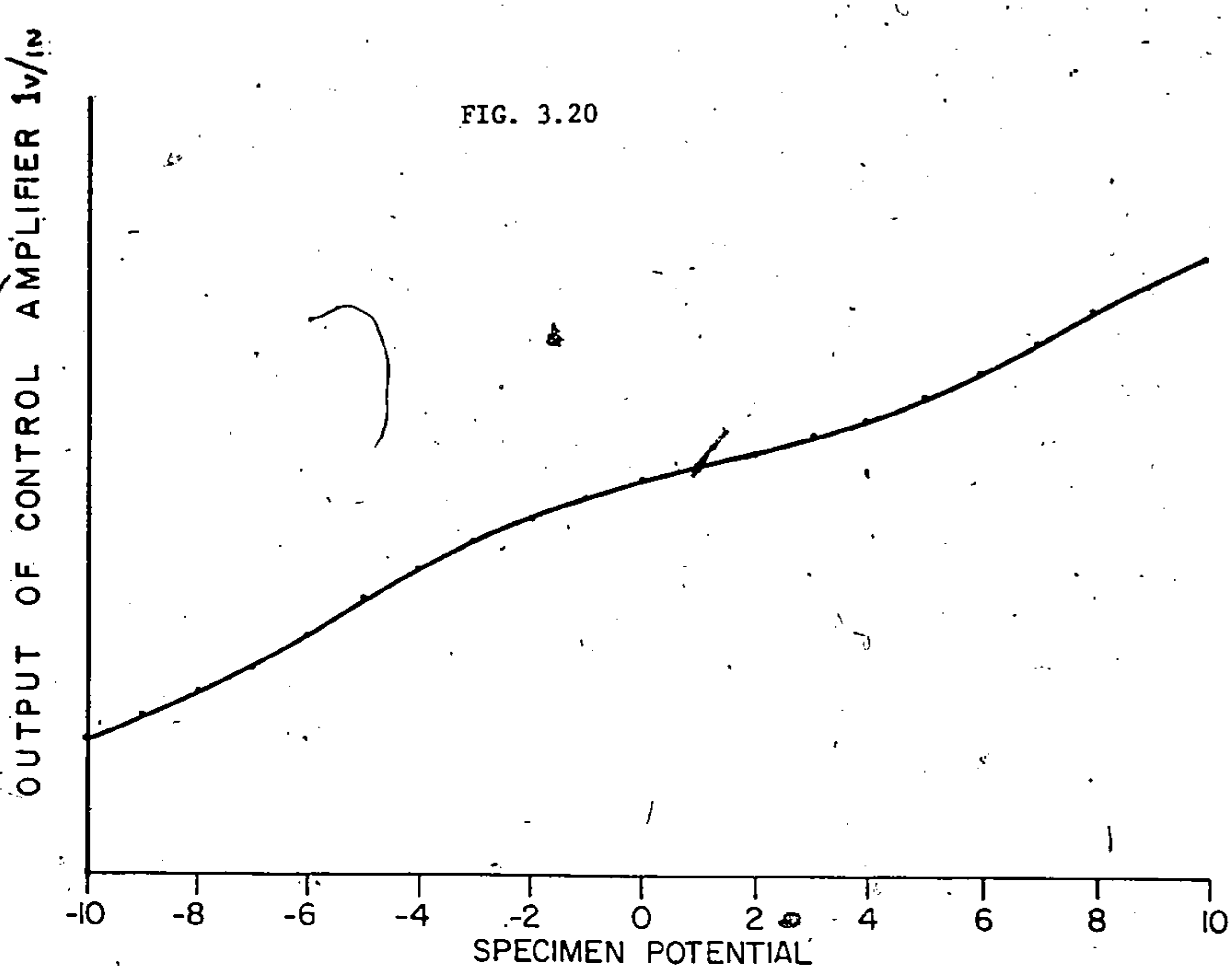

FIG. 3.21

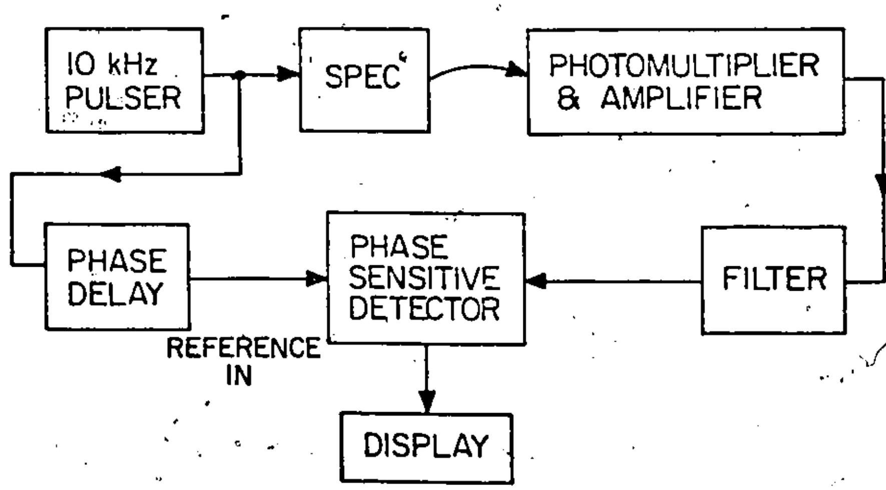

Fig. 3.20

This figure shows the voltage contrast characteristic obtained using the feedback control loop, Beaulieu et.al.

Fig. 3.21

Shows the technique used to suppress topographic contrast, a technique developed by Gopinath and Sanger.

3.5 The New Voltage Sensitive Detector

Based on the review of published work on voltage sensitive detectors above, and referring to the specification required of a measuring system suggested in Chapter 1, it is possible to arrive at a set of required specifications for a new detector system. They are discussed in some detail below.

3.5.1 Design Criteria

a) Accuracy, Linearity and Range

Plows and Nixon (3.2) have achieved a linearity of 17% over a 4 volt range of specimen potential. By using a linearisation technique, this value was improved with some sacrifice in sensitivity. Banbury and Nixon (3.7) achieved a linearity of 13% over a ± 2 volt range of specimen potential. This was achieved without the use of electronic linearisation. The other papers discussed did not provide details of the linearity and range achieved.

The figures quoted above are of little use for performing routine voltage measurements on integrated circuits. A range of +20 volts to −20 volts is needed in order to cover the range of voltages typically used for rail and bias voltages in operational amplifiers and digital integrated circuits. An accuracy of ± 5% of full scale, i.e. ± 1 volt in 10 volts is needed for most general work. A second range of ± 2 volts with an accuracy of ± 2.5% of full scale i.e. ± .05 volts in 2 volts, is needed for more accurate studies.

These figures imply a linearity of ± 5% over the entire range of ± 20 volts and ± 2.5% over a range of ± 2 volts. These requirements are considerably better than have been achieved to date. The attainment of good linearity allows the detector output to be used directly, avoiding the use of calibration curves or complex electronics. However, for very accurate work over the entire range, a calibration curve could be used.

b) Sensitivity, Signal to Noise Ratio and Beam Current

The sensitivity of a voltage sensitive detector system can be defined as the smallest voltage or change in voltage that can be detected or displayed. Beaulieu, Black and Cox (3.8) have succeeded in displaying potentials as low as 10 mV, however, for the majority of studies, a sensitivity of 100 mV would be acceptable. For example, this sensitivity would allow the potential drop across a silicon p-n junction (600 mV) to be observed with ease.

The sensitivity of a given detector is governed by the signal to noise ratio of the system. An expression for this can be derived as follows. If the primary beam current incident upon the sample is I_b amps., then the number of electrons incident per second is I_b/e, where e is the electronic change. The number of secondary electrons emitted per second is given by $I_b\delta/e$ where δ is the secondary electron yield (see Chapter Two). If R is the fraction of the emitted secondary electrons collected and detected, then the total number detected per second is $I_b\delta R/e$.

If we now consider the displayed image to be composed of an array of 500 x 500 picture elements and if the time to scan one complete raster is T secs, then the number of electrons collected from each picture element, N, is given by: (3.11)

$$N = \frac{I_b \cdot \delta R \cdot T}{(500)^2 e} \qquad \text{eq. 1}$$

The r.m.s. fluctuation in N will be $\sqrt{N}$ so that $\frac{N}{\sqrt{N}}$ or $\sqrt{N}$ represents the basic signal to noise ratio of the element being scanned. This signal to noise ratio, S:N is given by

$$S{:}N = \frac{1}{500} \left(\frac{I_b \delta RT}{e}\right)^{\frac{1}{2}} \qquad \text{eq. 2.}$$

This represents the signal to noise ratio due to the shot noise contribution of the primary electron beam. However, the generation of secondary electrons is itself a random process and will also contribute noise. Peace (3.12) has determined that this noise contribution will degrade the basic signal to noise ratio of eq. 2 by a factor of 4. Thus

$$S{:}N = \frac{1}{2 \times 10^3} \left(\frac{I_b \delta RT}{e}\right)^{\frac{1}{2}} \qquad \text{eq. 3}$$

This equation shows that the signal to noise ratio can be optimised by using a large beam current, ensuring that the collection factor of the detector system is as high as possible and by using a long frame scan time. In addition, the use of a fairly low value of beam energy (approximately 2 KeV) will maximise the value of

δ, the secondary electron yield (see section 2.2:1).

Increasing the primary beam current I_b, increases the electron beam size and reduces the spatial resolution of the SEM. If a spatial resolution of 1000 Å is chosen, then a beam current of the order of 10^{-9} amps. can be used. For the present following Everhart (3.15), the value of δ will be taken as 0.3 which is a satisfactory value at high beam energy (15 to 20 KeV). The average value of the collection factor, R, will be chosen conservatively as 10%.

Substituting these values into equation 3, we can arrive at a relationship between the signal to noise ratio and the frame scan time.

$$S:N = \frac{10}{\sqrt{2}} \; T^{\frac{1}{2}} \qquad \text{eq. 4}$$

The relationship between the signal to noise ratio and the detection of contrast in an image has been studied by Rose (3.13). He found that the minimum contrast that could be detected by the eye was inversely proportional to the signal to noise ratio. This minimum contrast is known as the threshold contrast C_T. Thus

$$C_T = \frac{K}{S:N}$$

where the proportionality constant was found to be close to 5.

If a value of C_T equal to 0.05 is accepted, i.e. 5% changes in voltage being detectable, then a signal to noise ratio of 100 is required. Substituting this value into equation 4 yields a frame scan time of 200 secs. This is an acceptable value.

A micrograph displaying 5% changes in voltage level could therefore be obtained in 200 secs. assuming the values discussed above. Under these conditions, the sensitivity of the detector over the two ranges discussed in the previous paragraph would be ; 1 V in 20 V and .1 volts in 2 volts when a micrograph was required. These values seem reasonable as a 10 mV sensitivity has already been achieved with a frame scan time of 100 secs. (3.9).

If a point measurement, rather than a micrograph were required, then significantly better sensitivity could be expected as the time taken to perform the measurement could be made as long as is consistent with system stability.

c) System Response Time

The response time required of the system can be calculated from the data above. A picture composed of $(500)^2$ picture elements is to be produced in 200 secs. This means that the electron beam spends .8 msecs on each picture element. In general terms, the system should respond in approximately one tenth of this time, implying a response time of 80 μsecs. maximum.

d) Suppression of Interfering Effects

One of the most troublesome effects described by the other workers is that of local transverse electric fields at the specimen surface. These fields, which can obscure the observation of voltage contrast have been controlled by the application of a strong normal electric field at the specimen surface. Such a field has been generated by the use of a cage structure (3.10) surrounding the specimen and by means of a parallel electrode or grid. Both of these methods have met with success and a similar technique must be adopted in the present detector design.

Another effect which was described, was the presence of topographic information in the secondary electron signal as well as the required voltage contrast. This signal was suppressed by the use of a modulation technique. However, in order to obtain optimum results from a voltage sensitive detector, it is necessary to eliminate all sources of signal other than the secondary electron signal carrying the voltage contrast information. This means that backscattered electrons, tertiary electrons and all sources of secondary electrons produced by both backscattered electrons and tertiary electrons must be eliminated and not contribute to the detector output signal (see section 2.4). This is an important requirement of the present detector design.

e) Other Requirements

It is desirable that the geometry of the detector be suited to the existing arrangement of specimen chamber, specimen stage, final lens pole piece and secondary electron photomultiplier and head amplifier assembly so that no major modifications are required to fit the new detector system. The detector should also allow the specimen to be changed easily and quickly. This is required so that the detector can finally be used in a production control environment.

The detector should interfere with the normal operation of the SEM as little as possible. Ideally, conventional topographic images should be available from the detector in addition to the voltage contrast displays.

Finally, the area on the specimen over which voltage measurements can be made should be as large as possible consistent with the accuracy requirements stated in paragraph (a) above. Ideally, this area should be of the order of 2.5mm x 2.5mm in order to cover the majority of integrated circuit chips.

3.5.2 The Proposed Detector

A schematic diagram showing the arrangement of the new detector is shown in Figure 3.22. An electrode is used, parallel to the specimen surface, to provide a high normal electric field at the specimen surface to reduce the effects of transverse fields. The secondary electrons emitted are accelerated from the surface towards this electrode and pass through a hole into an electrostatic field-free box maintained at the same potential as the accelerating electrode. A lateral magnetic field in this box deflects the bundle of secondary electrons towards an aperture in the side of the box, effectively separating the secondary electron signal from all other possible signals. Some of the electrons pass through this aperture and are detected by a scintillator-light-guide-photomultiplier assembly.

Changes in the specimen surface potential produce changes in the energy of the secondary electrons entering the box as the electrostatic field between the specimen and the accelerating electrode (the bottom of the box) is changed. As the energy of the electrons is varied, the deflection in the magnetic field is varied, and the electron bundle moves with respect to the aperture. As the secondary electron bundle moves over the aperture, a signal variation is produced which is related to the variation in specimen potential.

This arrangement, which is essentially a simple secondary electron spectrometer, will detect only secondary electrons emitted from the specimen surface.

FIG. 3.22

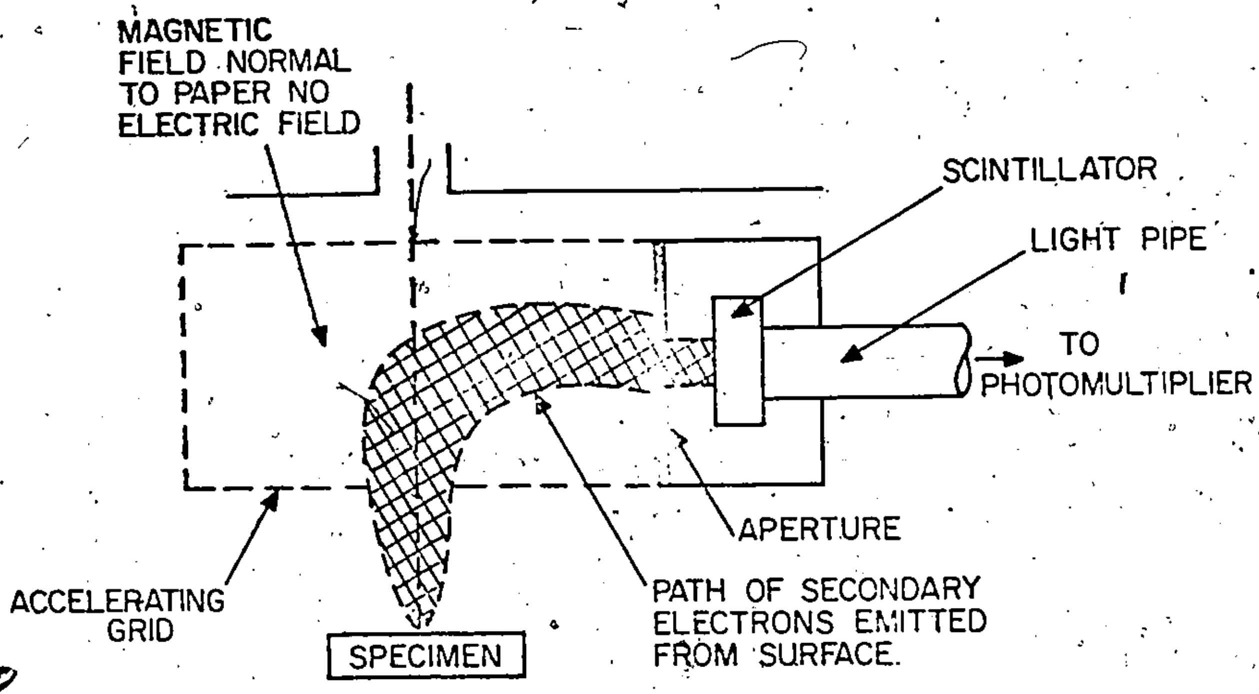
MAGNETIC FIELD NORMAL TO PAPER NO ELECTRIC FIELD
SCINTILLATOR
LIGHT PIPE
TO PHOTOMULTIPLIER
APERTURE
ACCELERATING GRID
SPECIMEN
PATH OF SECONDARY ELECTRONS EMITTED FROM SURFACE.

Fig. 3.22

This figure shows the proposed detector design using a magnetic field to separate the secondary electrons from backscattered and tertiary electrons.

Backscattered and tertiary electrons, because of their higher energies will not be deflected sufficiently in the magnetic field to pass through the aperture. Secondary electrons produced by backscattered electrons on the inside top surface of the box will be deflected away from the aperture towards the opposite end of the box. In fact, secondary electrons produced on all the inside surfaces of the box will not have the correct direction of travel or the correct energy (as they have not been accelerated through the electrostatic field) and hence they will not be directed towards the aperture plane by the magnetic field.

This method will eliminate all spurious signals except the topographic information in the secondary electron signal which can be rejected by using the modulation technique and phase sensitive detection technique already described above (3.6).

The detector geometry is ideally suited for use in a conventional SEM without the need for any major modification. It is proposed that the detector be mounted on the base of the electron optical column and that the specimen be mounted on the normal specimen stage. This will ensure that specimen changing and manipulation is nor more difficult than with the conventional SEM.

The primary electron beam passes through the lateral magnetic field and will therefore suffer a deflection. However, this can be compensated for in the location of the aperture in the lower surface of the box. The deflection of the primary beam and the use of a long working distance will degrade the resolution of the SEM. It is unlikely that the resolution will be worse than the required 1000 Å however. The response time of such a system will be limited by the scintillator-light-guide-photomultiplier detector. This has a bandwidth of at least 8 MHz and so the response time of the system should be entirely satisfactory.

The brief introduction to the new detector illustrates how it meets many of the requirements specified. The sensitivity, linearity and range etc. can only be determined by testing a prototype unit. Before implementation of this design in the form of a test detector, the behaviour of electrons in electric and magnetic fields was studied. The results of this study are discussed in the next chapter.

CHAPTER FOUR

The Motion of Electrons in Electrostatic and Magnetic Fields

Introduction

The proposed design for the new voltage contrast detector was introduced in the latter section of Chapter Three. Before such a detector can be designed, the motion of electrons in both electrostatic and magnetic fields must be studied in order to arrive at an optimum set of design parameters. This chapter describes the studies that were performed and the conclusions reached.

In the first section the detector model studied is described. The following section investigates the behvaiour of electrons in crossed electric fields. Such fields exist at the surface of a specimen due to transverse and accelerating fields. The final part of the chapter deals with electron motion in a magnetic field.

4.1 The Detector Model

The model of the detector shown in Figure 4.1 is to be studied. In the presence of transverse fields, secondary electrons are emitted into a crossed electrostatic field at the specimen surface because of the transverse fields and the accelerating field due to the potential, V_m, applied to the lower mesh of the detector. The secondary electrons are extracted from the influence of the transverse fields by the accelerating field and pass through the accelerating mesh into the region of the magnetic field. Here the secondary electrons of low energy are deflected more than the higher energy backscattered and tertiary electrons, see Figure 4.1. If the strength of the magnetic field is adjusted so that the secondary electrons are deflected through approximately 90^o, then only the secondary electrons emitted from the specimen will pass through the aperture and be detected. All other low energy electrons (for example, secondary electrons produced on the pole piece by backscattered electrons from the specimen) will be deflected away from the aperture, see Figure 4.1.

The analysis of the motion of electrons in the various regions of the

Fig. 4.1

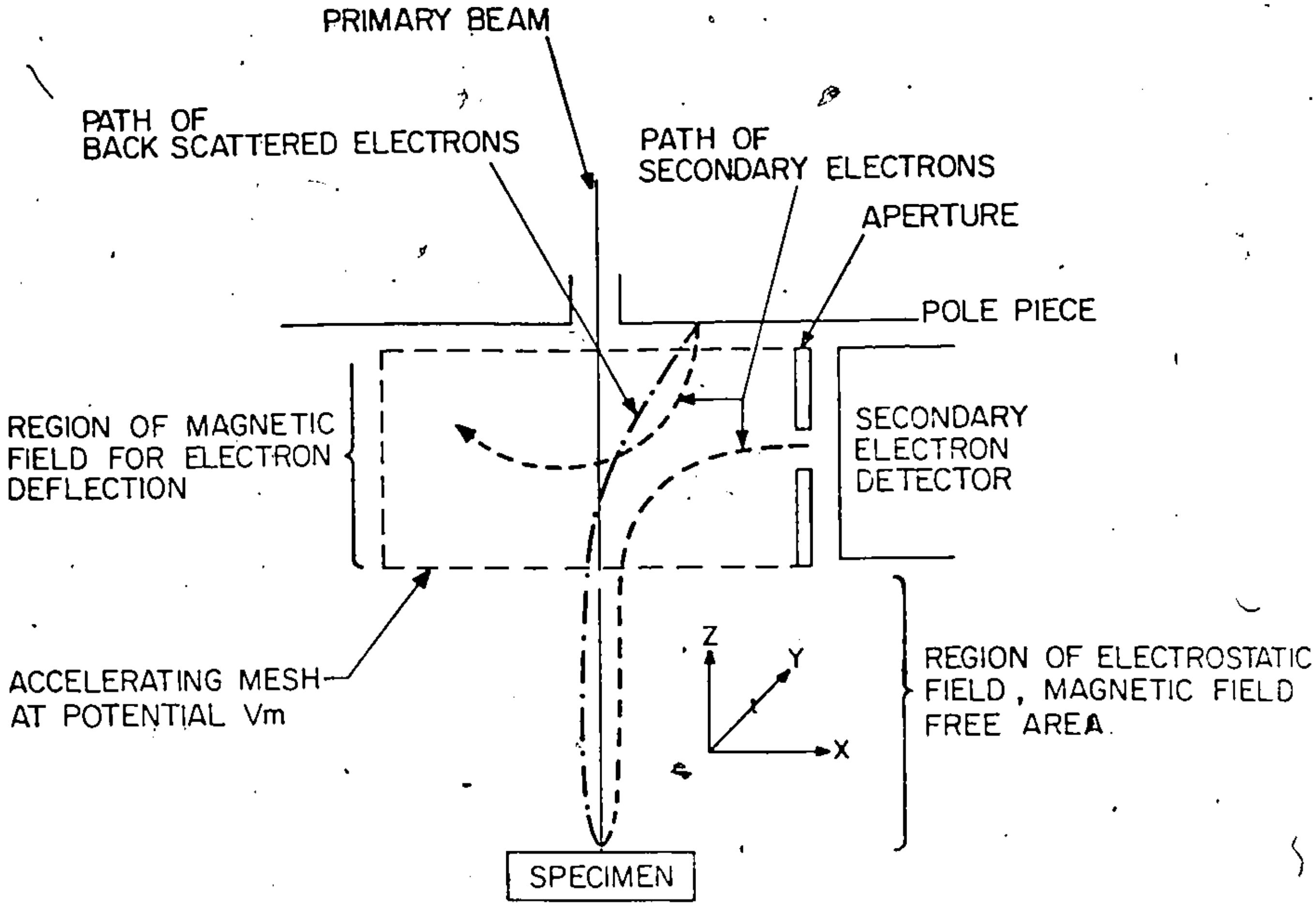
PRIMARY BEAM
PATH OF
BACK SCATTERED ELECTRONS
PATH OF
SECONDARY ELECTRONS
APERTURE
POLE PIECE
REGION OF MAGNETIC
FIELD FOR ELECTRON
DEFLECTION
SECONDARY
ELECTRON
DETECTOR
Z
Y
X
ACCELERATING MESH
AT POTENTIAL Vm
REGION OF ELECTROSTATIC
FIELD, MAGNETIC FIELD
FREE AREA.
SPECIMEN

Fig. 4.2

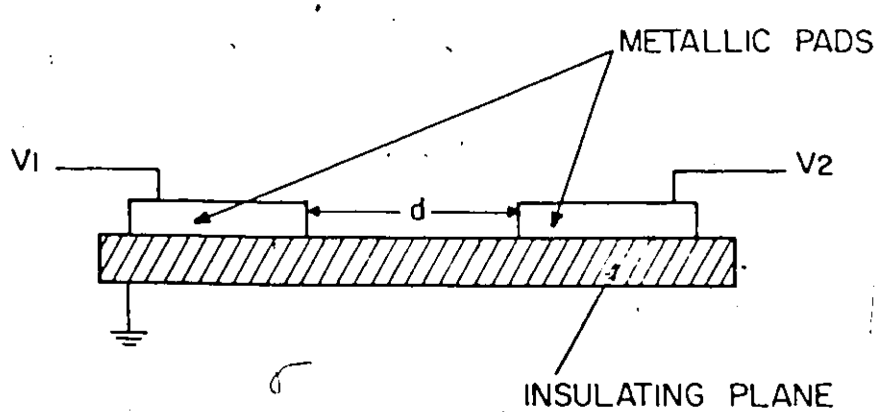
METALLIC PADS
V1
V2
d
INSULATING PLANE

Fig. 4.1

Shows the model of proposed detector design studied using the computer programs.

Fig. 4.2

This figure shows the surface electrode configuration studied during the analysis.

detector will be described. First of all, their behaviour in the crossed electrostatic fields at the specimen surface will be discussed.

4.2 Trajectory Analysis in Crossed Electric Fields

In order to analyze electron trajectories in the region of crossed electric fields, the geometry of electrodes shown in Figure 4.2 was used. Although this geometry is very simple, it offers a good approximation to the geometry found in reality on a typical integrated circuit.

Because of the complex fields generated between these electrodes and the accelerating mesh, it is difficult to perform either a rigorous mathematical analysis or experimental field plots to determine the field configuration. It is therefore necessary to approximate the field conditions near the specimen surface and the following assumptions will be made.

Since the ratio of the distances between the surface electrodes and the plane of the accelerating mesh is very large, it will be assumed that the shape of the transverse fields is not distorted by the accelerating field. If the analysis is performed in the x, z plane (see Figure 4.1) then the net field is the vector sum of its x and z components assuming that the y components are zero, i.e. the net field is composed of E_{ZA}, the accelerating field vector, and E_Z and E_X, the components of the transverse field in the Z and X directions respectively. These fields and their components are shown in Figure 4.3. Also shown in Figure 4.3 is that the angle between the local direction of the transverse or micro-field and the surface, angle AMF, varies with the point of study chosen on the metallic pad. The differential equations describing electron motion in fields of this type are as follows:

$$\frac{d^2x}{dt^2} = A\ E_o \exp\left(\frac{-Z}{2d}\right) \cos AMF \qquad \text{eq. 4.1}$$

$$\frac{d^2Z}{dt^2} = A\ (E_{ZA} + E_o \exp\left(\frac{-Z}{2d}\right) \sin AMF) \qquad \text{eq. 4.2}$$

where A is the charge to mass ratio, E_o is the magnitude of the transverse field at the surface, AMF is the angle subtended by the transverse field at the surface, d is the separation of the electrodes and E_{ZA} is the accelerating field due to the

Fig. 4.3

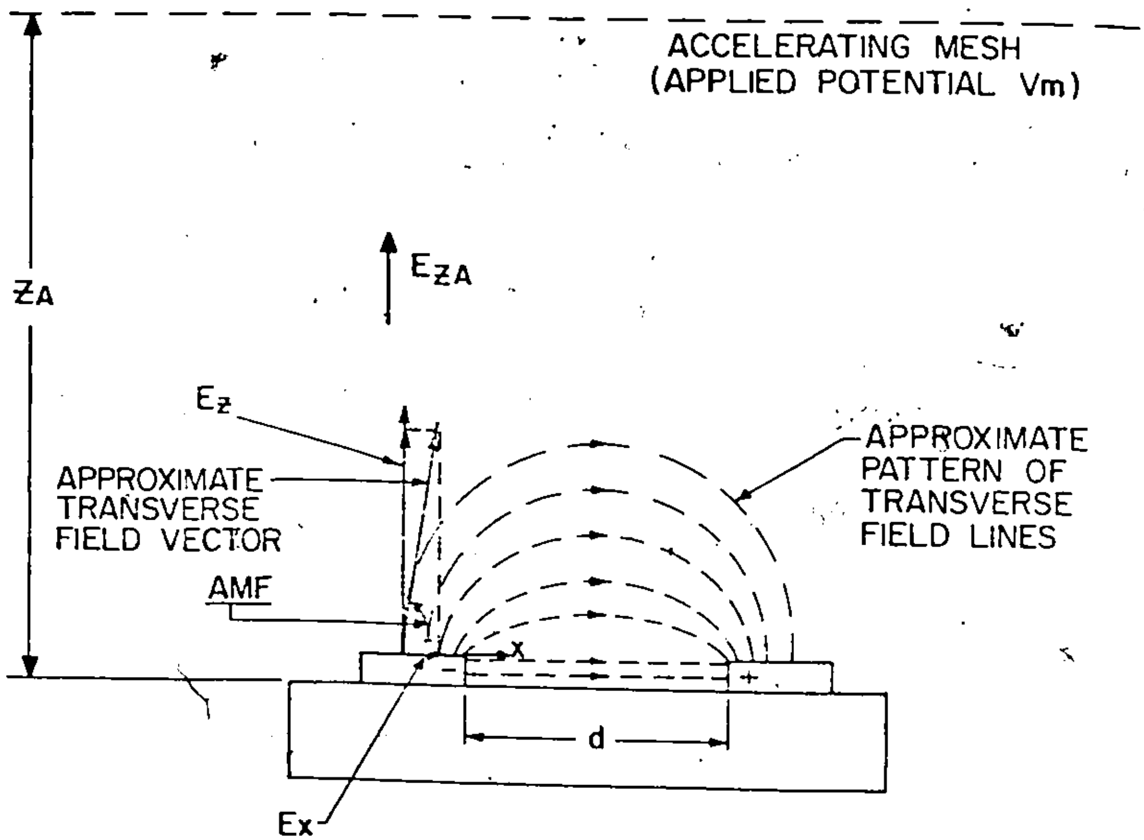

ACCELERATING MESH
(APPLIED POTENTIAL Vm)
E_{ZA}
Z_A
E_z
APPROXIMATE TRANSVERSE FIELD VECTOR
AMF
APPROXIMATE PATTERN OF TRANSVERSE FIELD LINES
x
d
Ex

Fig. 4.3

Shows the coordinate system used for the study of transverse fields, AMF being the angle of entrance or exit of the micro-field with E_x and E_y the horizontal or vertical components of this microfield.

lower mesh of the detector. These equations are developed in Appendix I.

When varying angles and directions of transverse fields are considered, the solution of equations 4.1 and 4.2 becomes complex. With the aid of an analogue simulator program (see Appendix I), these equations were solved using a digital computer. A wide range of conditions was studied and the following results were obtained.

When the specimen at the point of beam incidence is negative, the transverse field lines emerge from the surface and the vertical component of this field, E_Z, will aid the accelerating field E_{ZA}, whereas the horizontal component E_X will, in general, generate a horizontal component to E_{ZA} and E_Z. If these field lines are assumed to be linear in the region of influence of the transverse field and emerge at the angle AMF, then the degree of electron deflection will depend on the angle AMF, the magnitude of the transverse field components, which depends on the potential difference between the metallic pads, V_d, and their spacing, d, and on the accelerating field strength, E_{ZA}, which depends on the specimen to accelerating mesh spacing, Z_A, and the potential on the mesh, V_m.

The degree of electron deflection, measured at the plane of the accelerating mesh, $Z = Z_A$, versus the specimen potential difference, V_d, is shown in Figure 4.4(a). The point of study in this case was the negative pad, i.e. with transverse field lines leaving the specimen and the vertical component of this field aiding the accelerating field. Electrons of emission energy 2 eV, emitted normal to the surface were studied. The other conditions are tabulated in the figure. These curves show that a linear relationship exists between the deflection produced and the specimen potential V_d for various values of AMF and V_m. Figure 4.4 (b) shows the variation of this deflection with the accelerating potential, V_m. It can be seen that as this potential is increased, the deflection is rapidly reduced.

The curves shown in Figures 4.4 (a) and (b) indicate that the effect of the transverse field under these conditions is to produce a deflection of the emitted electrons and a consequent distortion of the electron density distribution in the plane studied. It is also evident that the effect of the transverse fields can be reduced

Fig. 4.4 a)

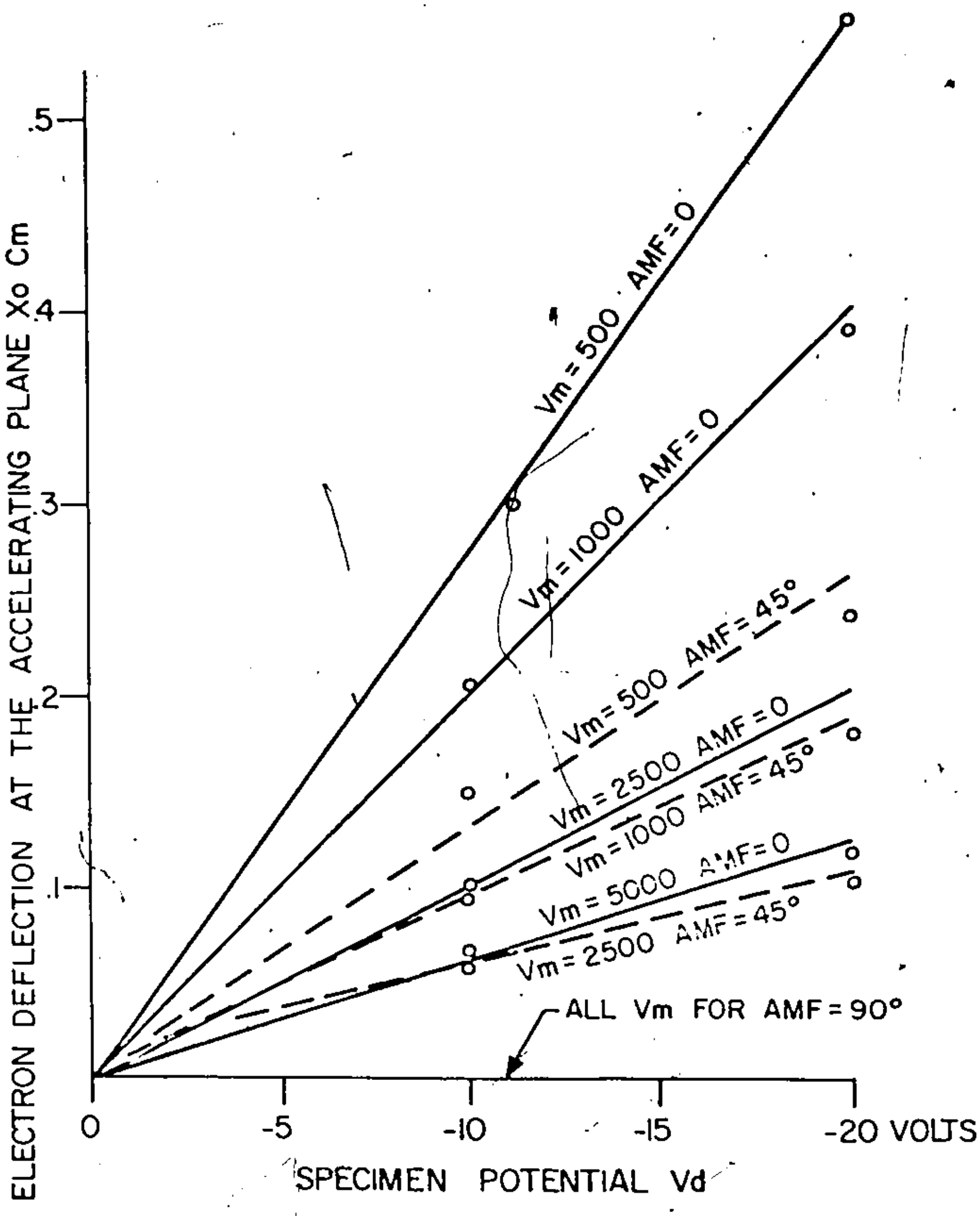

ELECTRON DEFLECTION AT THE ACCELERATING PLANE Xo Cm
.5
.4
.3
.2
.1
Vm = 500 AMF = 0
Vm = 1000 AMF = 0
Vm = 500 AMF = 45°
Vm = 2500 AMF = 0
Vm = 1000 AMF = 45°
Vm = 5000 AMF = 0
Vm = 2500 AMF = 45°
ALL Vm FOR AMF = 90°
0
-5
-10
-15
-20 VOLTS
SPECIMEN POTENTIAL Vd

Fig. 4.4(a)

This graph plots the specimen potential U_d versus electron deflection at the accelerating mesh plane.

angle of emission = 90^o
ZA = 1.27×10^{-2} meters
d = 2.54×10^{-5} meters
Emission energy = 2 ev.

FIG. 4.4(b)

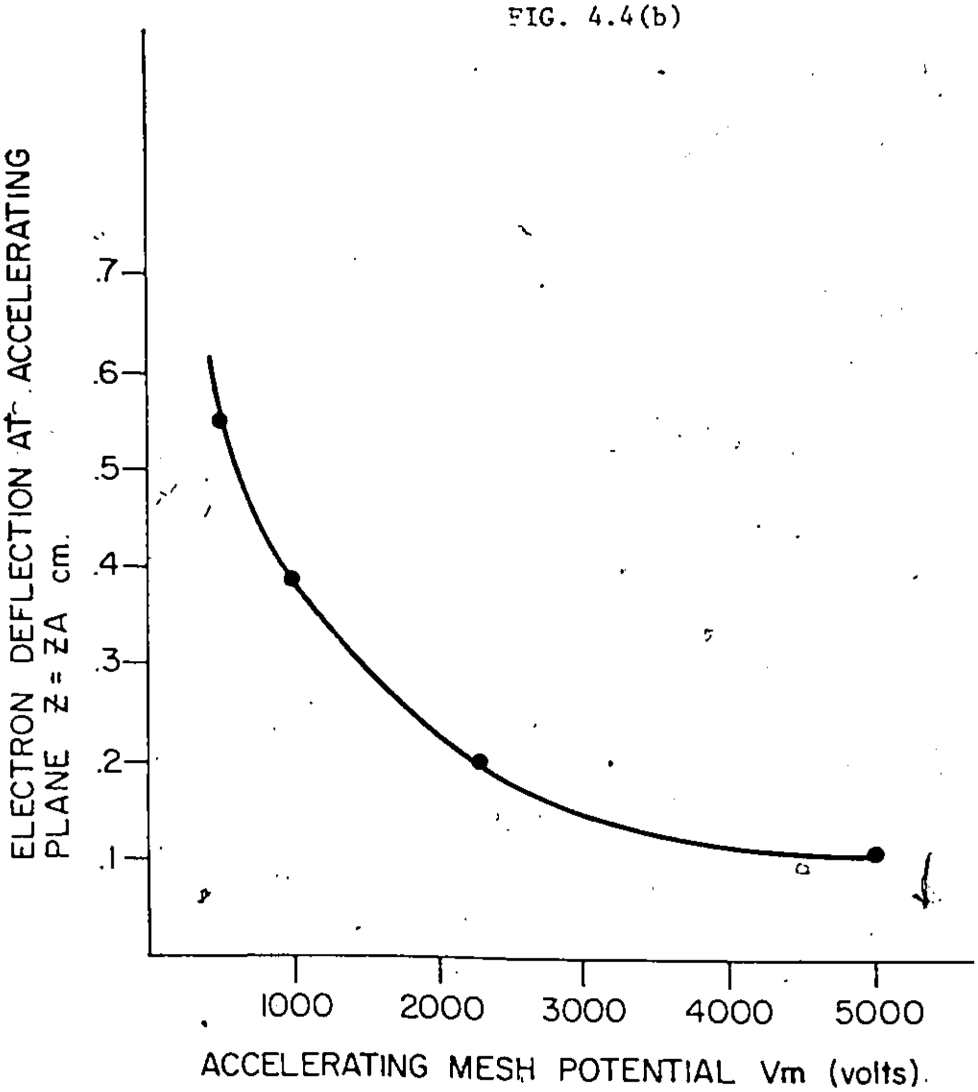

ELECTRON DEFLECTION AT ACCELERATING PLANE Z = ZA cm.
.7
.6
.5
.4
.3
.2
.1
1000
2000
3000
4000
5000
ACCELERATING MESH POTENTIAL Vm (volts)

Fig. 4.4(b)

This graph plots the accelerating mesh potential versus electron deflection of the accelerating mesh plane.

U_d = - 20.0 volts

AMF = 0.0°
Emission angle = 0.0
Emission energy = 2 ev
d = 2.54×10^{-5} meters
ZA = 1.27 cm.

Fig. 4.5

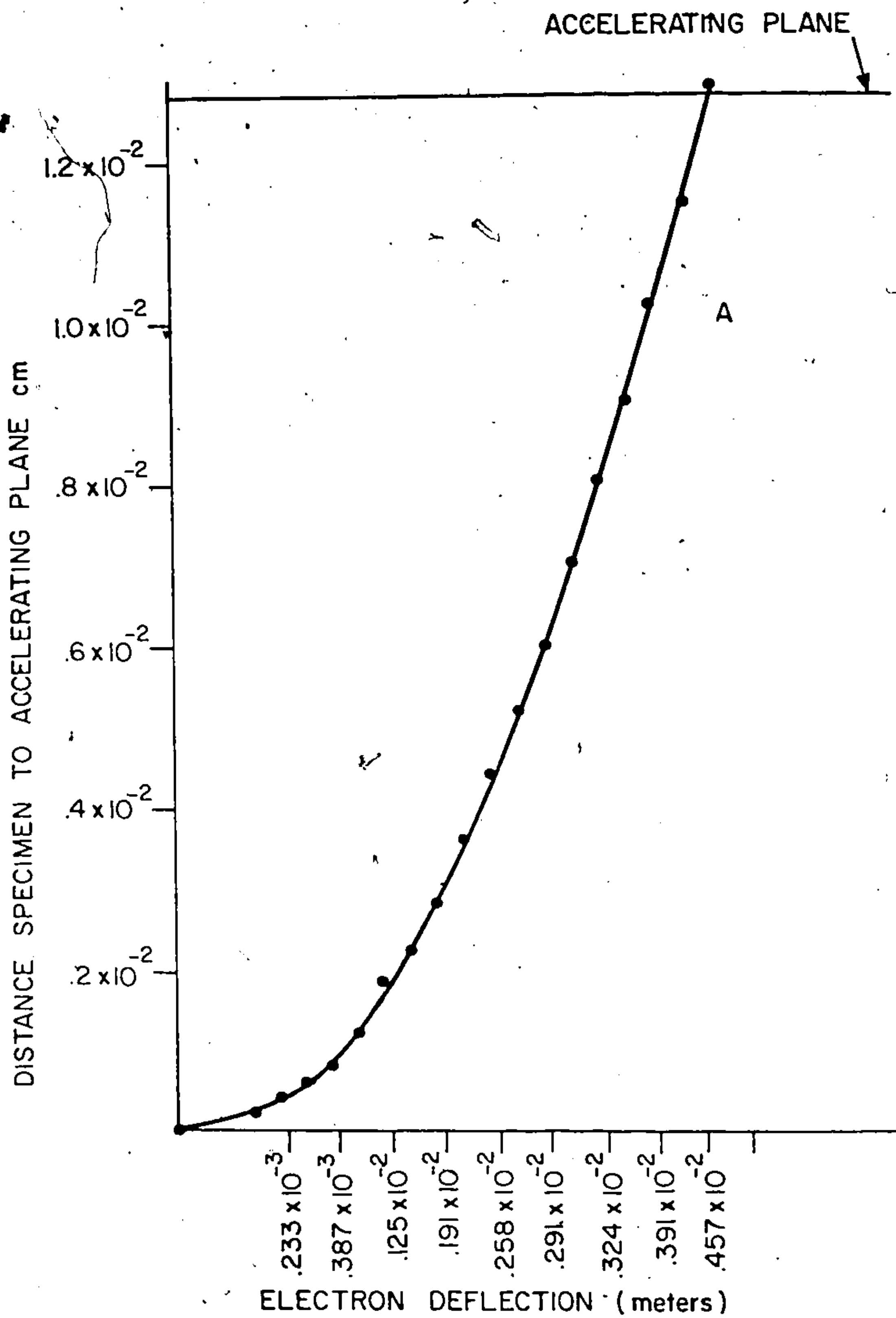
ACCELERATING PLANE
A
1.2 x 10^-2
1.0 x 10^-2
.8 x 10^-2
.6 x 10^-2
.4 x 10^-2
.2 x 10^-2
DISTANCE SPECIMEN TO ACCELERATING PLANE cm
.233 x 10^-3
.387 x 10^-3
.125 x 10^-2
.191 x 10^-2
.258 x 10^-2
.291 x 10^-2
.324 x 10^-2
.391 x 10^-2
.457 x 10^-2
ELECTRON DEFLECTION (meters)

Fig. 4.5

This figure shows an example of an electron trajectory in an aiding transverse field.

AMF = 0^o
Ud = -20 volts
Um = 500 volts
ZA = 1.27 cm.
Emission energy = 2 ev
Angle of emission = 90^o
d = 2.54×10^{-5} meters.

by the use of a high value of V_m, the accelerating mesh potential.

An example of a calculated electron trajectory under these conditions is shown in Figure 4.5. An abrupt change of slope in the trajectory at approximately 10^{-3} cm from the surface indicates that the effects of transverse fields are limited to a region very close to the specimen surface.

If the emission of electrons from the positive pad is considered, then the transverse field terminates at the surface and its vertical component, E_Z is opposed to E_{ZA}, while the horizontal component produces a deflection similar to that observed in the case considered above.

Because the vertical component of the transverse field now opposes the accelerating field, the magnitude of these two fields and the energy and angle of emission of the electron will determine whether or not it will reach the accelerating mesh. For a given set of conditions, there will be a critical value of accelerating field, E_{CRIT}, such that an electron will just reach the accelerating mesh. If the vertical component of the transverse field is changed such that $E_Z > E_{CRIT}$ then the electron will be reflected back to the specimen surface whereas if $E_Z < E_{CRIT}$ then the electron will pass through the accelerating mesh.

The behaviour of an electron emitted normally with an energy of 2 eV from the surface of a pad biased at +20 volts with respect to the other pad (see Figure 4.2) was studied. The value of E_{CRIT} as a function of AMF is shown in Figure 4.6. It can be seen, as might be expected, that as the angle of the transverse field increases (i.e. as the field becomes perpindicular with the surface), the value of E_{CRIT} increases also. Figure 4.7 shows the deflection of the electron in the plane at Z = ZA as a function of specimen potential difference, V_d, at various values of AMF. These curves were derived at a value of accelerating field equal to E_{CRIT} at V_d = +20 volts. The deflection of the electron increases with the potential difference, V_d, and also with decreasing values of AMF, again as may be expected.

Figure 4.8 shows an example of a computed electron trajectory where the value of E_Z is greater than E_{CRIT}. As can be seen, the electron is deflected back to the specimen surface and thus will not be collected and detected. The conditions

Fig. 4.6

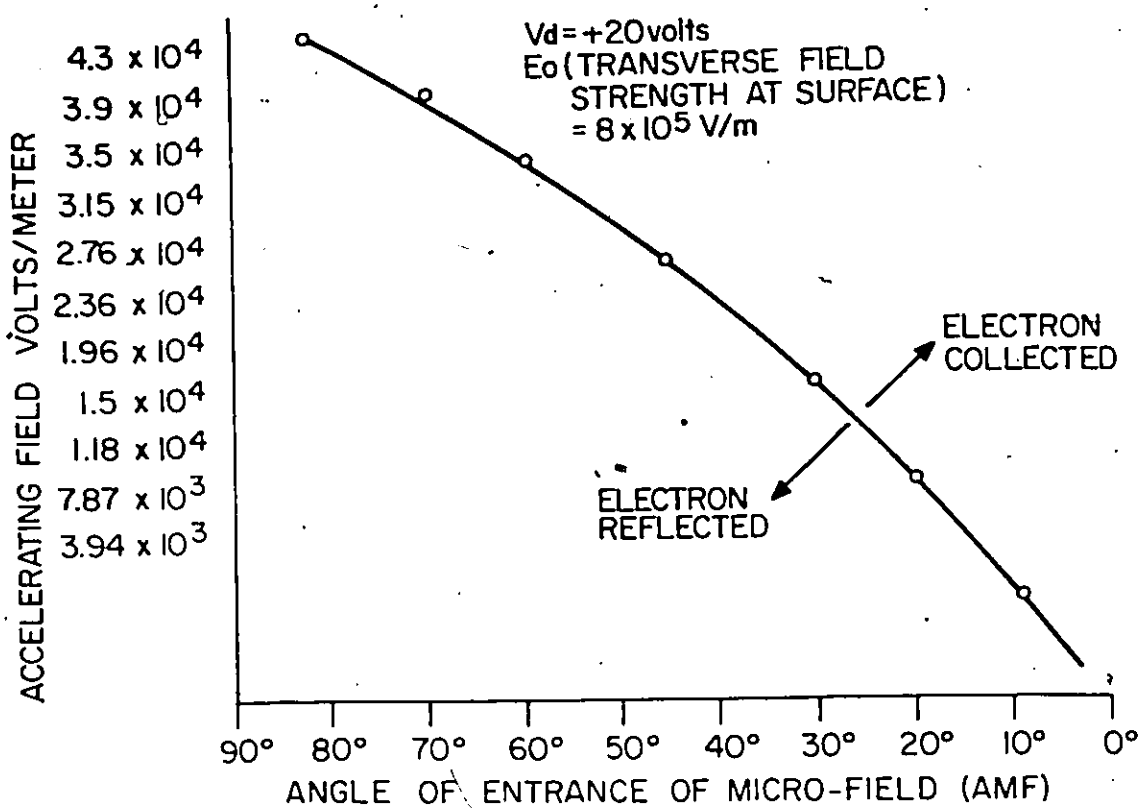
Vd = +20 volts
Eo (TRANSVERSE FIELD STRENGTH AT SURFACE) = 8 x 10^5 V/m
ACCELERATING FIELD VOLTS/METER
4.3 x 10^4
3.9 x 10^4
3.5 x 10^4
3.15 x 10^4
2.76 x 10^4
2.36 x 10^4
1.96 x 10^4
1.5 x 10^4
1.18 x 10^4
7.87 x 10^3
3.94 x 10^3
ELECTRON COLLECTED
ELECTRON REFLECTED
90° 80° 70° 60° 50° 40° 30° 20° 10° 0°
ANGLE OF ENTRANCE OF MICRO-FIELD (AMF)

Fig. 4.7

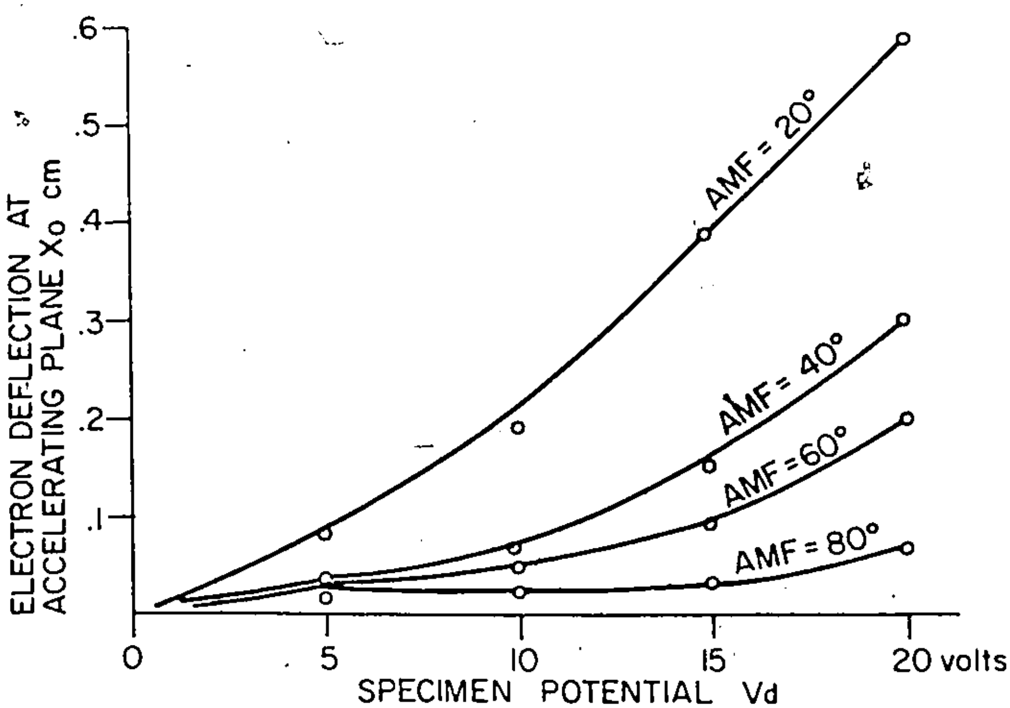
ELECTRON DEFLECTION AT ACCELERATING PLANE Xo cm
.6
.5
.4
.3
.2
.1
AMF = 20°
AMF = 40°
AMF = 60°
AMF = 80°
0 5 10 15 20 volts
SPECIMEN POTENTIAL Vd

Fig. 4.6

This graph shows the angle of entrance of micro-field plotted against accelerating field strength.

Ud = +20 volts
Eo (Transverse field strength at surface) = 8 x 10 volts/meter
d = 2.54×10^{-5} meters
ZA = 1.27×10^{-2} meters

Fig. 4.7

This graph shows the specimen potential plotted against electron deflection at the accelerating plane, angle of entrance of the micro-field as a parameter.

Fig. 4.8

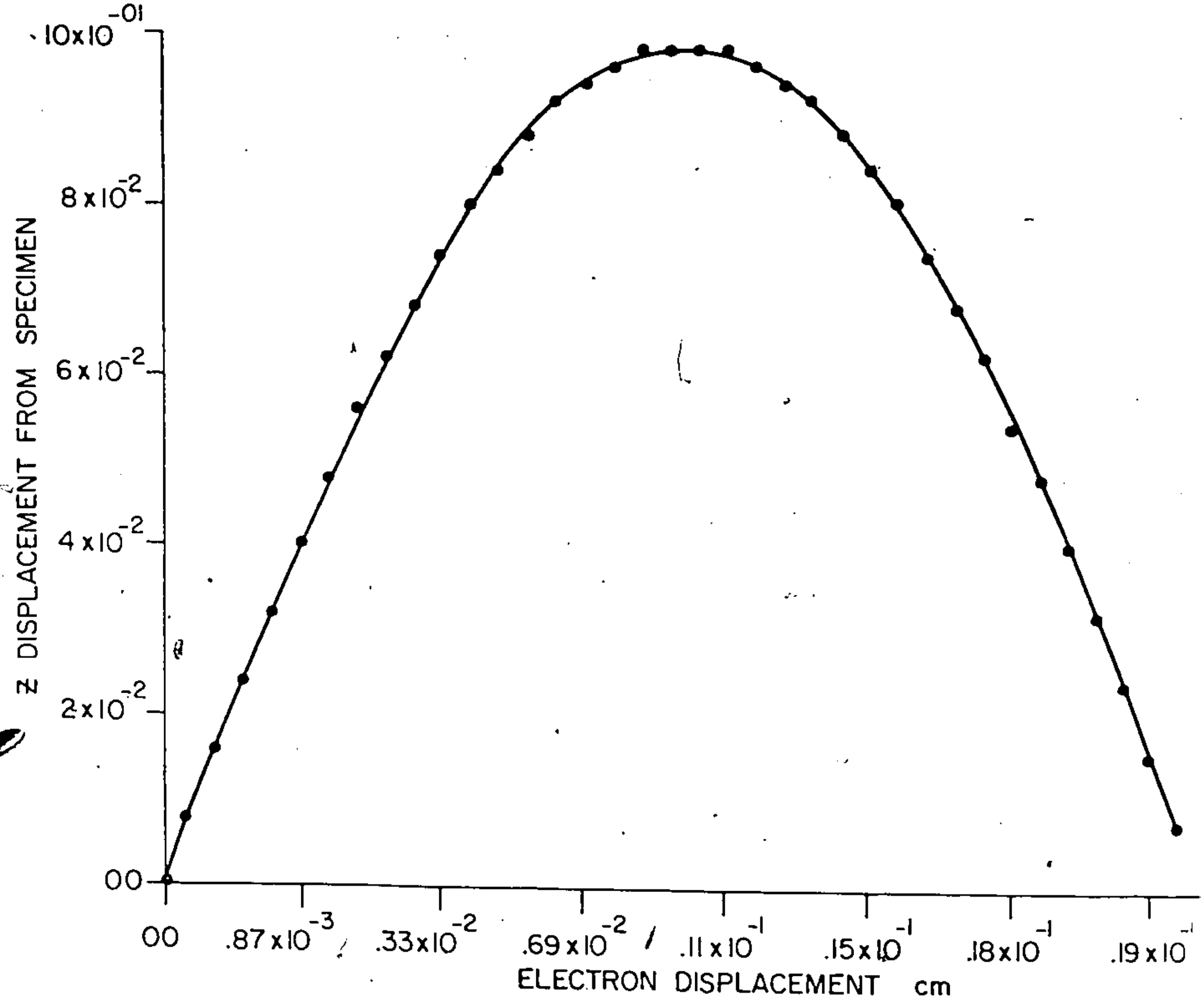

10x10^-01
8x10^-2
6x10^-2
4x10^-2
2x10^-2
00
Z DISPLACEMENT FROM SPECIMEN
00
.87x10^-3
.33x10^-2
.69x10^-2
.11x10^-1
.15x10^-1
.18x10^-1
.19x10^-1
ELECTRON DISPLACEMENT cm

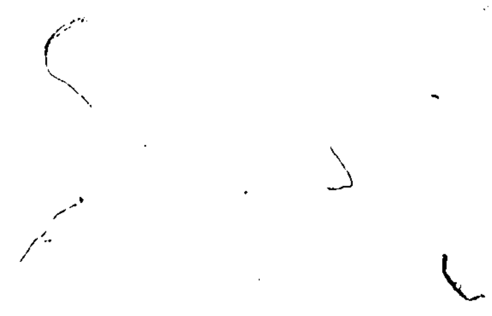

Fig. 4.8

This figure shows an example of an electron trajectory emitted into a retarding transverse field.

Ud = +20 volts
AMF = 70°
Emission Energy = 2 ev
Accelerating mesh potential = 3000 volts
d = 2.54×10^{-5} meters
ZA = 1.27×10^{-2} meters

Fig. 4.9

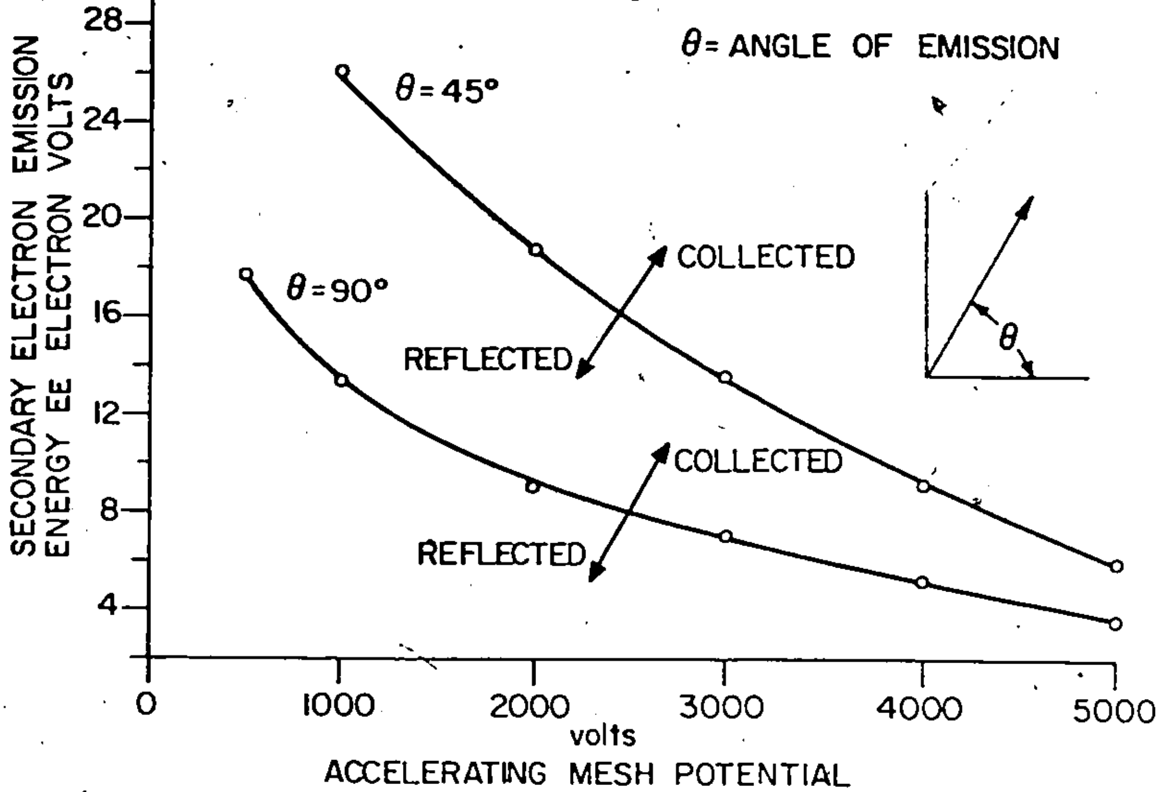

Fig. 4.10

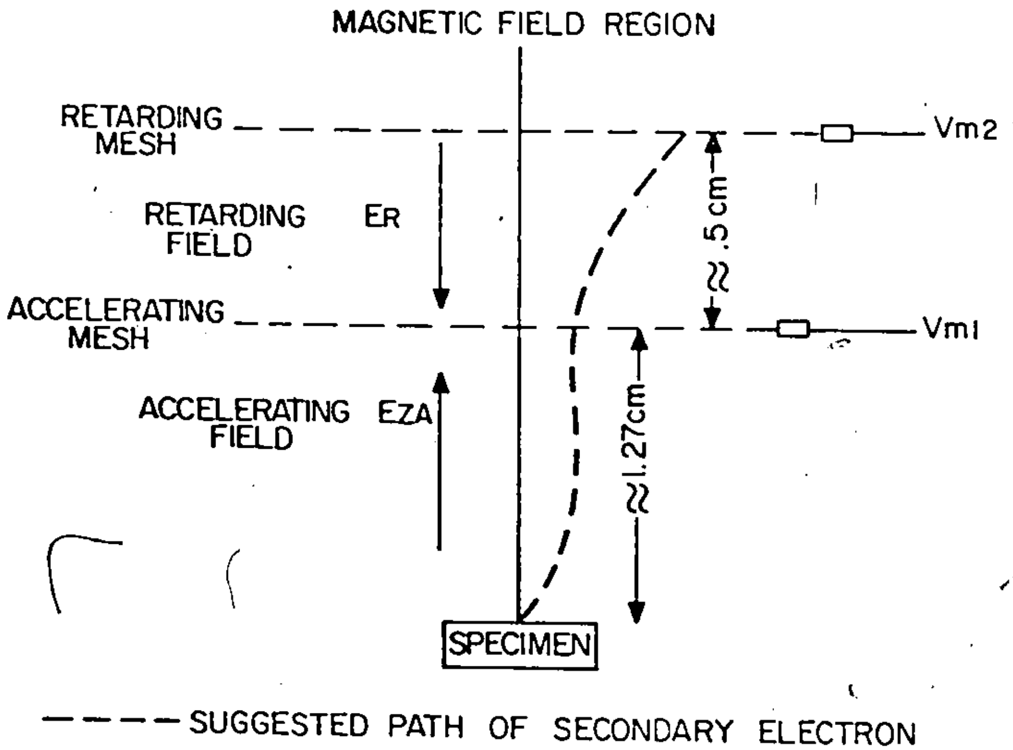

Fig. 4.9

This graph shows accelerating mesh potential versus secondary electron emission energy with the angle of electron emission θ as a parameter.

AMF = 90^o,
Vd = +20 volts
d = 2.54×10^{-5} meters
ZA = 1.27×10^{-2} meters.

Fig. 4.10

This figure shows the arrangement of accelerating and retarding field.

for this trajectory are tabulated in the figure. Before any conclusions are drawn from these data, the effect of varying the angle and energy of emission of the electron must be studied. This data is shown in Figure 4.9 where the boundary conditions between the collection and reflection of an electron are shown against emission energy and accelerating mesh potential for two values of the emission angle. The curves were derived for a normal angle of transverse field and a value for V_d of +20 volts. The curves show that under these worst case conditions, an electron with an emission energy of 2 eV will not be collected even at the highest value of accelerating mesh potential and a zero emission angle, θ.

The data presented so far shows that at a high value of accelerating field of $\sim 5 \times 10^4$ volts/meter (V_m = 6000 volts, Z_A = 1.27 cm in Figure 4.9) the effects of transverse fields can be reduced so that low energy electrons can be collected. However, the effects can never be eliminated entirely. The two most difficult conditions are, 1) strong transverse fields normal to the surface which will reflect electrons and 2) transverse fields at high angles which will produce the largest lateral electron deflection. In the case of a measurement performed on the type of structures shown schematically in Figure 4.3, a near normal field will exist near the centre of the pad but the highest field will exist at the edges. It seems reasonable, therefore, that measurements may be performed near the centre of a pad where the field, although normal, is the weakest. This has been confirmed by the experimental work (see Chapter 5 and 6).

If, as suggested above, the electrons are accelerated from the specimen surface by a potential of 6 KV on the accelerating mesh, it may be shown (see next section) that a magnetic field of approximately 10^{-2} webers/m^2 would be required to deflect these 6 KeV electrons through an angle of 90° and onto the aperture plane of the detector. It will be shown in Chapter 5 that the generation of a magnetic field of this magnitude would result in a high power dissipation and resultant heating problems.

A possible solution to this problem is to use a retarding field immediately after the accelerating field, to reduce the energy of the electrons so that they may be deflected with lower magnetic field strengths. This arrangement is shown schematically in Figure 4.10. Using a modification of the computer program cited earlier, an analysis of this situation was carried out to determine if the presence of the retarding field would limit the effectiveness of the accelerating field in controlling transverse fields at the specimen surface. It was found that the lateral electron deflection produced by the transverse fields, measured in the plane of the retarding mesh M_2, was very sensitive to accelerating field potential, V_{m1}, but very insensitive to retarding field potential V_{m2}. These results are shown in Figures 4.11 (a) and (b). Electrons emitted normal to the surface with energy of 2 eV into a parallel transverse field were studied. The curves show that if the potential on the retarding mesh, V_{m2}, is varied from zero to 5 KV with 5 KV on the accelerating mesh, a deflection of only .01 cm is produced, whereas, if the accelerating mesh potential, V_{m1}, is varied from zero to 5 KV with 200 volts on the retarding field mesh, a change in deflection of .24 cm is produced. The fact that the retarding field has little effect on the behaviour of the transverse field supports the argument that transverse field effects are limited to a region very close to the specimen surface.

It is interesting to note the effect of the transverse field on the shape of the electron density distribution at the accelerating plane. Assuming that the electron emission density distribution is Gaussian (3.1), the effect of transverse fields of varying angles is shown in Figure 4.12 (a), (b), and (c). Figure 4.12(a) shows that the distribution is distorted very little by a transverse field which is parallel to the surface; a large lateral shift is noted however. This is in agreement with the assumptions made by Saparin (3.1). However, in Figure 4.12 (b) considerable distortion is evident at a transverse field angle of 30^{o} and in the case of a normal transverse field, Figure 4.12 (c), no shift and only a slight distortion are evident.

Fig. 4.11 a)

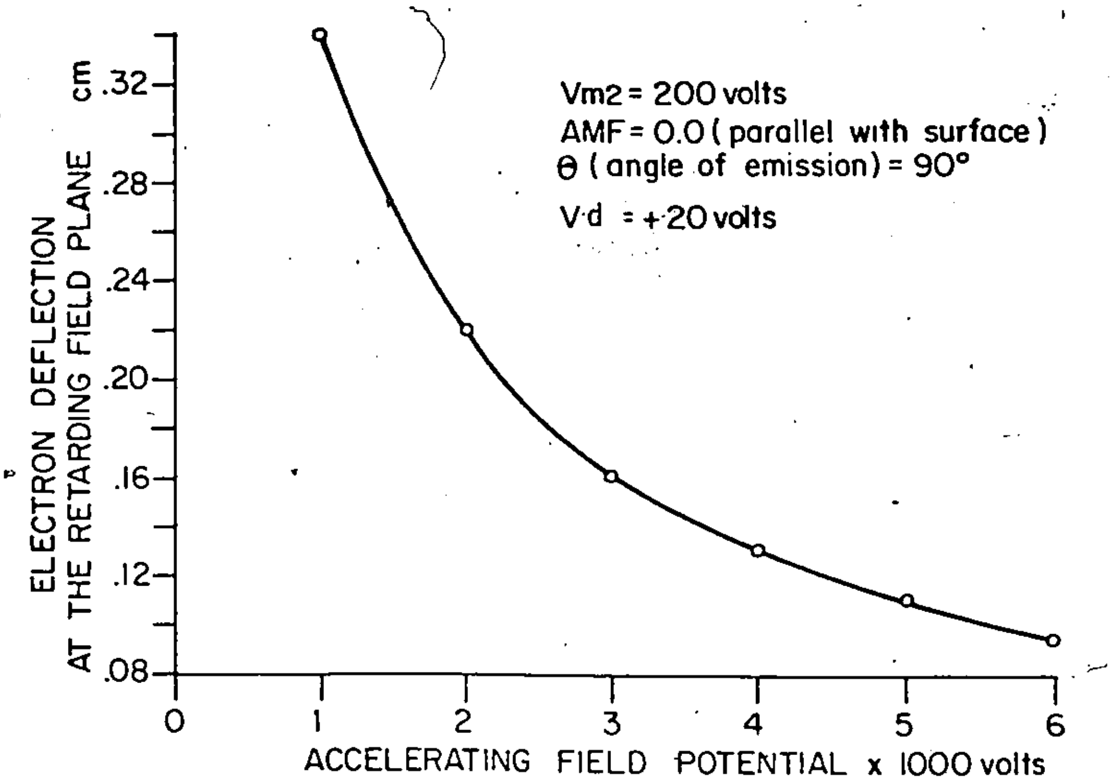

Fig. 4.11 b)

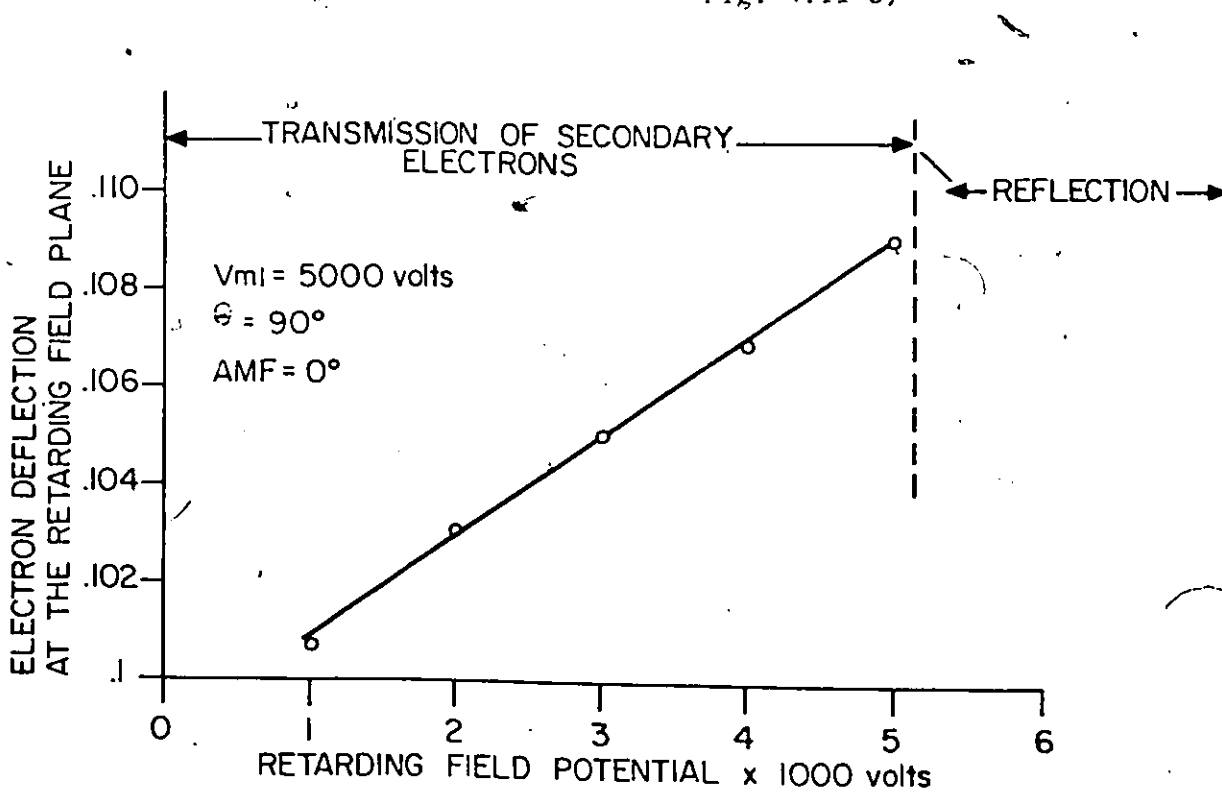

Fig. 4.11(a)

This graph shows accelerating field potential plotted against electron deflection at the retarding field plane.

Retarding mesh potential U_{m2} = 200 volts

AMF = 0.0^{o}
$\theta = 90^{o}$
Ud = +20 volts
d = 2.54×10^{-5} meters
ZA = 1.27×10^{-2} meters

Fig. 4.11(b)

Retarding field potential versus electron deflection at the retarding field plane is plotted in this graph.

Accelerating mesh potential U_{m1} = 5000 volts
$\theta = 90^{o}$
AMF = 0^{o}
Ud = +20 volts
d = 2.54×10^{-5} meters
ZA = 1.27×10^{-2} meters

Fig. 4.12 a)

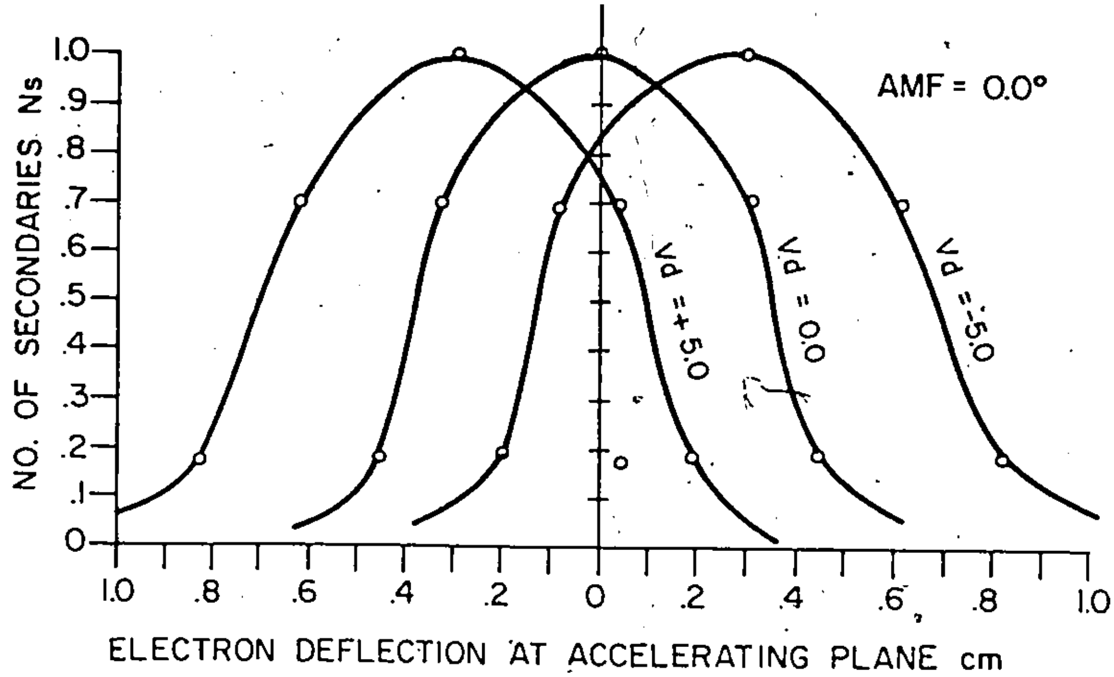

Fig. 4.12 b)

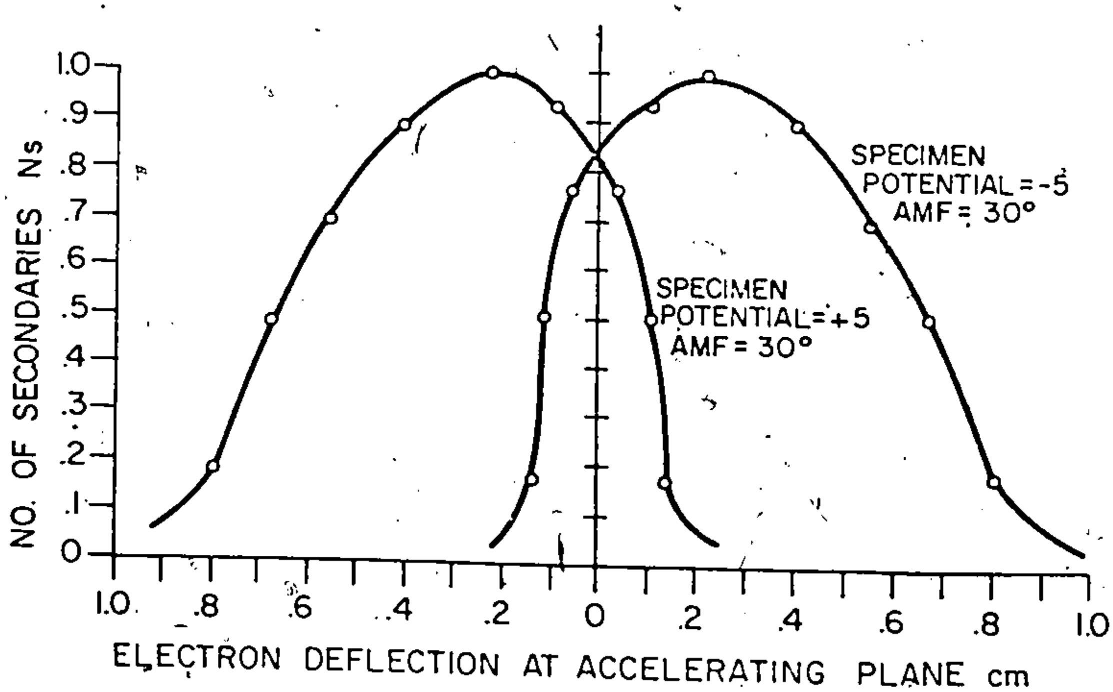

Fig. 4.12

This figure shows the electron deflection at the accelerating plane plotted against the number of secondaries arising at the plane under the following conditions.

a) Electron emission energy = 2.0 ev
AMF = 0.0
$d = 2.54 \times 10^{-5}$ meters
$\theta = 90^{\circ}$
$ZA = 1.27 \times 10^{-2}$ meters

b) electron emission energy = 2.0 ev
AMF = 30°
$d = 2.54 \times 10^{-5}$ meters
$\theta = 90^{\circ}$
$ZA = 1.27 \times 10^{-2}$ meters

Fig. 4.12 c)

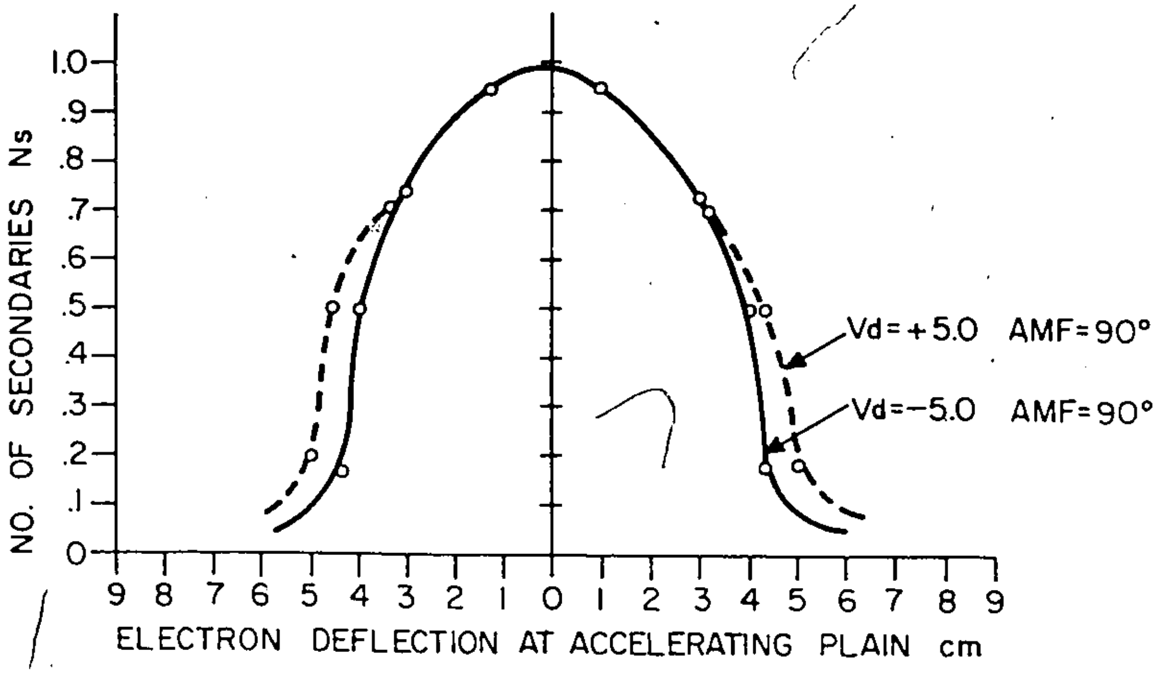

1.0
.9
.8
.7
.6
.5
.4
.3
.2
.1
0
NO. OF SECONDARIES Ns
9 8 7 6 5 4 3 2 1 0 1 2 3 4 5 6 7 8 9
ELECTRON DEFLECTION AT ACCELERATING PLAIN cm
Vd=+5.0 AMF=90°
Vd=−5.0 AMF=90°

Fig. 4.12

c) electron emission energy = 2.0 ev
   $\theta = 90^{o}$
   $d = 2.54 \times 10^{-5}$ meters
   $ZA = 1.27 \times 10^{-2}$ meters

Before any conclusions are drawn from this analysis we shall investigate the motion of electrons in a magnetic field.

4.3 The Motion of Electrons in a Magnetic Field

The secondary electrons, having been collected by the electrostatic field, now enter a magnetic field area, free of any electric fields. The magnetic field has the direction and magnitude such that these secondaries of energy E_{EM}, are deflected through an angle ϕ towards the aperture plane, see Figure 4.1.

The force on a charged particle in a magnetic field differs from the force exerted by an electric field in two important respects. There is a force only when the particle is in motion and the force is always at right angles to the direction of motion. A constant magnetic field can change the direction of motion of an electron but not its kinetic energy. With reference to Figure 4.1 and using the right hand rule, it may be determined that in order to deflect the electrons along the positive x axis, the magnetic field must be in the direction of the negative y axis.

The differential equations governing electron motion in a static magnetic field may be developed to the following form (4.1).

$$\frac{d^2x}{dt^2} = \frac{-e}{m}\left(Bz\frac{dy}{dt} - By\frac{dz}{dt}\right)$$

$$\frac{d^2y}{dt^2} = \frac{-e}{m}\left(Bx\frac{dy}{dt} - Bz\frac{dx}{dt}\right)$$

$$\frac{d^2z}{dt^2} = \frac{-e}{m}\left(By\frac{dx}{dt} - Bx\frac{dy}{dz}\right).$$

where all the terms have their usual meaning and e/m is the charge to mass ratio for the electron.

If $Bx = Bz = 0$ and if the aperture plane is positioned on the positive x axis, these equations become,

$$\frac{d^2x}{dt^2} = +\frac{eBy}{m}\frac{dz}{dt}$$

$$\frac{d^2y}{dt^2} = 0 \qquad \text{eqs. 4.1}$$

$$\frac{d^2z}{dt^2} = -\frac{e}{m}By\frac{dx}{dt}$$

Fig. 4.13

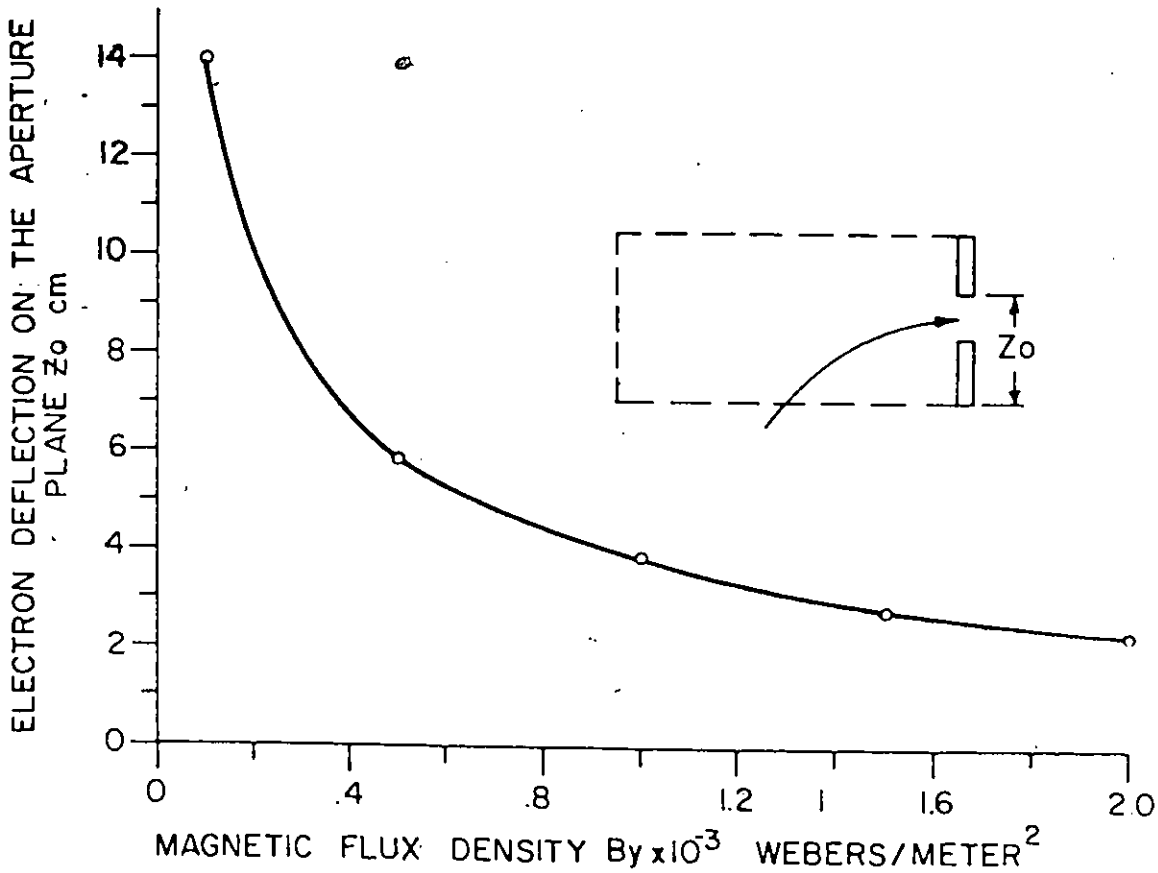

ELECTRON DEFLECTION ON THE APERTURE PLANE Zo cm
14
12
10
8
6
4
2
0
.4
.8
1.2
1.6
2.0
MAGNETIC FLUX DENSITY By x10^-3 WEBERS/METER^2
Zo

Fig. 4.13

This graph plots magnetic flux density versus electron deflection at the aperture plane.

Aperture plane 2 cm. from beam axis.
Energy of electrons entering magnetic field = 200 ev
β(angle of entrance into magnetic field) = 90°

These equations may be solved to yield the following expressions (see Appendix 2)

$$x = \frac{+e}{m} Vx\ By\ Sin \frac{e}{m} By\ t \frac{+e}{m} VzBy\ Cos \frac{e}{m} By\ t \frac{-mVz}{eBy}$$

$$y = Vyt \qquad \text{eqs. 4.2}$$

$$z = \frac{+m}{e} \frac{Vx}{By} Cos \frac{e}{m} By\ t \frac{-m}{e} \frac{Vz}{By} Sin \frac{e}{m} By\ t \frac{-mVx}{eBy}$$

The value of By may be determined from the equation (4.1),

$$\phi = \frac{e}{m} By \frac{a}{v} \qquad \text{eq. 4.3}$$

where ϕ is the deflection angle, By is the magnetic field, a is the length of the magnetic field region, V is the electron velocity and e/m is the charge to mass ratio for the electron as before.

If ϕ is chosen as 90^{o} and 'a' as 5 cm and if the electrons have an energy of 200 eV then the flux density is

$$By = 1.55 \times 10^{-3} \text{ webers/m}^2 = 15.5 \text{ gauss.}$$

The analogue simulator program was again used to study the electron trajectories in the magnetic field. If the electrons entering the magnetic field are assumed to be monoenergetic and enter the magnetic field at right angles to the retarding plane, then their point of incidence on the aperture plane is dependent on the magnetic flux density as shown in Figure 4.13. It was shown, that at higher values of By, ($\gtrsim 3 \times 10^{-3}$ webers/m^2) the electrons are deflected below the retarding plane (i.e. Z_o negative) at the aperture plane. At very high values of By ($\gtrsim 8 \times 10^{-3}$ webers/m^2) the electrons are made to spiral in the magnetic field.

If now, an appropriate value of flux density is chosen (By = 1.5×10^{-3} webers/m^2) and the entrance energy of the electron is allowed to vary, the variation of electron incidence position on the aperture plane with entrance energy is shown in Figure 4.14. This curve shows that the incidence position varies linearly with entrance energy over a range of 40 eV centred on 200 eV. This is equivalent to a ± 20 V specimen potential change with a retarding mesh potential of 200 volts. The position parameter, Z_o, is again measured from the retarding field plane as in Figure 4.13.

Fig. 4.14

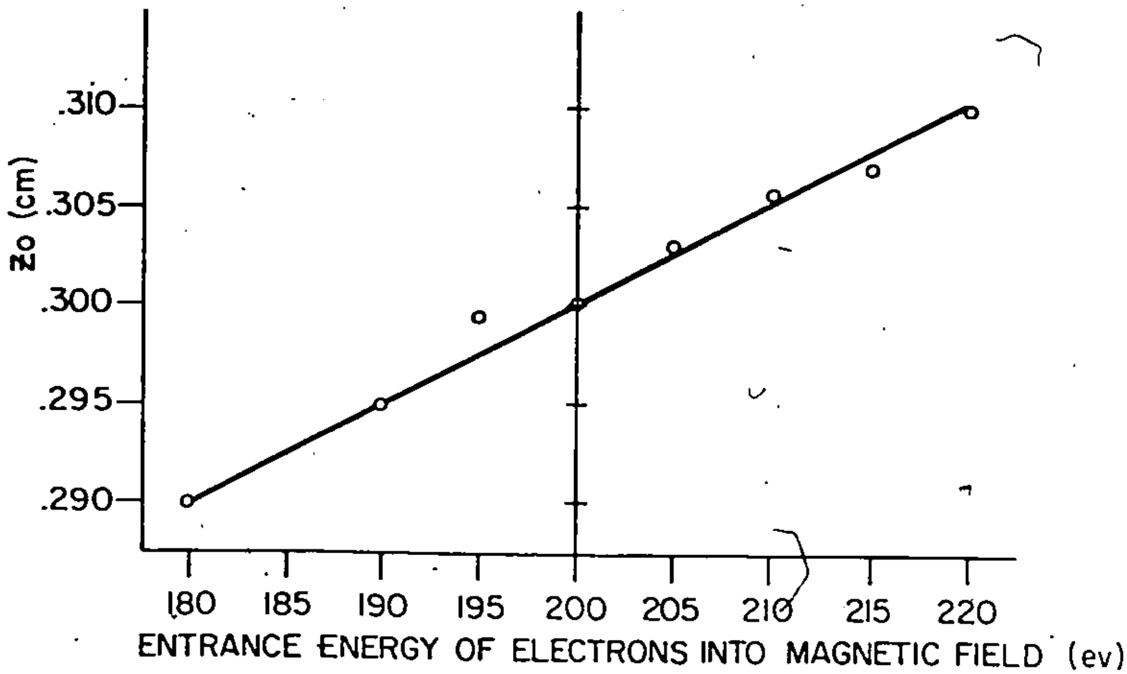

Fig. 4.15

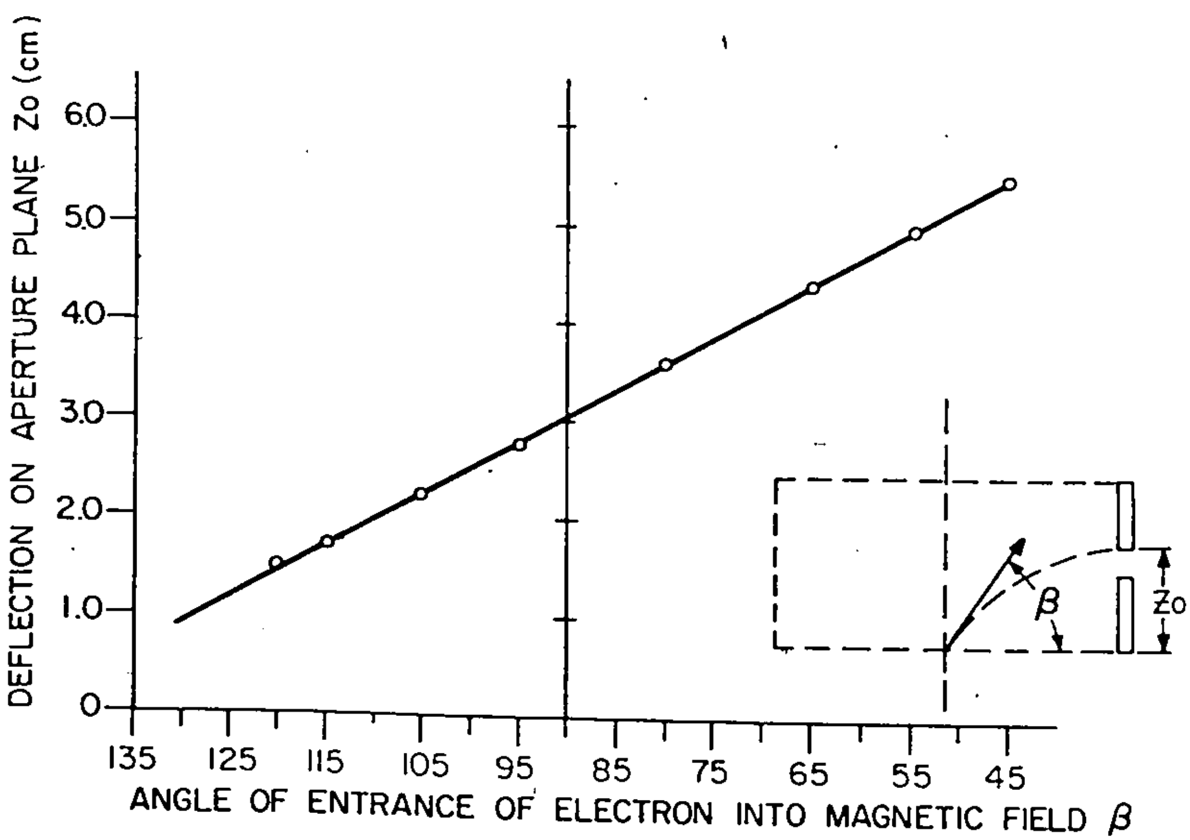

Fig. 4.14

This graph plots entrance energy of electrons into magnetic field versus electron deflection Z_o.

By = 15 gauss
$\beta = 90°$

Fig. 4.15

This graph shows angle of entrance of electron into magnetic field (β) versus deflection of electron on the aperture plane Z_o.

entrance energy of electrons = 200 ev
By = 15 gauss

As may be expected, the magnetic field causes a defocusing of the bundle of secondary electrons as these electrons are not, in reality, monoenergetic. The bundle size arriving on the aperture plane is further enlarged by the fact that electrons may enter the magnetic field at a variety of angles. The effect of this variation is shown in Figure 4.15. It is estimated that the combined effect of defocusing due to the presence of different electron energies and different angles of entrance into the magnetic field results in a bundle size at the aperture plane which is approximately 5 times larger than the bundle size at the entrance plane (retarding field mesh).

4.4 Conclusions

From the above analysis, an appreciation of the magnitude of the potentials and fields involved in the design of a voltage sensitive detector can be gained. In addition, some of the processes involved and the factors of importance are indicated. Because of the assumptions made, however, it was decided that an analysis of the total operation of the detector in an attempt to predict the sensitivity, linearity and range etc. would not be worthwhile. The determination of these parameters is to be carried out on an experimental basis in the next two chapters.

The above analysis does lead to the following general conclusions.

a) The contrast resulting from changes in specimen surface potential is composed of a field contrast component and a voltage contrast component. The field contrast component results from transverse fields which exist between elements on the surface at different potentials.

b) The transverse fields lead to a deflection of the emitted electrons or even the reflection of electrons back to the specimen surface under extreme conditions. Both of these effects hinder the observation of voltage contrast.

c) The effects of transverse fields can be reduced by the use of a normal accelerating field at the surface of the specimen. A field of the order of 5×10^4 volts/meter is required to adequately suppress the effects under the worst case conditions.

d) Even though transverse fields cannot be entirely eliminated, it may be possible to perform voltage measurements away from the edges of pads and metallization strips without the effects of transverse field interference.

e) The use of a retarding field after the accelerating field does not disturb the action of the accelerating field in the reduction of transverse field effects.

f) A magnetic field of ~ 2×10^{-3} webers/m^2 will produce the desired deflection of electrons of 200 eV energy. This means that a potential of the order of 200 volts should be used on the retarding mesh if the value of magnetic field is not to be increased.

CHAPTER FIVE

Experimental Testing of the New Detector

Introduction

In the last chapter,an analysis of the new detector was carried out and approximate values were determined for the important parameters. The analysis showed that the detector design proposed would, in fact, operate as anticipated. In this chapter the design of the first prototype detector is described along with the results obtained from it. The first section discusses the construction of the detector.

5.1 Detector Construction

The detector design used in the first experiments is shown schematically in Figure 5.1. It consists of three main sections, the specimen box, the wire mesh cage and electromagnetic coil assembly and an Everhart-Thornley type electron detector. The collection field is generated between the lower surface of the mesh cage (the accelerating plane) and the specimen and its surrounding area. The surrounding area is of complex geometry and in order to maintain a symmetrical and controllable field around the specimen, the specimen box arrangement shown was used. This box is made of aluminum and has a hole in the centre which allows the specimen to be moved in the x and y directions within the hole. Photographs of the actual detector are shown in Figure 5.2.

The specimen box is suspended from the base of the mesh cage so that the base of the cage, which acts as the accelerating plane in the present experiments, is close and parallel to the specimen surface. The analysis indicated that the secondary electron bundle could be up to 2cm in width and a cage width of 4cm was chosen on this basis. The length of the cage is 6cm. and its height is 2.5cm These dimenisons were dictated by space limitations. The top and bottom surfaces of the cage are made of Ni mesh. This mesh is made up of .002" wires with a .018" spacing and has a transmission factor of 82%. These meshes were used to provide an electric equipotential surface with a high electron transmission factor.

.../2

FIG. 5.1

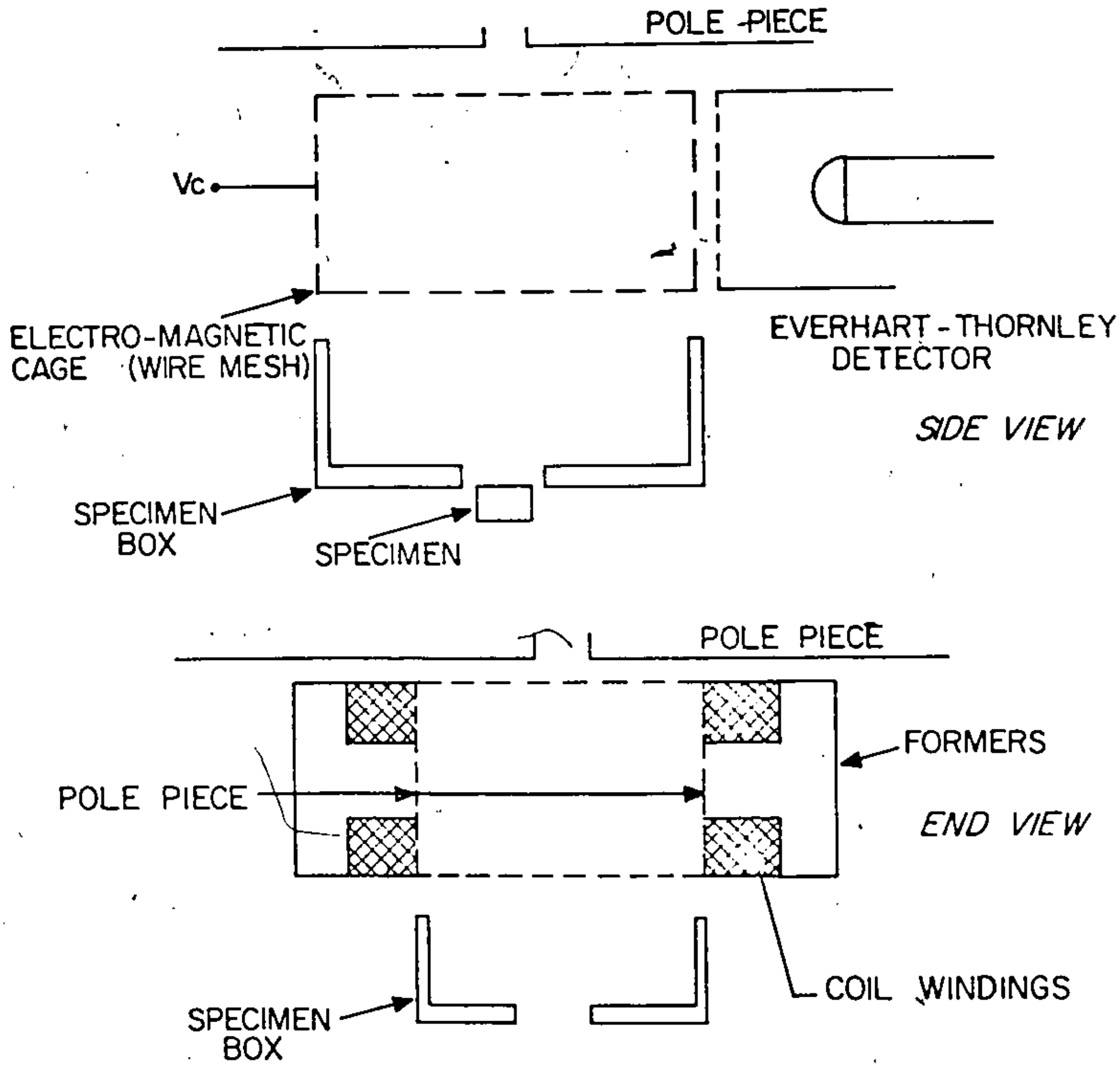
POLE -PIECE
Vc
ELECTRO-MAGNETIC CAGE (WIRE MESH)
EVERHART - THORNLEY DETECTOR
SIDE VIEW
SPECIMEN BOX
SPECIMEN
POLE PIECE
FORMERS
POLE PIECE
END VIEW
COIL WINDINGS
SPECIMEN BOX

Fig. 5.1

This figure shows the detector used in the first experiments.

FIG. 5.2

(a)

(b)

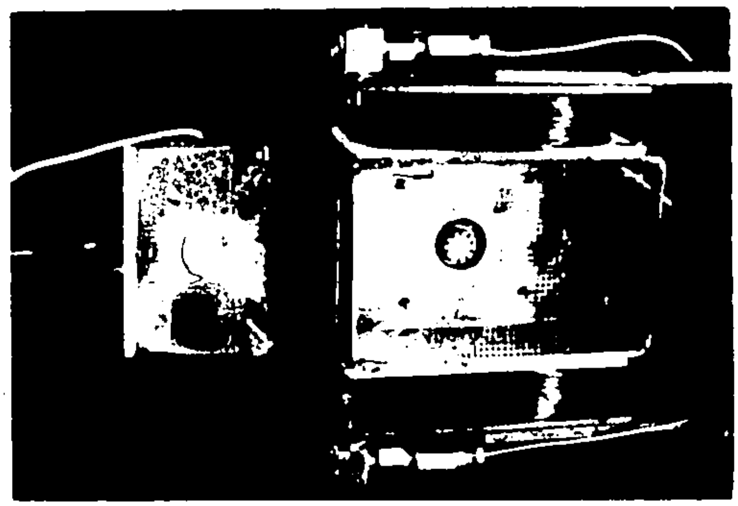

(c)

Fig. 5.2(a)

These photographs show an expanded view of the proto-type detector showing the Everhart-Thornley electron detector on the left, the specimen box and specimen in the bottom and the wire mesh cage and electromagnetic coil assembly in the upper right.

Fig. 5.2(b)

This figure shows the top view of the detector system with the electron detector assembly on the right and the wire mesh cage and electromagnetic coil assembly to the left. The specimen is viewed through the cage.

Fig. 5.2(c)

This shows the front view of the cage assembly showing the mounting of the aperture.

The coils used to generate the magnetic field are mounted on the sides of the cage, see Figures 5.1 and 5.2. The dimensions of the magnetic pole pieces and the magnetic air gap being determined by the dimensions of the cage. A low reluctance path is used to complete the magnetic circuit, see Figure 5.2. The dimensions of the magnet coils and the circuit are shown in Figure 5.3. The number of ampere-turns needed to generate the required flux density in the gap was determined using the data provided by Dawes (5.1) and the formula,

$$By.A = \frac{0.4\ N \cdot I}{\ell/\mu A} \quad \text{eq. 5.1}$$

where By is the flux density in the gap in gauss, A is the cross-sectional area of the pole pieces, ℓ is the path length in the air gap, μ is the permeability of free space and NI is the number of ampere-turns.

The analysis carried out in the previous chapter showed that a flux density of the order of 15 gauss was needed. Accepting this value, and using the values of ℓ and A for the coils used, a value for NI of 128 Ampere-turns is calculated from equation 5.1.

The coils consist of 540 turns of #30 magnet wire wound on cold-rolled steel pole pieces. A current of .24 A is needed to provide the flux density specified and this results in a power dissipation of 150 mW. This value was considered sufficiently low for operation in a vacuum environment.

The third part of the system is an Everhart-Thornley type of electron detector with an aperture mounted in front. The aperture plate forms one end of the cage and it is supported by two cross bars. The Everhart-Thornley detector is supported by its light guide. In all the experiments reported, the Faraday cage of the Everhart-Thornley detector was held at the same potential as the mesh cage. The aperture and detector can be seen in Figure 5.2.

5.2 Experimental Testing of the Detector--The Magnetic Characteristic

The first series of experiments carried out was of an exploratory nature, designed to determine the general operating characteristics of the system. In these

FIG. 5.3

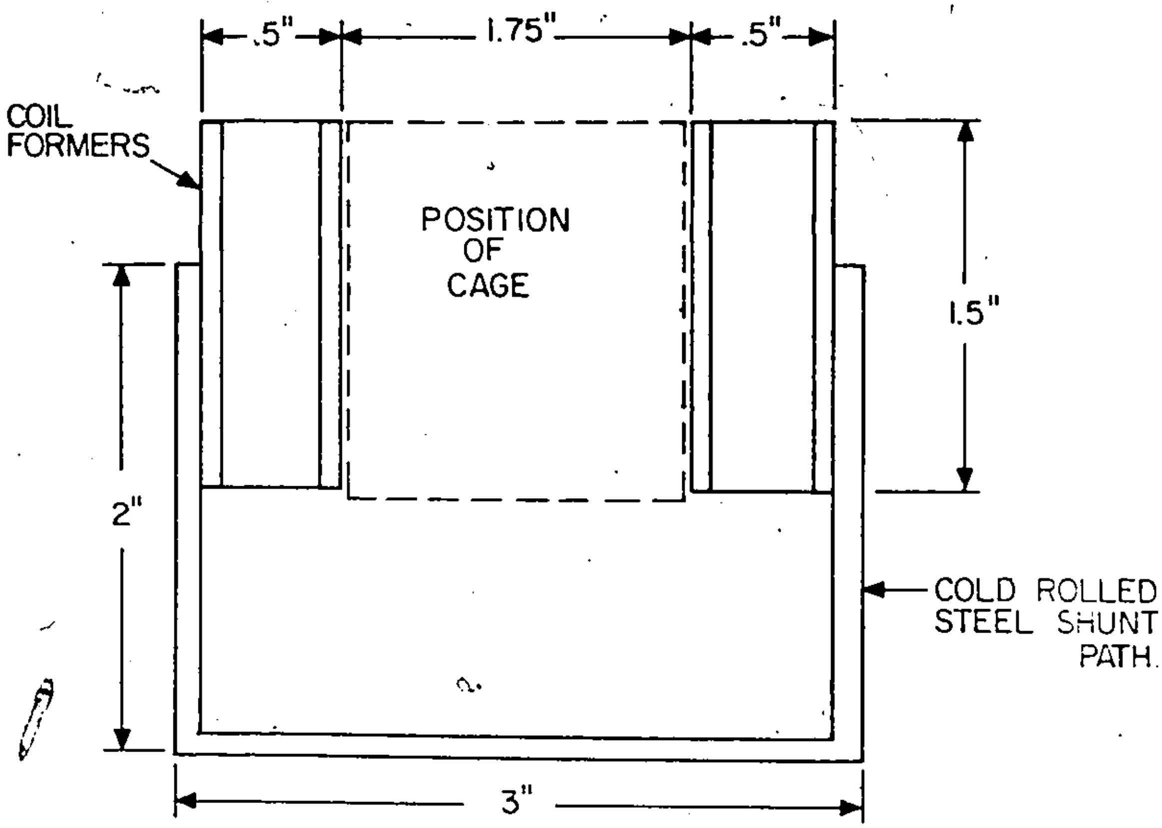

TOP VIEW

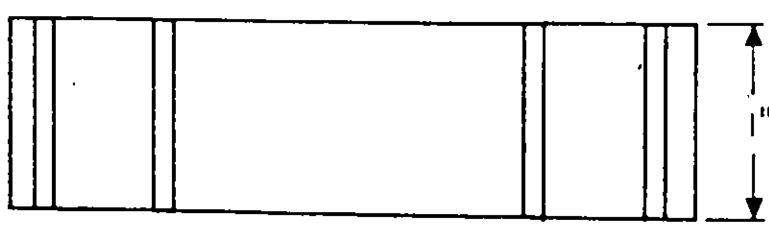

END VIEW

Fig. 5.3

The dimensions of coil formers and magnetic shunt used in the first detector test model are shown here.

experiments, the cage potential and the specimen and specimen box potentials were held constant and the output signal was observed as the magnetic field was varied from zero to a value well in excess of that required. No aperture was used, with the end of the box covered by a piece of wire mesh to maintain the electrostatic field-free region.

It was expected that the output signal versus magnetic field curve would show a single broad peak as the secondary electrons from the specimen surface were deflected towards the detector. In addition, a shift in the apparent position of the specimen, as observed on the viewing CRT, was anticipated as the primary electron beam would be deflected away from the detector by the magnetic field.

The shift in the specimen position was observed but the output signal showed five distinct peaks as the magnetic field was varied rather than the single peak expected. The experimental arrangement and conditions are shown in Figure 5.4, together with the output signal versus magnetic field strength characteristic obtained. Because the primary electron beam is moved across the specimen surface with changing magnetic field, a scanned line rather than a single spot was used in order to integrate the effects of changing topography which would otherwise confuse the results obtained.

It was suggested that the first peak, peak 1 of Figure 5.4, was due to secondary electrons generated at the lower mesh of the cage by backscattered electrons from the specimen surface. These electrons would have a lower energy than those emitted from the specimen surface and consequently be detected at a lower value of magnetic field. In order to verify this, a piece of aluminum foil was used to cover the lower mesh of the cage. A hole allowed the primary beam to pass through to the specimen and the secondary electrons to re-enter the cage. The wire mesh was also removed from the area of the hole to minimize the number of secondary electrons generated. The characteristic curve was again plotted and it was found that peak 1had been severly reduced where the remaining peaks were unaffected. It is apparent from this test that peak 1 is due to low energy secondary electrons generated at the lower surface of the cage.

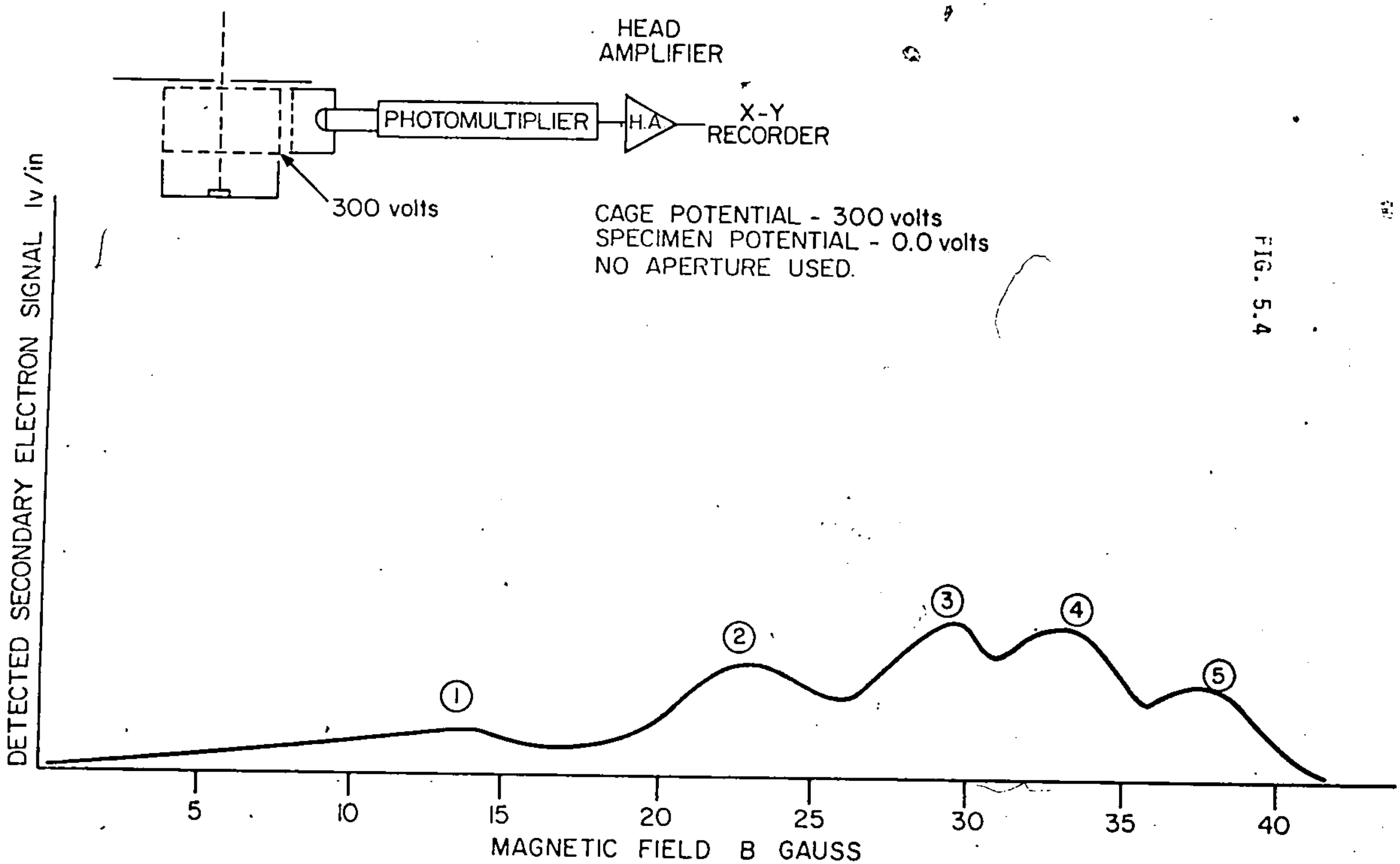
HEAD
AMPLIFIER
PHOTOMULTIPLIER
H.A.
X-Y
RECORDER
300 volts
CAGE POTENTIAL - 300 volts
SPECIMEN POTENTIAL - 0.0 volts
NO APERTURE USED.
DETECTED SECONDARY ELECTRON SIGNAL lv/in
1
2
3
4
5
5
10
15
20
25
30
35
40
MAGNETIC FIELD B GAUSS

FIG. 5.4

Fig. 5.4

This graph shows the magnetic field flux density versus detected secondary electron signal.

The peaks numbered 2 through 5 in Figure 5.4 were thought to be due to electrons arriving at the detector via unwanted paths. In order to determine these paths and eliminate the unwanted peaks, the Everhart-Thornley detector was replaced by a phosphor screen. A viewing port was installed in the specimen chamber so that the electron patterns produced on this screen could be observed and photographed as the magnetic field was varied. The arrangement used is shown in Figure 5.5(a). The secondary electron bundle observed on the phosphor screen and the corresponding scanning electron microscope images observed on the viewing CRT were photographed for a series of values of the magnetic field. These results are shown in Figure 5.6(a) through (f) for magnetic field strengths from zero to 30 gauss, covering the range of peaks 1, 2 and 3 of Figure 5.4.

It should be noted at this point, that the SEM images shown in Figure 5.6 were taken at a magnification such that the primary electron beam scanned the inside of the lower surface of the cage. This technique proved useful as it helped to determine the sources of the various signals involved. Under normal operation of the detector, the beam would not scan these areas.

Photographs A1 and A2 of Figure 5.6 were obtained at zero magnetic field. Photograph A2 shows that the source of signal observed in both the upper mesh (the large squares) and the lower surface of the cage as these appear bright. With no magnetic field present, secondary and backscattered electrons from these areas can be detected. No signal is observed from the specimen. As expected with zero magnetic field, no defined bright spot is observed on the phosphor screen. A rectangular area of light is observed however, the edges of which are defined by the edges of the end of the cage facing the screen.

As the magnetic field is increased from zero, a number of things occur. First of all, a steadily increasing signal is observed from the specimen in photographs A2, B2 and C2. Secondly, the signal observed from the inside lower surface of the cage reaches a peak at approximately 14 gauss (photograph B2) while the signal from the top mesh of the cage appears to remain substantially constant over this range. A well defined bright-region appears on the phosphor screen at low fields and

FIG. 5.5

(a)

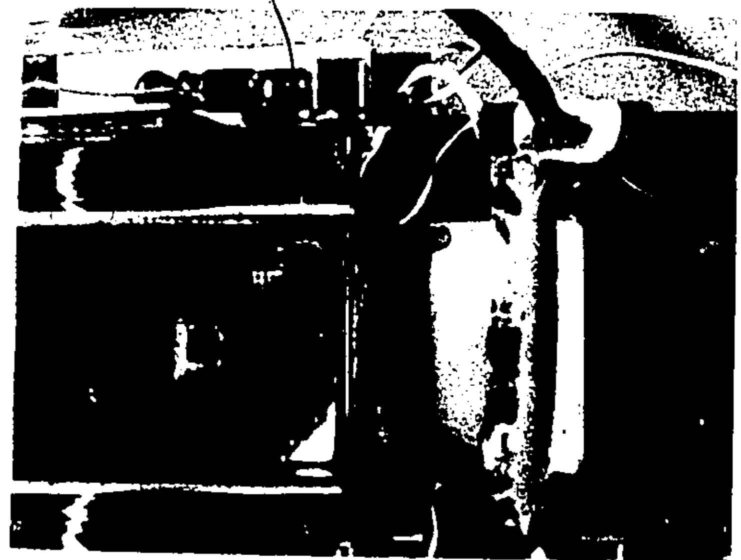

(b)

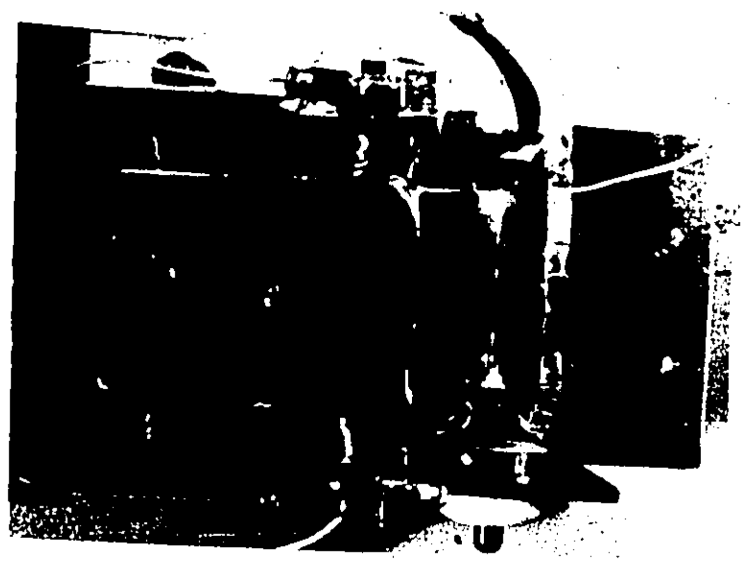

Fig. 5.5(a)

The phosphorous screen is shown here mounted facing the aperture plane of the cage assembly.

Fig. 5.5(b)

A piece of aluminum foil was placed over the top mesh of the cage to eliminate peak 2 of the magnetic characteristic.

FIG. 5.6

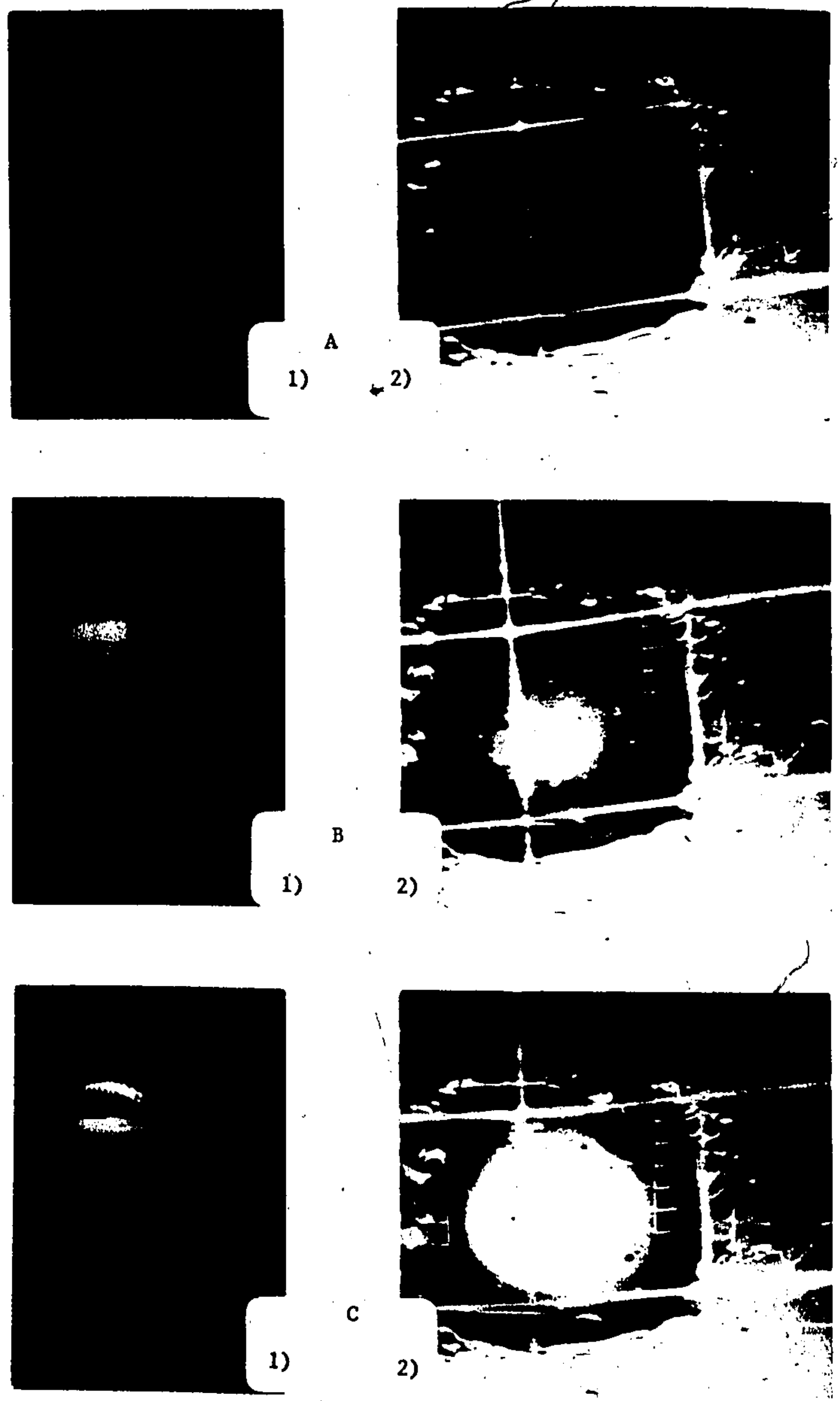

Fig. 5.6

This figure shows the results obtained using the phosphorous screen to observe the secondary electron bundle, 1) electrons arriving at the phosphorous screen, 2) micrograph of cage and specimen.

a) B = 0

b) B = 14 gauss

c) B = 20 gauss

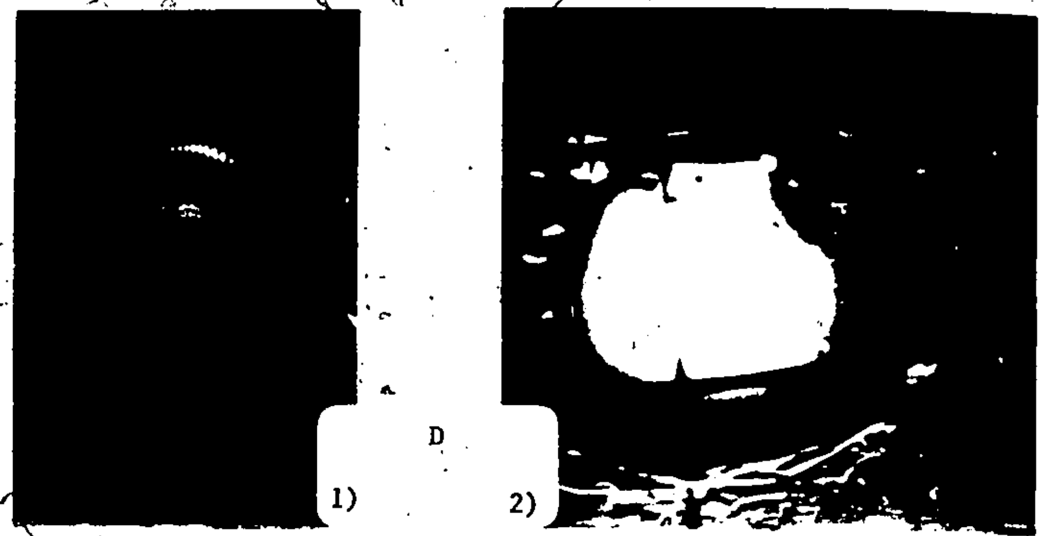
D
1)
2)

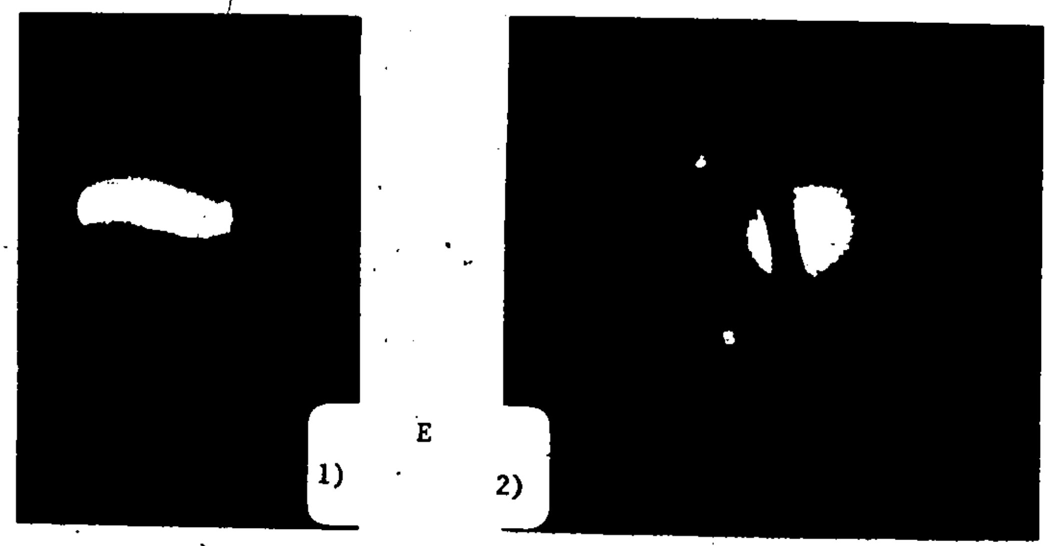
E
1)
2)

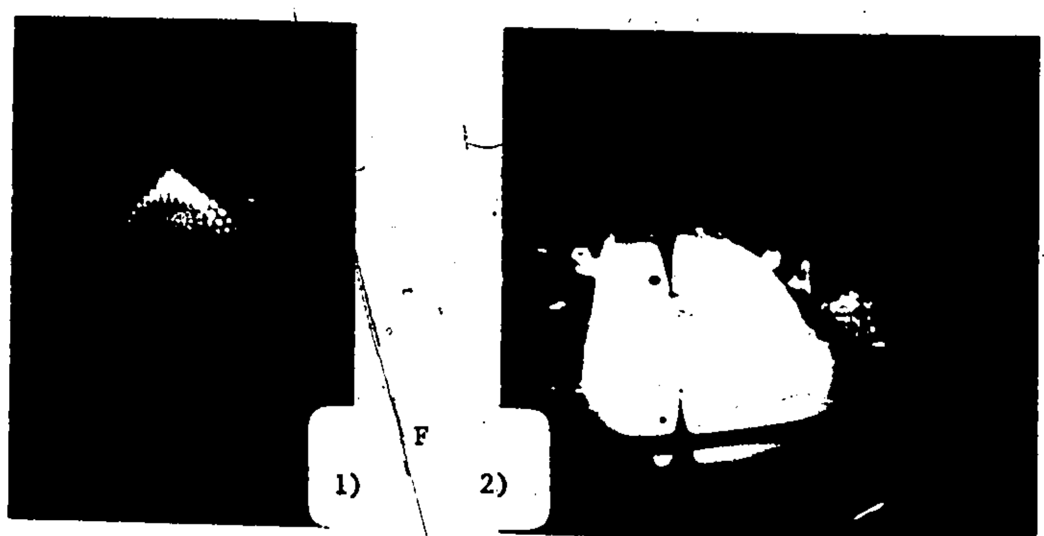
F
1)
2)

d) B = 23 gauss

e) B = 26.5 gauss

f) B = 29.5 gauss

rapidly moves down the screen as the field is increased. Its brightness position is shown in photograph B1 and it corresponds closely to the field value at which maximum signal is observed from the inside of the bottom of the cage, photograph B2: Referring now to Figure 5.4, it can be seen that the position of peak 1 of the magnetic characteristics, the peak in signal from the inside of the bottom surface of the cage and the brightest position of the spot on the phosphor screen are all coincident. They all occur at a value of magnetic field equal to 14 gauss. It is apparent that peak I of the magnetic characteristics is caused by secondary electrons generated on the inside of the base of the cage as proposed above. This is shown schematically in Figure 5.7A.

As the magnetic field is increased beyond 14 gauss, the first defined bright area on the phosphor screen disappears and a second one begins to appear at the top of the screen. Photograph C1 shows this second area appearing. Both this bright area and the signal from the specimen grow more intense as the magnetic field is increased and are then reduced in intensity again to a signal trough at approximately 26 gauss. The signal trough is shown in photographs E1 and E2. If the magnetic field is increased further than the signal from the specimen increases again and reaches another peak and an intense, well defined inverted "U" appears on the phosphor screen.

Both the signal from the specimen and the intensity of the inverted "U" on the phosphor screen reach a maximum intensity at a magnetic field strength close to 30 gauss. The intensities of the signals from the inside of the bottom surface of the cage and the top mesh of the cage are now undetectable.

If the values of the magnetic field shown in Figure 5.6 and those of Figure 5.4 are compared, it can be seen that peak 2 corresponds to the appearance of the second bright area on the phosphor screen and the trough between peaks 2 and 3 corresponds to photographs E1 and E2, where both the light output of the phosphor screen and the signal observed from the specimen show a dip in intensity. Peak 3 then corresponds to the appearance of the intense inverted "U" on the phosphor screen and the large signal observed from the specimen.

FIG. 5.7

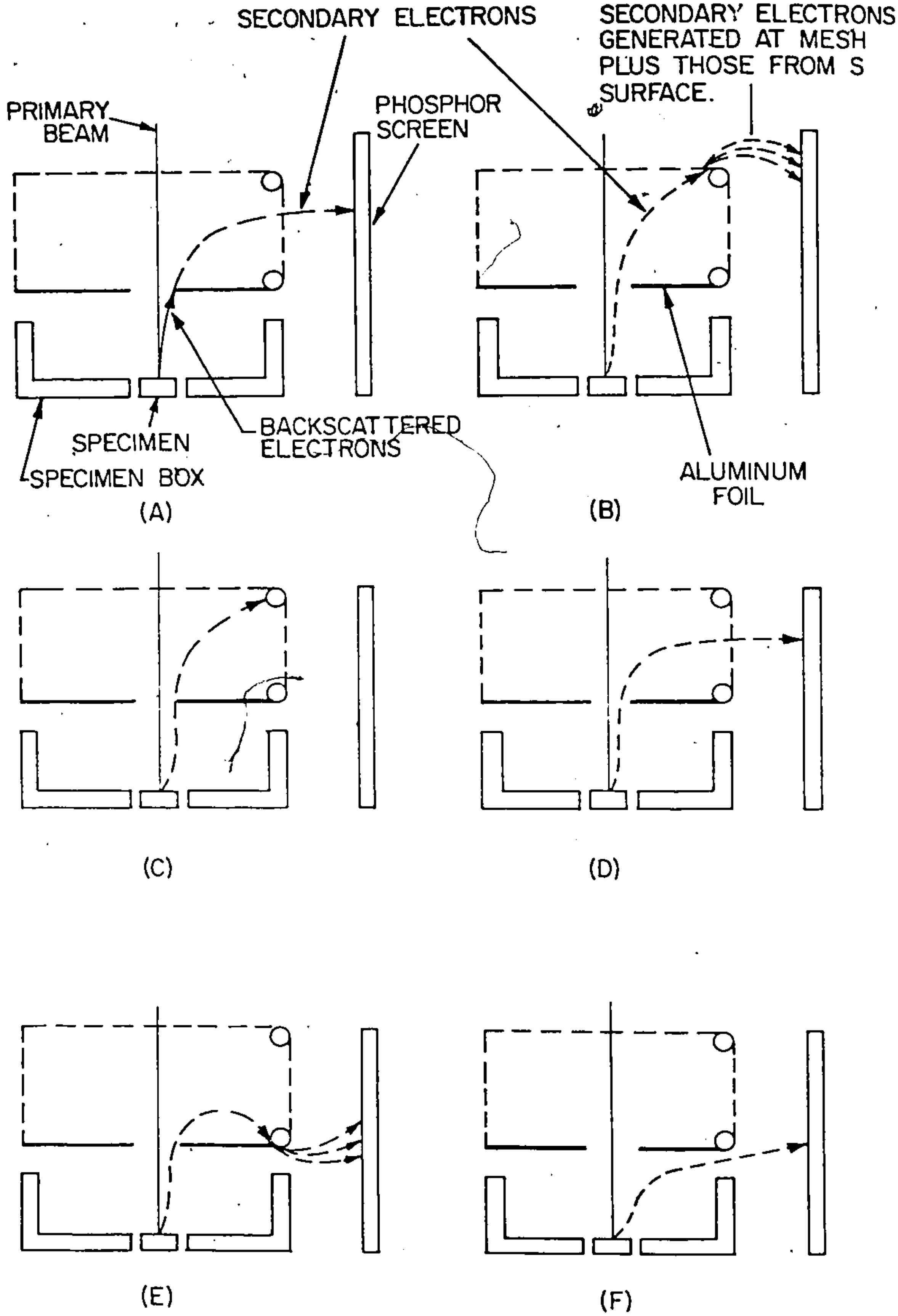
SECONDARY ELECTRONS
SECONDARY ELECTRONS GENERATED AT MESH PLUS THOSE FROM S SURFACE.
PRIMARY BEAM
PHOSPHOR SCREEN
SPECIMEN
SPECIMEN BOX
BACKSCATTERED ELECTRONS
ALUMINUM FOIL
(A)
(B)
(C)
(D)
(E)
(F)

Fig. 5.7

This series of diagrams follow the text in explaining the possible reasons for peaks 1 through 5 of the magnetic characteristic given in Figure 5.4.

a) Peak 1 results from secondaries produced on the lower mesh.

b) Peak 2 results from secondaries produced on the top mesh near the aperture plane.

c) The trough between peaks 2 and 3 results from the secondary electron bundle sweeping the top support bar.

d) Secondary electron bundle arriving at the aperture plane, peak 3.

e) Peak 4 results from secondary electrons produced at the lower mesh and aluminum foil.

f) Peak 5 is caused by electrons deflected directly towards the phosphorous screen (electron detector system).

It is proposed that peaks 2, 3 and 4 are caused by the secondary electron bundle of interest sweeping, first of all across the top mesh of the cage, then down the end mesh opposite the phosphor screen and finally onto the bottom of the cage as the magnetic field is increased. Referring now to Figure 5.7. Peak 2 of Figure 5.4 corresponds to Figure 5.7B where the secondary electron bundle is arriving at the top mesh of the cage just in front of the cross bar used to support the end of the cage. A further increase in the magnetic field sweeps the secondary electron bundle onto the cross bar and produces a fall in the signal observed (Figure 5.7C and photographs E1 and E2). As the field is further increased, the bundle of electrons reaches the screen directly as in Figure 5.7D and peak 3 is produced corresponding to photographs F1 and F2 of Figure 5.6. Another decrease in signal is caused by the lower cross bar followed by peak 4 where the secondary electron bundle strikes the inside of the bottom surface of the cage as shown in Figure 5.7E. The final peak, peak 5 is produced by electrons, deflected by the fringing magnetic field below the bottom plane of the cage, following paths directly to the phosphor screen as shown schematically in Figure 5.7F.

This explanation is supported by the fact that when aluminum foil was placed over the entire top and bottom surfaces of the cage, see Figure 5.5 (b), peaks 2 and 4 disappeared. Also, preventing electrons travelling directly from the specimen to the phosphor screen, again by using aluminum foil, eliminated peak 5.

The inverted "U" shape of the electron bundle arriving on the aperture plane (phosphor screen), shown in Figure 5.6F was explained by the presence of a non-uniform magnetic field within the cage. This field was measured using a small Hall probe and the values determined were used, together with the computer program, to predict the shape of the electron bundle arriving at the aperture plane under these conditions. The inverted "U" shape predicted by the computer analysis is in agreement with the results obtained. A typical result is shown in Figure 5.8.

FIG. 5.8

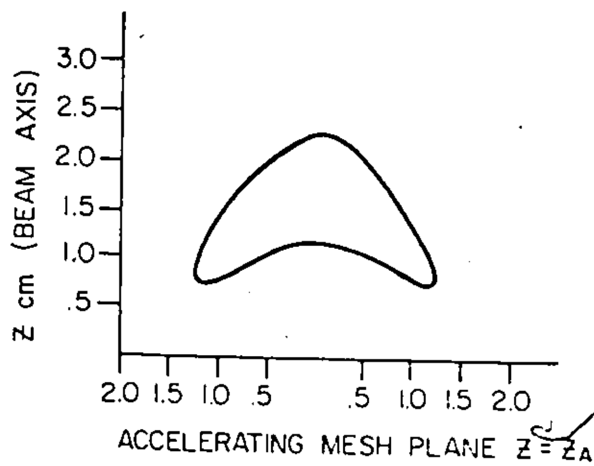

VIEW LOOKING AT APERTURE PLANE

Fig. 5.8

This figure shows the computer results showing the inverted "U" shape of the secondary electron bundle arriving at the aperture plane.

The Hall probe also showed that a relatively strong fringing magnetic field was present between the bottom surface of the cage and the specimen. The presence of such a field in the neighborhood of the specimen surface would be very undesirable as it would introduce a third force vector on the electrons emitted into the combined effects of the accelerating and transverse fields. Such a fringing field would have an unpredictable effect on the detector characteristics.

Before any further measurements were made, this field was reduced by replacing the mesh and forming the base of the cage by a piece of cold-rolled steel to provide a low reluctance path for the fringing field. This reduced the flux density at the specimen surface by about an order of magnitude. This new base contained an aperture for the primary beam and for the emitted secondary electrons. Figure 5.9 shows the steel base fitted to the cage.

When the detector was again used in the microscope a shadowing effect was observed. Only secondary electrons emitted from the rear part of the specimen, away from the aperture plane were detected and, as the inside of the base of the cage was scanned, secondary electrons generated on the rear inside edge of the hole in the cage base were also observed. This is shown in Figure 5.10. These effects are explained with the aid of Figure 5.11(a).

The primary electron beam is deflected away from the aperture plane as it passes through the magnetic field. The beam thus passes through the aperture in the base of the cage at a tilt with respect to the normal to the base of the cage. This explains why the inside back edge of the aperture is scanned and a singal obtained from it. As a horizontal velocity component is impressed on the primary beam, the beam scans an area on the specimen which is not directly below the aperture, see Figure 5.11(a). As only the rear part of the specimen is scanned, this explains why a signal is not obtained from the whole area of the specimen in Figure 5.10.

To compensate for this effect, the entire detector assembly is tilted as shown schematically in Figure 5.11(b). In this way, the primary beam passes through the aperture normal to the base of the cage and the area scanned on the specimen is now directly below the aperture in the base of the cage. By tilting the

FIG. 5.9

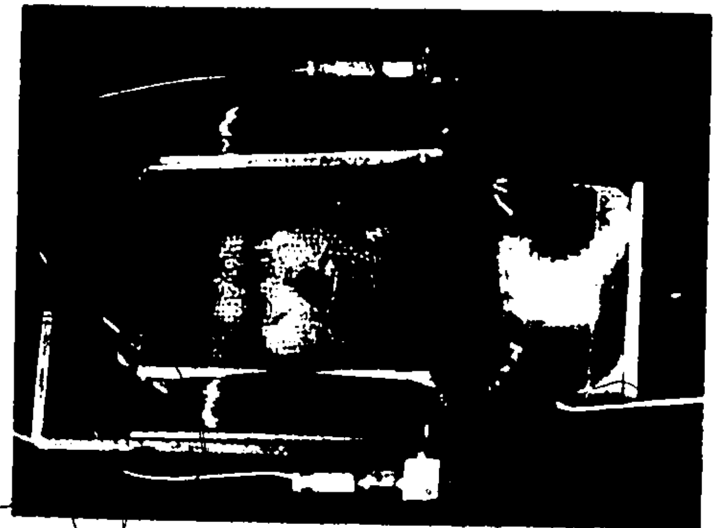

FIG. 5.10

Fig. 5.9

The magnetic shield is shown here mounted to the bottom of the wire mesh cage.

Fig. 5.10

Because of the primary beam deflection in the magnetic field the rear inside edge of the magnetic shield hole is scanned. The aperture plane is at the top of the photograph.

FIG. 5.11

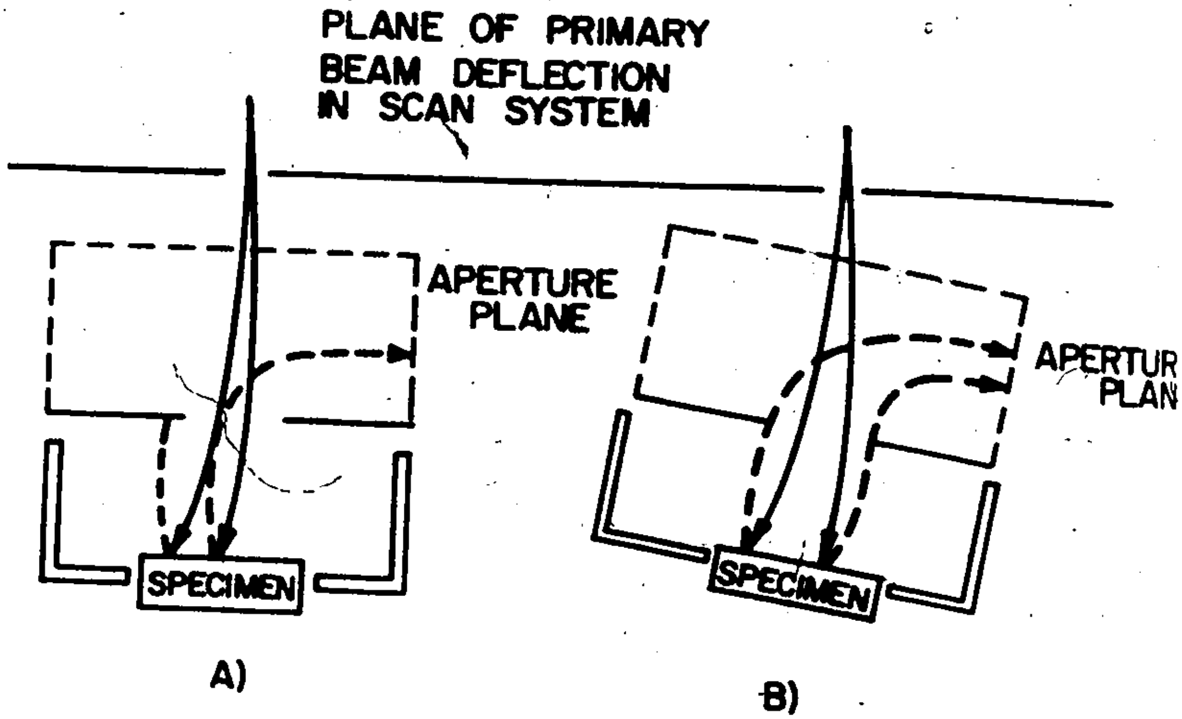

FIG. 5.12

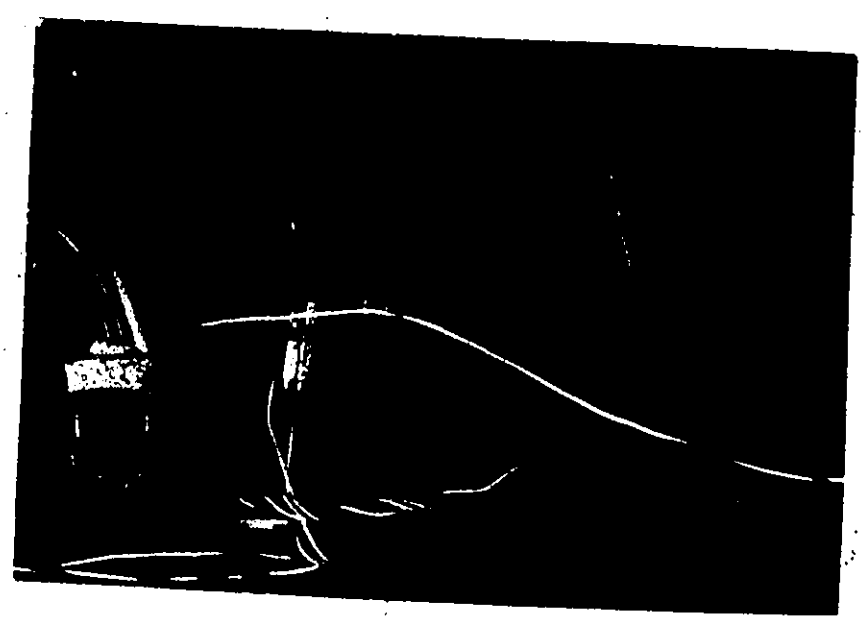

Fig. 5.11

A) The primary beam scan displacement due to deflection in the magnetic field is shown here.

B) The detector assembly may be tilted to compensate for this displacement as shown.

Fig. 5.12

This photograph shows the detector assembly in the tilted position.

specimen also, a normal electrostatic field at the surface of the specimen is maintained. The tilted detector is shown in Figure 5.12 and the results obtained are shown in Figure 5.13. This figure shows that emission is now observed from the whole specimen area and the shadowing effect has been largely eliminated. By carefully adjusting the value of the tilt angle, the shadowing effects can be entirely eliminated.

At this stage in testing the detector, an aperture was placed in the aperture plane. For these initial tests, a rectangular aperture 2.5cm x 0.5cm was used and the magnetic characteristic was again measured. This is shown in Figure 5.14. This curve was obtained at a high value of photomultiplier gain. In spite of this, only the single peak of interest was observed. It is apparent that the detector is now operating as required and all unwanted electron paths to the detector have been eliminated.

The next section deals with the operation of the detector system in a more normal manner, i.e. the magnetic field is maintained constant and the potential on the cage is varied. The problems associated with the primary electron beam moving on the specimen surface are thus eliminated.

5.3 Experimental Testing of the Detector--The Accelerating Field Characteristics

Before operating the detector at a fixed magnetic field it is instructive to determine the magnetic characteristics obtained at various values of accelerating field, with the specimen and specimen box potentials constant. It is expected that, as the cage potential is increased, the secondary electron bundle diameter from the specimen surface would decrease as indicated in the analysis of Chapter 4, and that the secondary electron current density passing through the aperture in the accelerating plane (base of the cage) would increase with increasing accelerating potential giving an increase in the detected signal peak. The signal would reach a maximum with increasing accelerating potential when all the secondary electrons emitted from the specimen surface are collected.

The magnetic field characteristics obtained at various values of accelerating potential are shown in Figure 5.15. As predicted by the analysis, an increase in

FIG. 5.13

Fig. 5.13

With the detector assembly tilted, the primary beam passes through the magnetic shield normal to it as shown in this micrograph.

FIG. 5.14

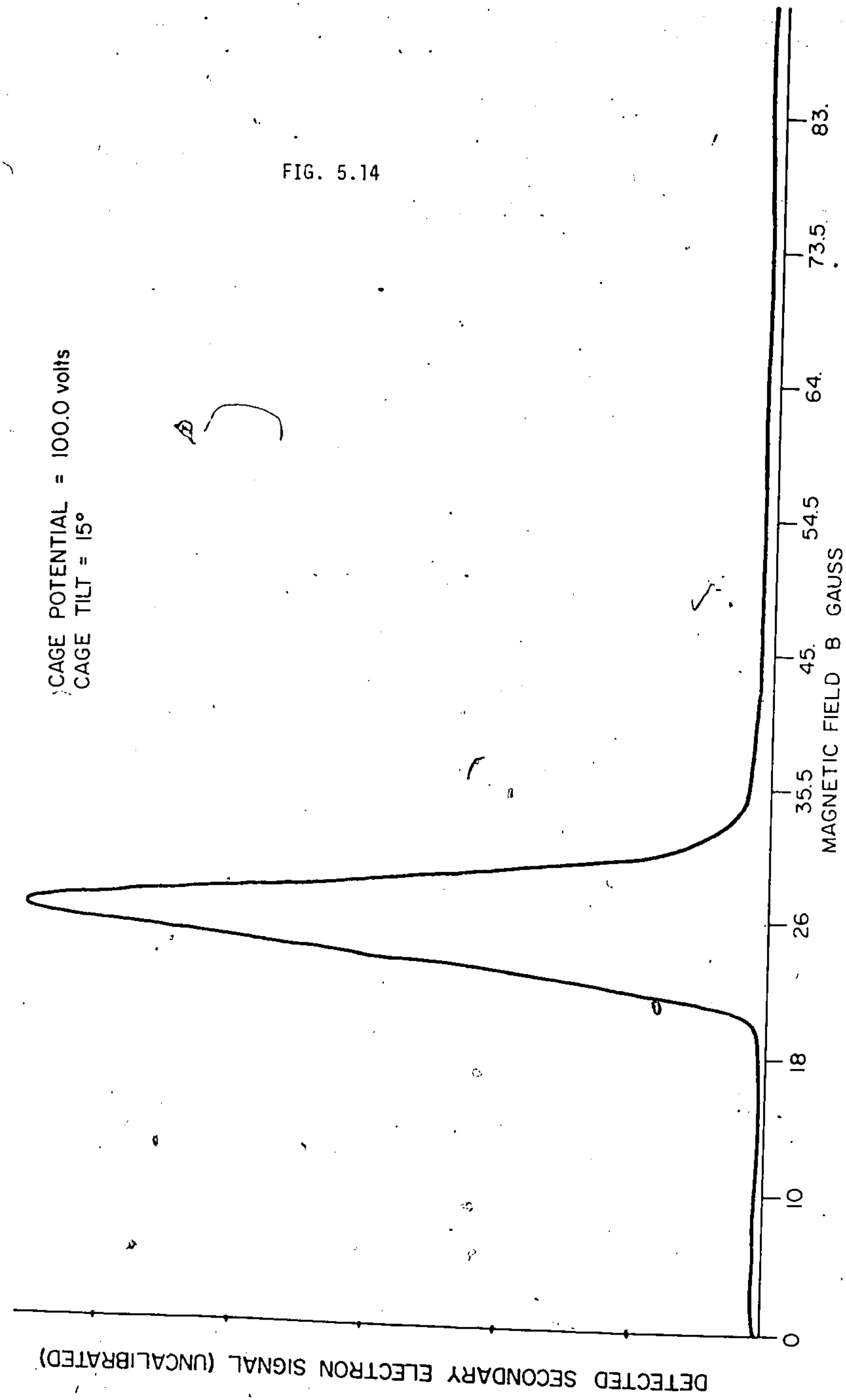

CAGE POTENTIAL = 100.0 volts
CAGE TILT = 15°
MAGNETIC FIELD B GAUSS
0
10
18
26
35.5
45.
54.5
64.
73.5
83.
DETECTED SECONDARY ELECTRON SIGNAL (UNCALIBRATED)

Fig. 5.14

This graph shows magnetic flux density versus detected secondary electron signal showing a single secondary electron peak.

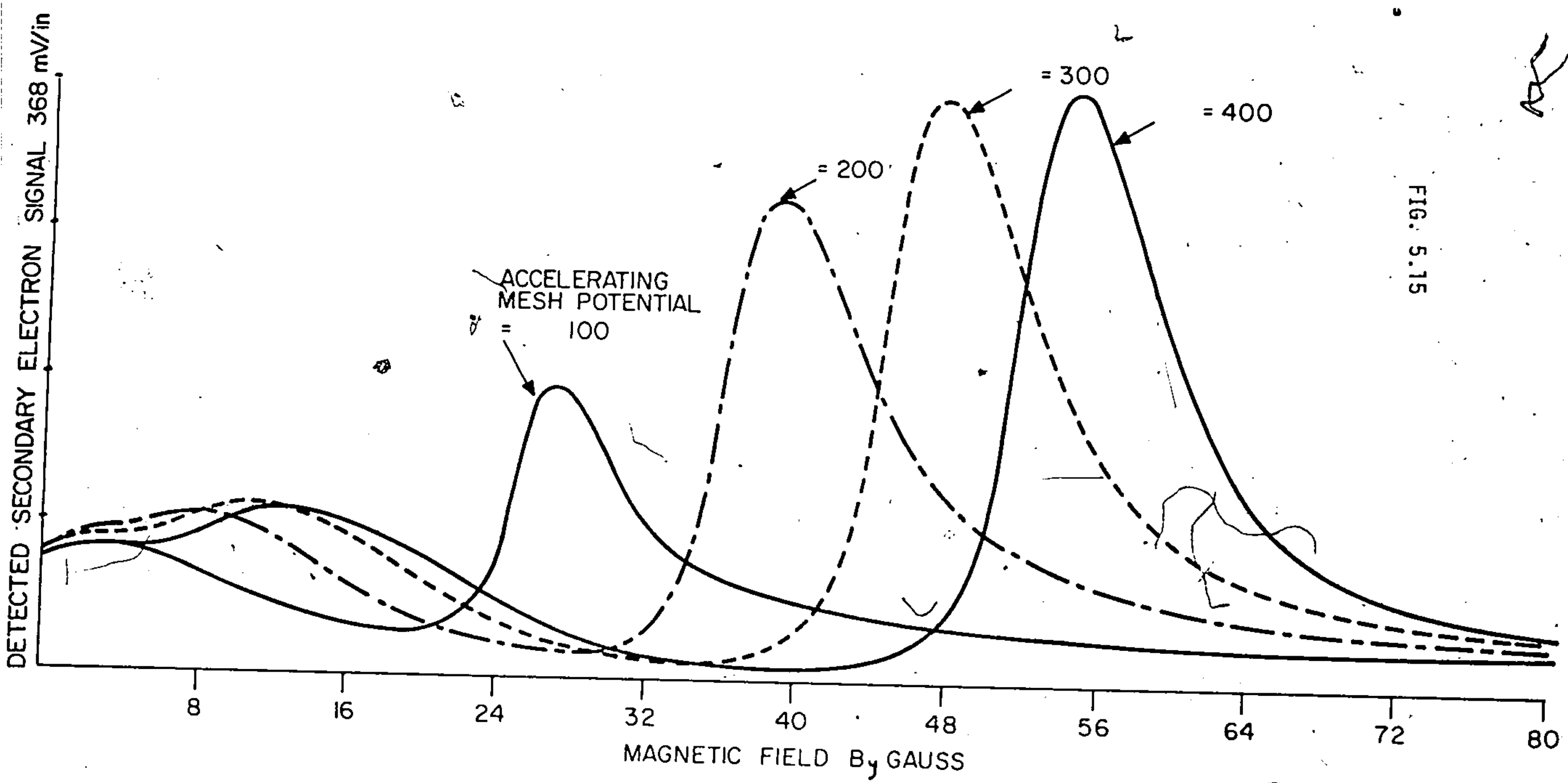

DETECTED SECONDARY ELECTRON SIGNAL 368 mV/in
ACCELERATING
MESH POTENTIAL
V = 100
= 200
= 300
= 400
8
16
24
32
40
48
56
64
72
80
MAGNETIC FIELD By GAUSS

FIG. 5.15

Fig. 5.15

This graph shows magnetic flux density versus detected secondary electron signal with accelerating mesh potential as a parameter.

the peak signal detected is observed as the accelerating potential on the lower surface of the cage is increased from 100 volts to 300 volts. Further increase of this potential produces little further increase in the peak signal detected. The shift in these peaks is due to the increasing energy of the secondary electrons entering the magnetic field as the accelerating field is increased. This necessitates the use of increasing values of magnetic field to produce the required deflection of the bundle onto the aperture plane.

The peaks observed in the curves of Figure 5.15 at low values of magnetic field are possibly due to secondary electrons generated at the edges of the aperture in the base of the cage by backscattered electrons from the specimen surface, (see previous section). It is not clear why these peaks were observed in the present case and not in Figure 5.14. However, as these peaks will not interfere with the proposed operation of the detector, they were not investigated further.

In the next experiment, the magnetic field was maintained constant and the output signal versus accelerating potential characteristic was plotted, again with constant specimen and specimen box potential. As expected, a shape similar to the magnetic characteristics was obtained. This is shown in Figure 5.16. The shape of this curve is important as it is similar to that expected when the specimen potential is varied (see next section). As can be seen from Figure 5.16, the output signal is nearly linear with accelerating potential over a wide range on both sides of the peak.

The specimen voltage characteristic at constant magnetic field and accelerating field is discussed in detail in the next section.

5.4 Experimental Testing of the Detector--The Specimen Potential Characteristic

If the accelerating potential and the magnetic field are held constant and the output signal as a function of specimen potential is observed, a characteristic similar to that of Figure 5.16 would be expected. This is because it matters little whether the accelerating field is varied by varying the accelerating potential on the lower surface of the cage or the specimen potential. A characteristic obtained by varying the specimen potential is shown in Figure 5.17.

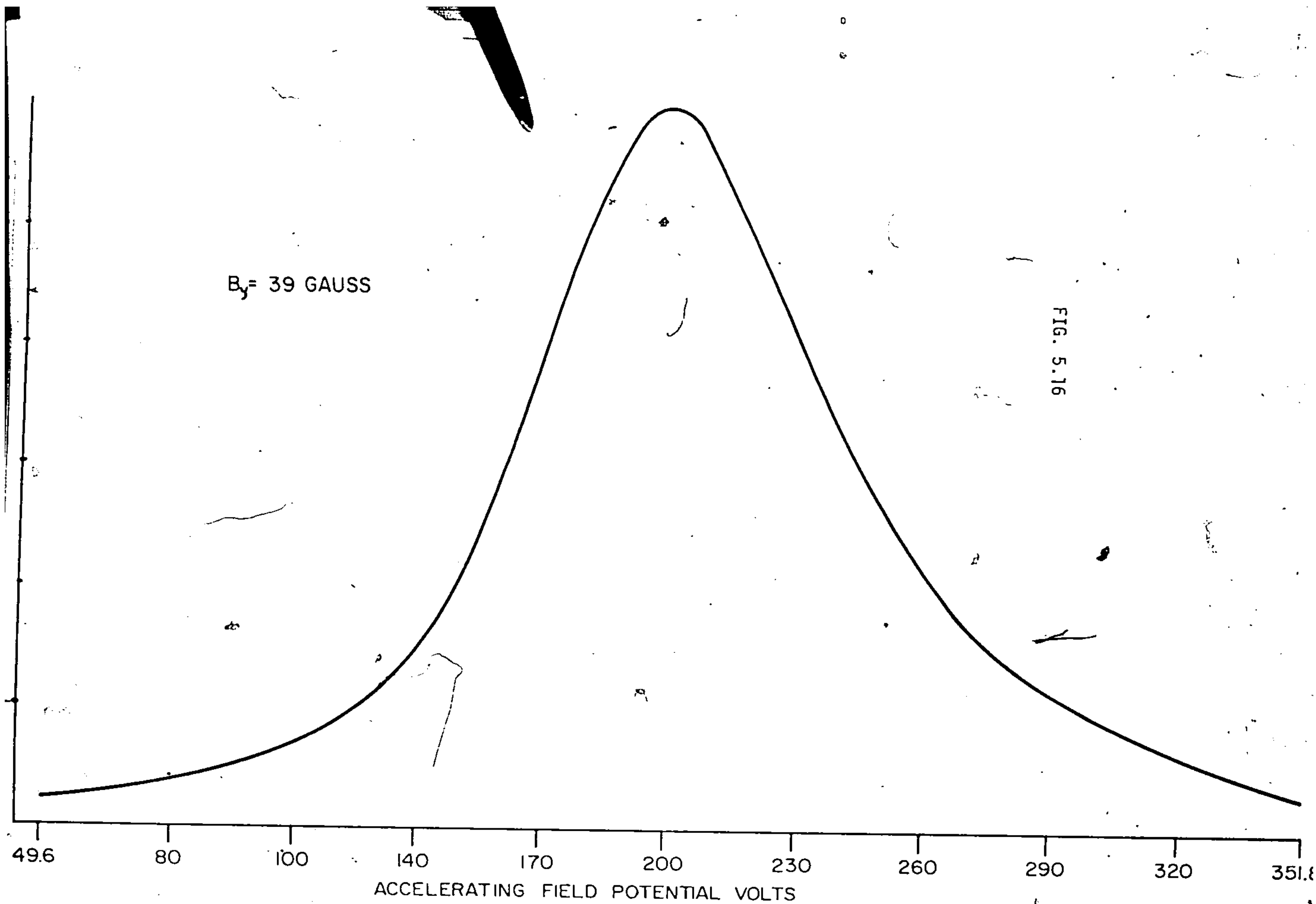

B_y= 39 GAUSS
49.6
80
100
140
170
200
230
260
290
320
351.8
ACCELERATING FIELD POTENTIAL VOLTS

FIG. 5.16

Fig. 5.16

Accelerating field potential versus detected secondary electron signal is shown in this graph.

B = 39 gauss
Specimen Potential = 0.0 volts

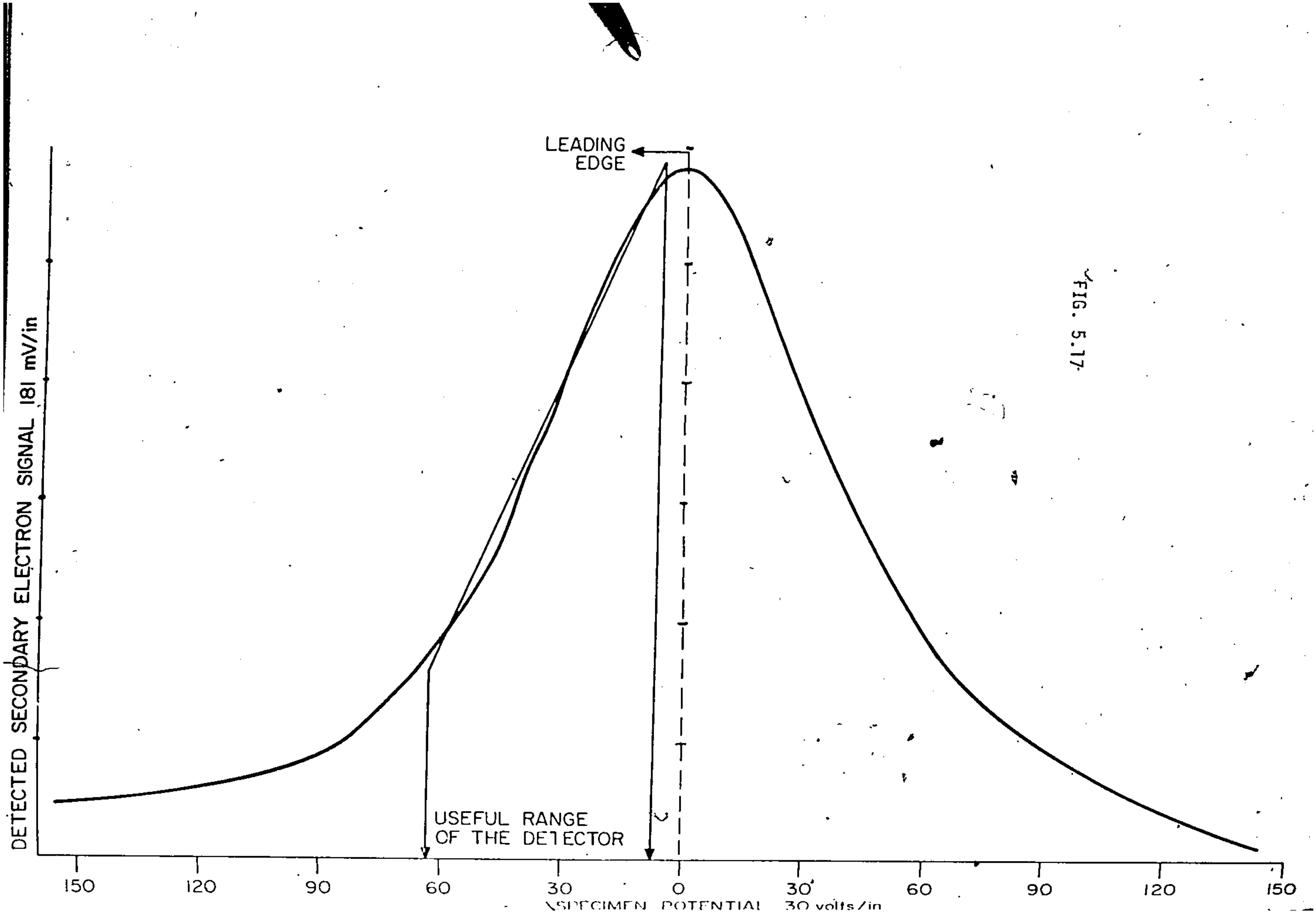

LEADING EDGE
USEFUL RANGE OF THE DETECTOR
DETECTED SECONDARY ELECTRON SIGNAL 181 mV/in
150
120
90
60
30
0
30
60
90
120
150
SPECIMEN POTENTIAL 30 volts/in

FIG. 5.17

Fig. 5.17

This graph shows specimen potential versus detected secondary electron signal.

B = 39 gauss
Accelerating potential = 200 volts.

The useful range of the detector is that over which a nearly linear variation of output signal with specimen potential is obtained, this range is indicated in Figure 5.17. It should be noted that the zero specimen potential point on the horizontal axis can be positioned anywhere on the characteristic by adjusting the accelerating potential and the magnetic field strength.

Figure 5.17 suggests that the leading edge of the peak is the useful range; the trailing edge could also be used if this proved to be more linear and of better range and sensitivity. These are the three parameters of interest in the type of detector characteristic shown in Figure 5.17 i.e., the range, the sensitivity and the linearity over the specified range. These three parameters are obtained in the following manner. The best straight line approximation to the curve of interest is superimposed on the curve over the range of interest. The sensitivity over this range is then given by the slope of the linear approximation to the curve either in millivolts/volt or as a percentage. The linearity over the specified range is given by the maximum deviation of the actual curve from the linear approximation in the range divided by the total output signal excursion over the range.

As the characteristics of the secondary electron bundle arriving at the aperture plane are fixed by the specimen potential, the magnetic field and the accelerating potential, the three parameters of interest may be empirically optimized by altering the shape of the analysis aperture used. Some magnetic characteristics for different aperture shapes are shown in Figure 5.18. As can be seen, the detailed shape of the characteristic can be tailored by the shape of the aperture chosen. Table 5.19 shows a more complete list of the results obtained from a variety of aperture shapes used.

From these preliminary tests it can be concluded that, for the specified operating range of the detector of ±20 volts, the best aperture shape is the large rectangle. This gives a range of ±24 volts with a sensitivity of 15.6 mV/V and a linearity of 3% over this range.

FIG. 5.18

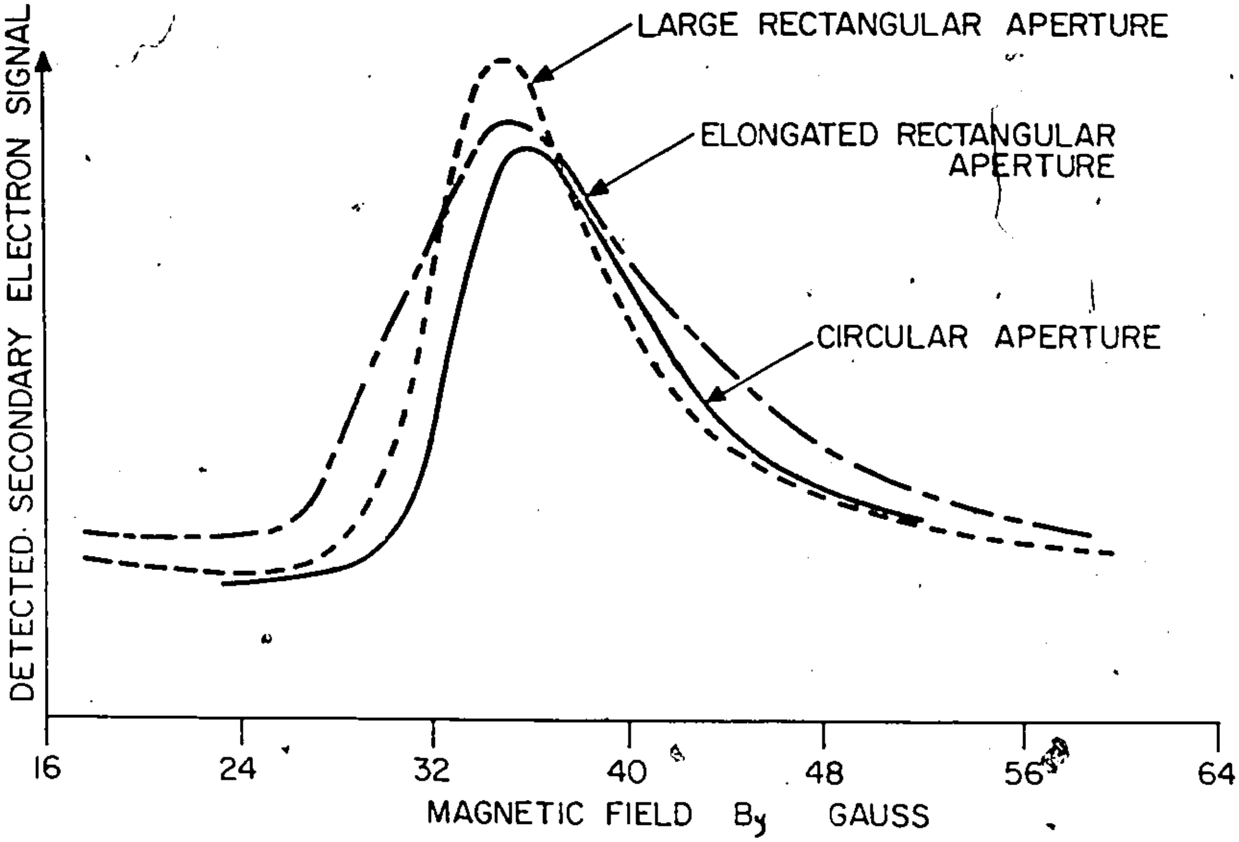
LARGE RECTANGULAR APERTURE
ELONGATED RECTANGULAR APERTURE
CIRCULAR APERTURE
DETECTED SECONDARY ELECTRON SIGNAL
16
24
32
40
48
56
64
MAGNETIC FIELD B_y GAUSS

Fig. 5.18

This graph shows magnetic flux density versus detected secondary electron signal with the aperture shape and size as a parameter.

TABLE 5.19

Aperture Shape	Sensitivity	Voltage Range	Linearity
Large Rectangle	15.6 MV/V	48.1	3.0%
Small Rectangle	12.9 MV/V	46.2	4.8%
Star	7.7 MV/V	113.0	4.6%
Large Diamond	6.3 MV/V	113.25	3.2%
Small Diamond	14.9 MV/V	18.8	.5%
Circle	17.0 MV/V	32.08	2.7%
Half Diamond	21.1 MV/V	37.0	3.5%
Flat Top Half Diamond	15.7 MV/V	47.0	4.1%
Crescent	10.6 MV/V	98.15	8.6%

All these results were taken from the leading edges of the peaks.

Table 5.19

The results of the aperture study are given here.

5.5 Transverse Field Studies

The experiments carried out above were performed on a planar specimen with little topographic detail on the surface. The specimen used was a highly polished piece of silicon. For the work in this section, a new specimen is needed on which controlled transverse fields can be generated so that the effects of such fields on the operation of the detector can be observed.

The specimen used is shown in Figure 5.19. This specimen, which was designed specifically for transverse field studies, consists of nine aluminum electrodes evaporated onto a silicon wafer. A central electrode is coupled to a large bonding pad at the top of the specimen in Figure 5.19. Pairs of electrodes are then spaced on either side of this central electrode at four different spacings. The spacing varied from 10μ to 25μ and the central electrode was 10μ wide. The specimen was mounted on a transistor header and bonded conventionally so that potentials could be applied to the individual electrodes.

As was discussed in Chapters 3 and 4, at low values of accelerating potential (normal field at the specimen surface) the presence of transverse fields at the specimen surface will affect the collection of the emitted secondary electrons. If the area scanned by the primary electron beam is positive with respect to the surrounding area, then the transverse field will oppose the accelerating field and, depending on their relative magnitudes, a reduction in the number of electrons collected can be produced. It was also shown how transverse fields parallel to the surface of the specimen can deflect the emitted electrons and effect their collection.

Figure 20 A) and B) show some preliminary results obtained using the detector system to examine one of the pads of the specimen shown in Figure 5.19. The accelerating potential used was 500 volts which, with the geometry used would produce a normal field strength of 5×10^4 volts/metre at the specimen surface.

In Figure 5.20 A), the pad is made progressively more negative in steps: -5, -10, -15 and -20 volts while the other pads and the substrate were held at ground potential. The width of the dark shadow around the edges of the pad increases in

FIG. 5.19

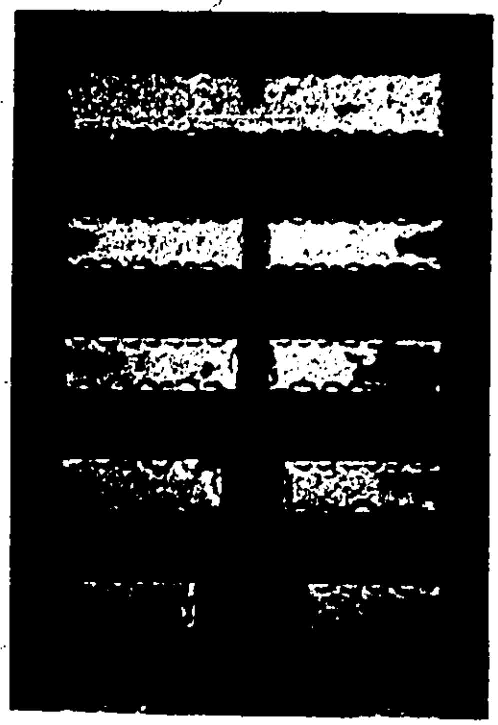

Fig. 5.19

The test specimen used to study transverse fields is shown in this figure.

FIG. 5.20

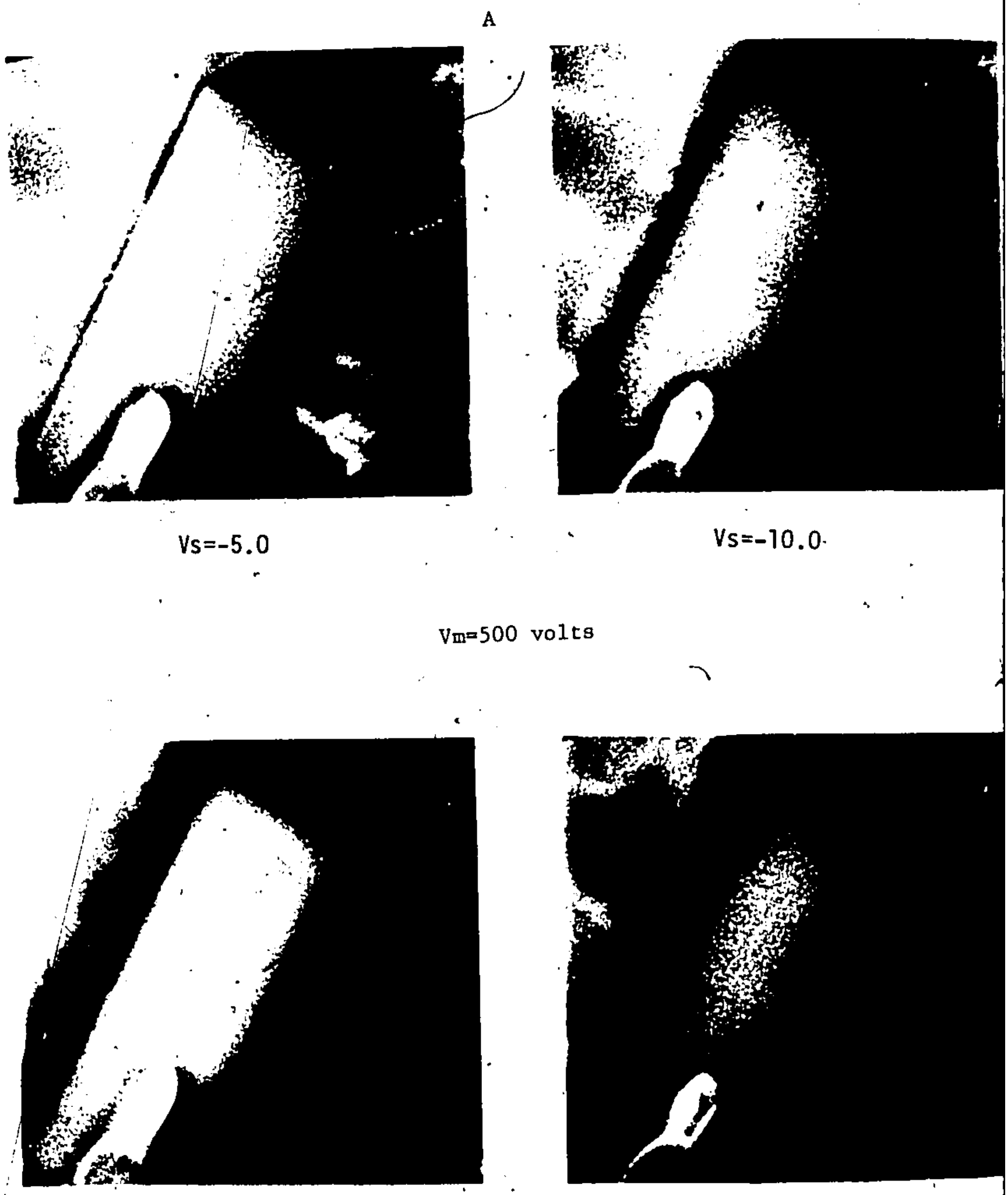

Vs=-5.0

Vs=-10.0

Vm=500 volts

Vs=-15.0

Vs=-20.0

Fig. 5.20(a)

The study of transverse fields using the test specimen (one mesh detector) is followed in these photographs. The specimen potential is indicated below the photographs.

Accelerating mesh = 500 volts
Specimen potential is the parameter.

B

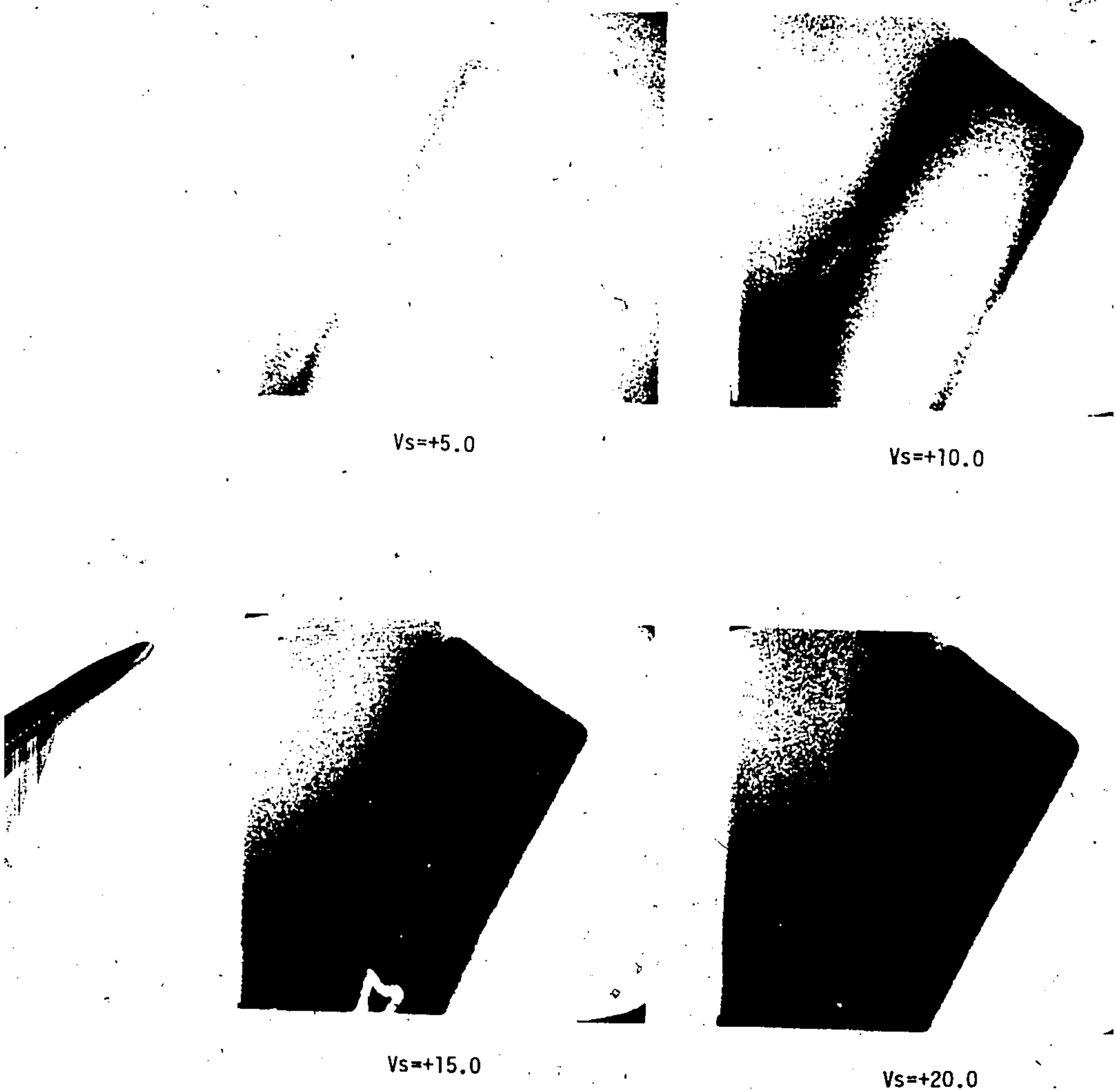

Fig. 5.20(b)

The transverse field study is continued in this series of photographs with a change in specimen potential.

width as the bias voltage in increased. This is due to the increasing vertical component of the transverse field at the edges of the pad. As discussed in Chapter 3, this contrast is known as Field Contrast and is one of the effects produced by transverse fields which hinder the observation of voltage contrast. It is difficult to detect voltage contrast in Figure 5.20 A) with any certainty because of this. The cause of the extended dark shadow on the right in these micrographs has not been explained, however, it was thought that this may be associated with the non-parallelism of the specimen surface and the bottom plane of the detector cage but this was not confirmed.

In Figure 5.20 B) the pad is biased progressively more positive in steps: +5, +10, +15 and +20 volts. Again, the dark shadow due to the vertical transverse field component at the edges of the pad is evident. In addition, the emission from the pad is reduced as the pad is made more positive indicating that secondary electrons emitted from the pad are being returned to the pad by the local field. The extended dark shadow on the left in these micrographs is similar to that observed in Figure 5.20 A) and again it was not fully explained, nor were the other detailed effects observed in these micrographs.

In spite of the unexplained details of the micrographs shown in Figures 5.20 A) and B), they do serve to illustrate some of the effects of transverse fields discussed in Chapters 3 and 4.

It is clear from the above results that a normal field at the surface of the specimen of 5×10^4 volts/m, which was determined from the analysis of Chapter 4, is not sufficient to control the effects of transverse fields adequately. Using the present detector arrangement, it is difficult to increase this field because if the potential on the base of the cage is increased then the strength of the magnetic field must also be increased. The increased power dissipation in the magnet coils produces an increase in the outgassing rate of the wire insulation which spoils the vacuum environment and the coils are eventually destroyed.

In Chapter 4 it was shown how an extra grid may be introduced between the base of the cage and the specimen. This grid can then be used to provide the normal field at the specimen surface, and the base of the cage then acts to retard the electrons again so that a low magnetic field strength can be maintained. An extra grid was fitted to the detector system as is shown in Figure 5.21. This grid was positioned 0.25" above the specimen surface and the insulation used allowed potentials up to 2 kV to be applied to the grid before breakdown occurred. This produces a normal field strength of up to 3 x 10^5 volts/m. This new arrangement was used to observe one of the pads on the specimen studied above. The results are shown in Figure 5.22. The pad was biased at +20 volts, the base of the cage (retarding electrode) was biased at +200 volts and the accelerating mesh potential was varied from 500 volts to 2 kV with a fixed magnetic field.

The micrograph obtained at an accelerating potential of 500 volts, as in Figure 5.20, shows very little signal from the pad due to the effects of transverse fields. As the accelerating potential is increased, an increasing signal is obtained from the pad as the retarding transverse fields are overcome by the accelerating field. At an accelerating potential of 2 kV, although the shadow effect is still evident at the edges of the pad, the central area of the pad shows no shadow and its contrast is related to its voltage only i.e. voltage contrast can now be seen with some degree of confidence.

At this point it was felt that the present detector had provided as much data as was needed in order to be able to design a more versatile detector. The design of this second detector is described in the next chapter together with the results obtained from it.

5.6 Summary and Conclusions

The design and testing of the first prototype surface voltage detector has been described in this chapter. It has been shown that the proposed detector configurations using an electrostatic field and a lateral magnetic field operate successfully. In order to meet the design criteria laid out in Chapter 3 however, a new detector must be built based on the experience and results gained from the one described in this chapter.

FIG. 5.21

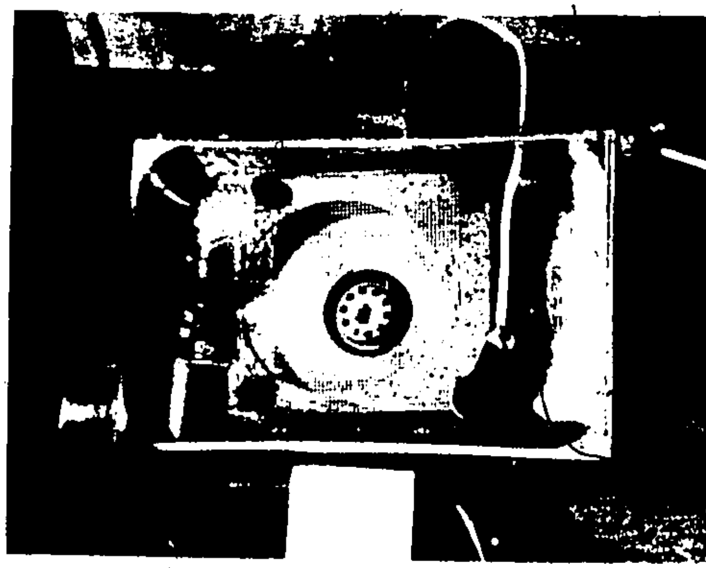

Fig. 5.21

A second grid was mounted on the specimen box, this grid to generate a high normal accelerating field at the specimen surface.

FIG. 5.22

(a)
Vm= 500.

Vs=+20.

(b)
Vm= 1000.

(c)
Vm= 1500.

(d)
Vm= 2000.

Fig. 5.22

This series of photographs illustrate the transverse field studies performed using the two mesh system. The accelerating mesh potential is the parameter.

Retarding mesh potential = 200 volts
Specimen potential = +20 volts

Before this new detector is discussed and the results from it are described, several conclusions can be drawn from the experiments which have been discussed in this Chapter. These conclusions are best described in point form.

a) The use of aluminum foil to eliminate unwanted electron paths to the detector and the resultant peaks on the magnetic characteristic (section 5.2) suggests that the electrostatic cage should have solid rather than mesh surfaces. A non-magnetic material such as aluminum would be suitable except for the base plane (the accelerating plane) which should be made of a magnetic material to reduce the stray fringing magnetic field at the specimen surface.

b) To compensate for the primary beam deflection within the magnetic field and to ensure that the beam scans an area of the specimen directly below the aperture in the base plane of the detector, this base plane should be tilted at an angle dependent on the magnetic field strength and the energy of the primary electron beam used. Also, the specimen must be tilted at the same angle to ensure that the accelerating plane of the cage and the specimen surface are parallel.

c) It is apparent from the preliminary empirical tests carried out to determine the best aperture shape that a large rectangular aperture provides the best overall range, sensitivity and linearity. A range of ±24 volts with a sensitivity of 15.6 mV/volt and a linearity of 3% were achieved using the first prototype.

d) In order to keep the physical size of the detector small so that it interferes as little as possible with the normal operation of the SEM, the size of the magnet coils must be kept to a minimum. Because of power dissipation problems, which are compounded by the fact that the coils must be operated in a vacuum, the detector must operate at a low value of magnetic field. This also produces the minimum primary electron beam deflection and distortion. The use of a low magnetic field in turn implies that the energy of the electrons entering the magnetic field must be kept as low as possible by the use of a retarding field in addition to the accelerating field.

e) It appears that the use of a high normal electric field at the specimen surface (of the order of 5 x 10^5 volts/m) will effectively control the influence of

...15

transverse fields so that meaningful voltage measurements can be made, as long as such measurements are performed at a distance of approximately 5μ from the interface of two areas at different potentials. In the interface region, field effects cannot be controlled and voltage measurements cannot be made.

CHAPTER SIX

FINAL DETECTOR DESIGN AND TESTING

Introduction

The experiments described in Chapter Five have shown that the basic detector arrangement performs as a surface voltage detector. The data obtained indicates that in order to optimize the design, some modifications must be made. The construction of a new detector which includes these modifications and improvements is described in this chapter. The results obtained using this new detector are discussed and suggestions for further work on this type of detector system are outlined.

6.1 The Detector Construction

When a deaccelerating grid is used with the detector, the size of the secondary electron bundle arriving at the aperture plane will be much smaller than in the case where only a single grid is used. This has been shown by the results of Chapter 4. Because of the reduced size of the secondary electron bundle, the size of the detector can be reduced. A cage width of .75" and a length of 1.5" were chosen. The new detector is shown schematically in Figure 6.1 and photographically in Figure 6.2. The main body of the cage is made of aluminum and a cold-rolled steel cage base plate is used to reduce the stray fringing magnetic field strength at the specimen surface. This base plate is pivoted at the aperature plane end of the detector so that it can be tilted to compensate for the deflection of the primary electron beam in the magnetic field. In addition, this base plate was designed so that an accelerating mesh could be mounted beneath it. This is shown in position in Figures 6.1 and 6.2. Also shown is an extra section located between the cage and the Everhart-Thornley type of electron detector. This section is included so that a retarding field energy analyzer can be added to the detector at a later date (see future work).

FIG. 6.1

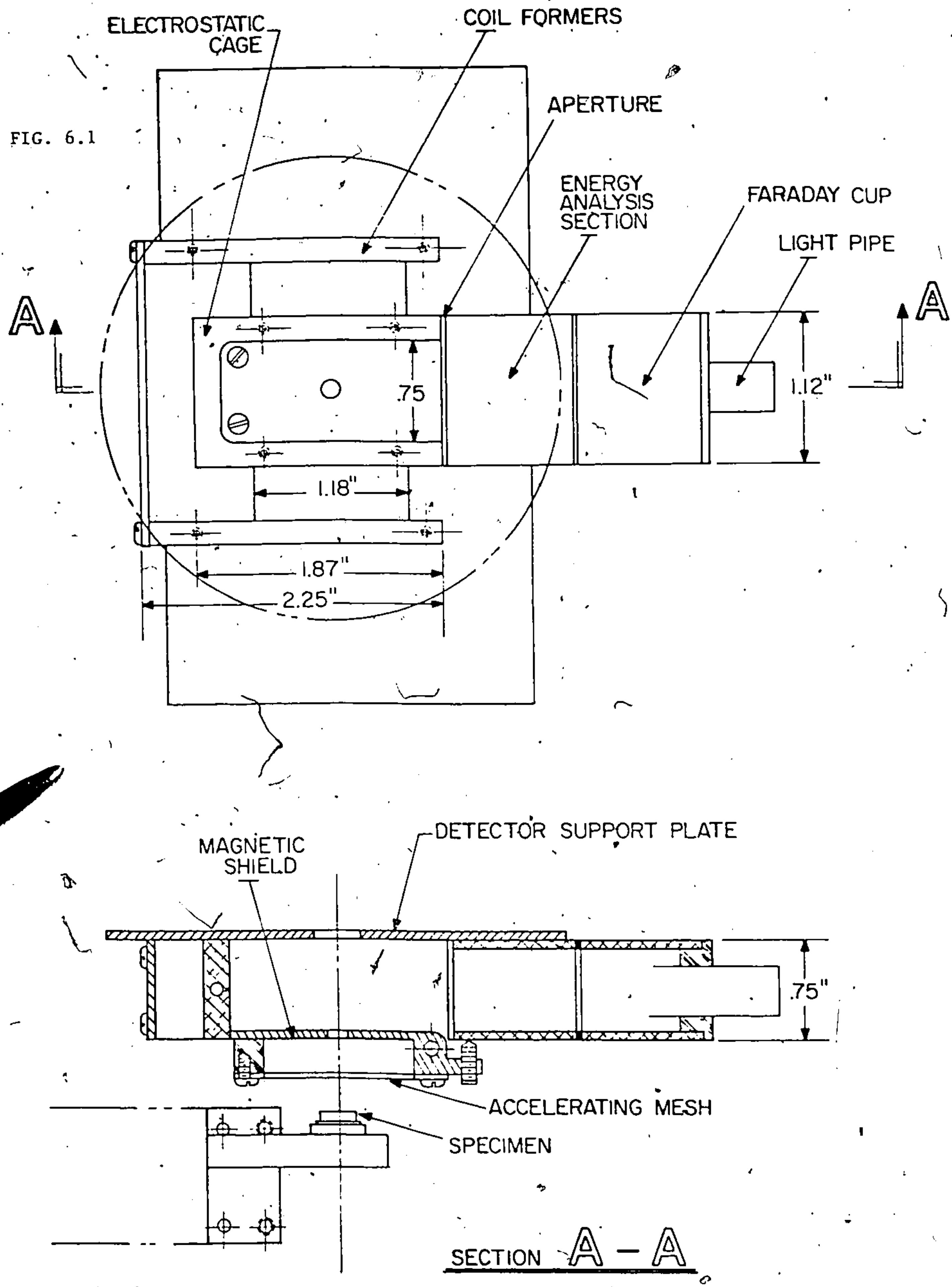
ELECTROSTATIC CAGE
COIL FORMERS
APERTURE
ENERGY ANALYSIS SECTION
FARADAY CUP
LIGHT PIPE
A
A
.75
1.12"
1.18"
1.87"
2.25"
MAGNETIC SHIELD
DETECTOR SUPPORT PLATE
.75"
ACCELERATING MESH
SPECIMEN
SECTION A – A

Fig. 6.1

This figure shows the schematic drawing of the redesigned detector system showing the six important sections.

1) Detector support plate
2) Electrostatic cage
3) Coil former
4) Shield and mesh assembly
5) Aperature and energy analysis section
6) Everhart-Thornley collector.

FIG. 6.2

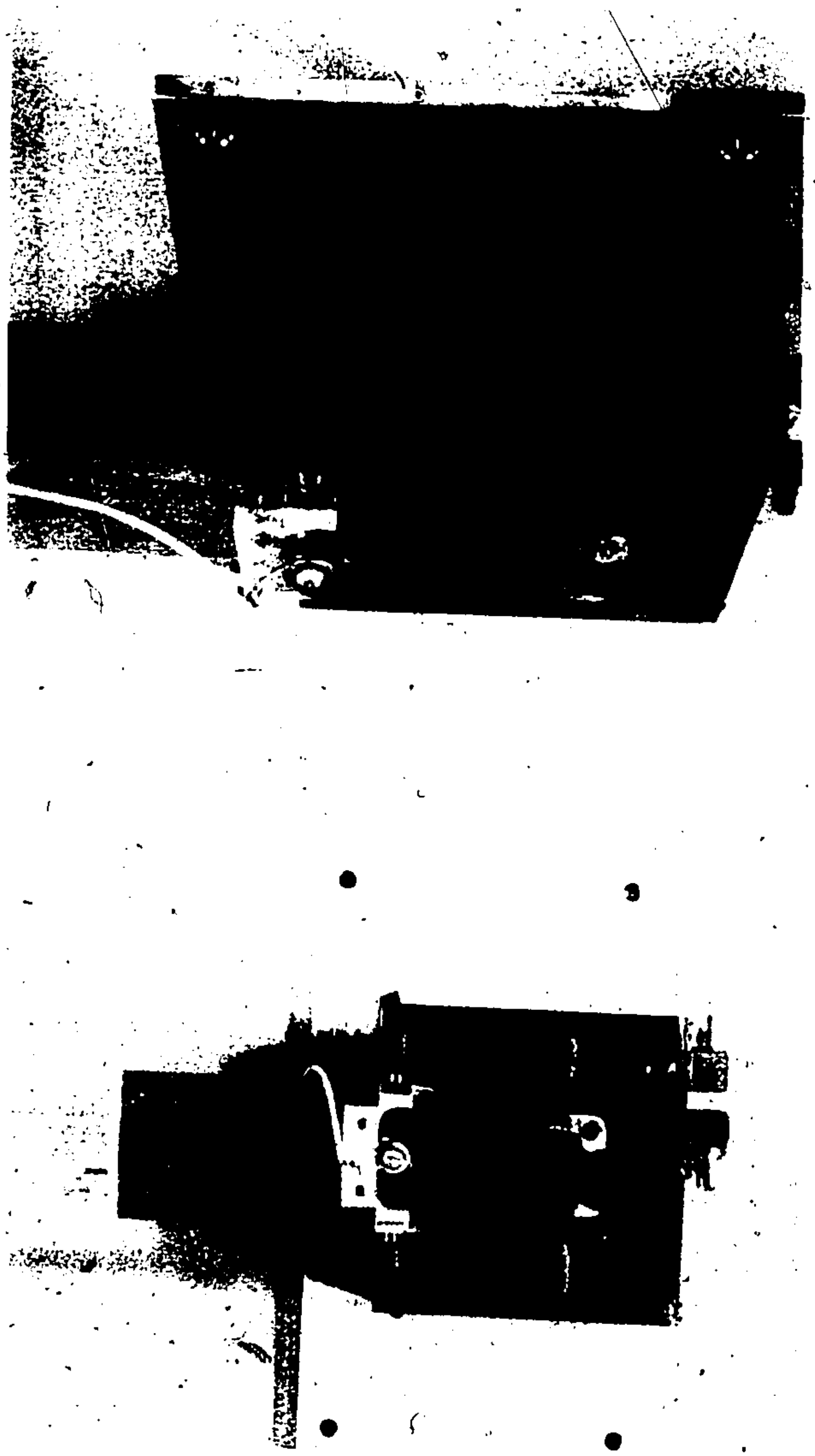

Fig. 6.2

These photographs show the redesigned detector system. The hinged mesh assembly showing the two mesh system. Accelerating mesh, and magnetic shield plate may be seen in the top photograph.

As in the case of the first detector, the magnetic coils are wound on cold-rolled steel pole pieces and the magnetic circuit is completed by a cold-rolled steel plate at the rear of the detector. Each of the coils is wound with 500 terns of #30 wire and a flux density of 15 gauss was measured in the cage at a coil current of 110 mA. The coils were potted using Epotch 360 (available from the Epoxy Technology Corporation). This provides a low out-gassing load for the vacuum pumping system of the SEM. The entire assembly is mounted on an aluminum base plate so that it could be suspended from the bottom surface of the electron optical column of the microscope rather than on the specimen stage as was the case for the first detector.

The first part of the testing of this new detector was carried out using the Mini-SEM. This is an instrument designed and built at the Communications Research Centre. The specimen stage for the Mini-SEM was used, with a small addition to support the specimen at the correct height and tilt angle relative to the detector. However, the final tests were again carried out using the Stereoscan SEM because of an electronics problem on the Mini-SEM associated with the scan amplifier. Figure 6.3 shows the view through one of the ports of the specimen chamber of the Stereoseon showing the detector mounted in position and the Mini-SEM specimen stage.

6.2 Results obtained using a One Electrode System

The experimental testing of the new detector was carried out in two parts. The first part studied the behaviour of the detector using the cage base plate as an accelerating electrode whereas the second part of the work was carried out with an accelerating grid fitted, the cage base plane then acting as a retarding field electrode.

In the first experiment, using the cage base plane as the accelerating electrode, the aperature in this plane was covered with nickel mesh (.002" wires

FIG. 6.3

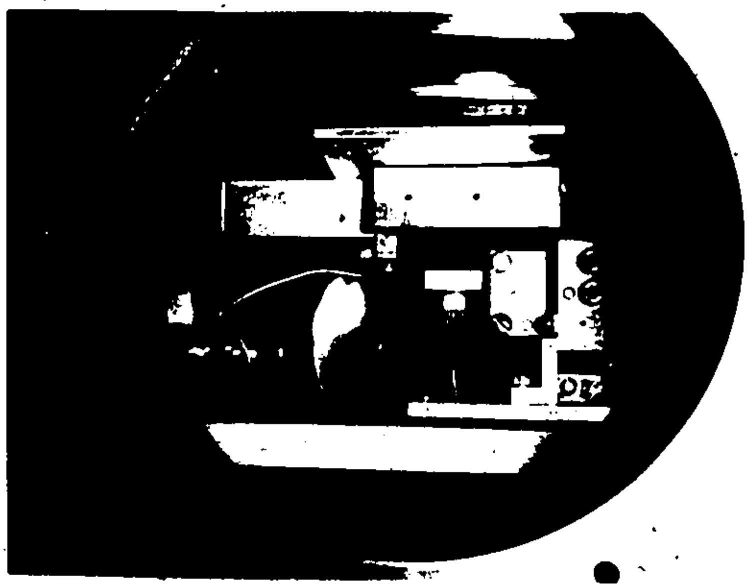

Fig. 6.3

The detector is shown mounted on the pole piece of the Steroscan SEM, the specimen socket, support bracket and stage can be seen below and to the right of the detector.

at .018" spacing) in order to reduce the distortion of the electrostatic field at the specimen surface produced by this aperature. Following the general procedure described in Chapter 5, the magnetic characteristics for the detector were obtained with a rectangular aperature fitted in the aperature plane of the cage. The magnetic characteristics obtained at three different values of a cage potential are shown in Figure 6.4 at a fixed base plane tilt angle of 5^o. These curves show that only the secondary electrons of interest are being detected and that no unwanted electron paths to the detector are present.

An increase in the peak heights of these curves was expected as the cage potential was increased (as was observed using the first detector, see Figure 5.15). However, a reduction in peak signal was observed at 600V compared to 400V. It was suspected that this was because results were obtained at a fixed value of tilt angle although three values of magnetic field were used. This suspicion was supported by the observation of a shadowing effect of the specimen at a cage potential of 600V as discussed in section 5.2. This could reduce the number of secondary electrons collected and produce the peak signal reduction observed at 600V. This explanation was verified by increasing the tilt angle of the base plane at 600V whereupon an increase in the signal was produced.

The electrostatic cage potential characteristics were plotted by measuring the detector output signal versus the cage potential at a constant magnetic field, a base plane tilt angle of 5^o and a specimen potential of zero volts. These results are shown in Figure 6.5. As anticipated from the results obtained in Chapter 5, an increase in the peak signal detected was observed at the higher values of magnetic field (and consequently, the higher values of accelerating potential). In addition, a pronounced broadening of the peak was observed at the higher value of magnetic field. The reason for the broadening of

... explain the

FIG. 6.4

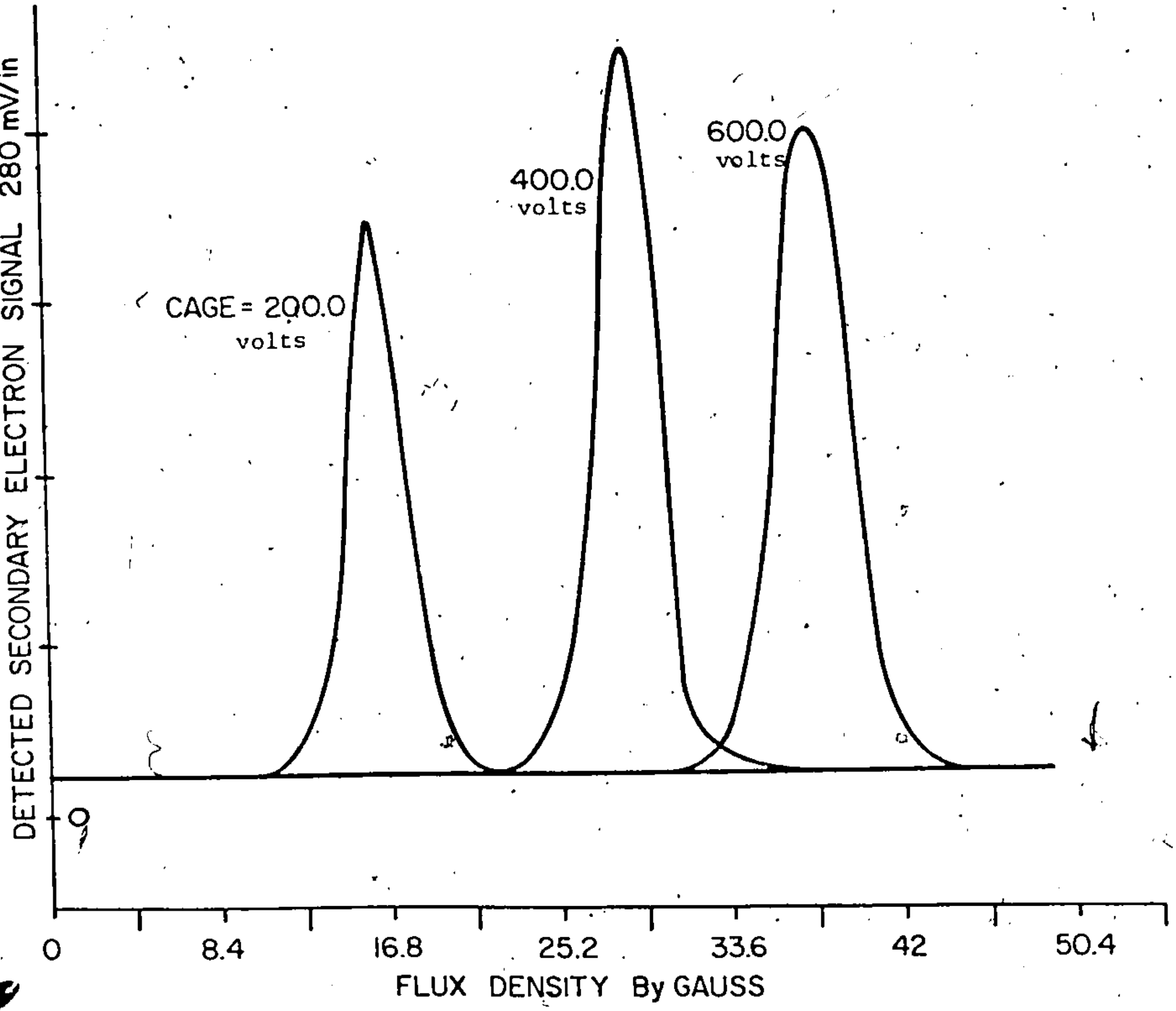
DETECTED SECONDARY ELECTRON SIGNAL 280 mV/in
CAGE = 200.0 volts
400.0 volts
600.0 volts
0
0
8.4
16.8
25.2
33.6
42
50.4
FLUX DENSITY By GAUSS

Fig. 6.4

This graph shows flux density versus detected secondary electron signal, electrostatic cage potential as a parameter.

Specimen potential = 0.0 volts

Cage base plane tilt = 5^{o}

I Beam = 5×10^{-9} amps

Electron gun potential = 20 KV

Rectangular aperature used.

FIG. 6.5

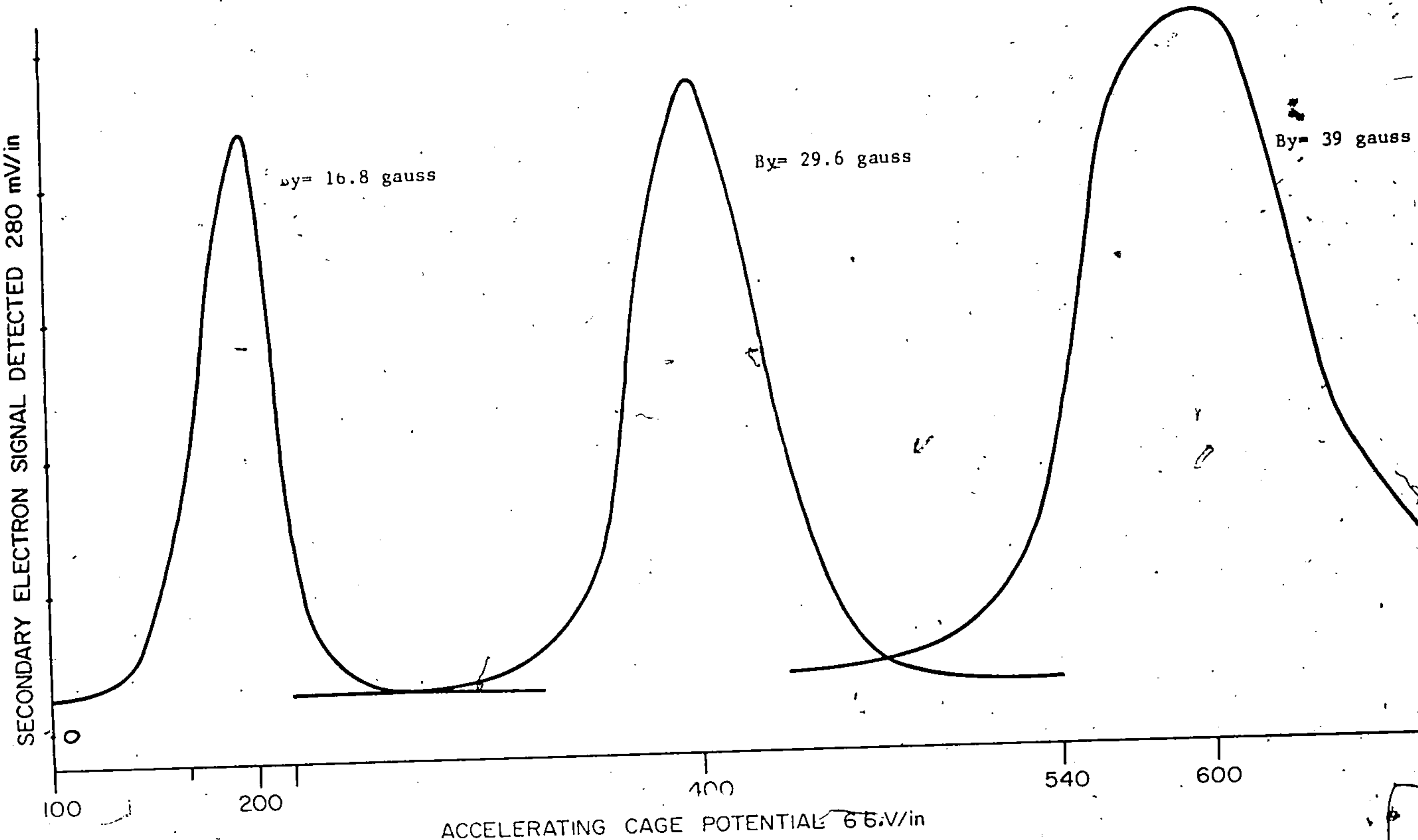

By= 16.8 gauss
By= 29.6 gauss
By= 39 gauss
SECONDARY ELECTRON SIGNAL DETECTED 280 mV/in
0
100
200
400
540
600
ACCELERATING CAGE POTENTIAL 66 V/in

Fig. 6.5

This graph shows accelerating cage potential versus secondary electron signal detected with magnetic field as a paremeter.

Specimen potential = 0.0 volts

Cage base plane tilt = 5^{o}

detailed processes which occur in the detector. For the present, the work was limited to the characterization of the total system as a surface voltage detector.

Again, using the optimum rectangular aperature shape determined in Chapter 5, the specimen potential versus output signal characteristics was measured using a unipotential specimen i.e., with no transverse fields present. The characteristic obtained is shown in Figure 6.6. A cage potential of 400 volts and a magnetic field strength adjusted to yield peak signal at a specimen potential of + 20 volts was used. This corresponds to operation on the leading edge of a characteristic very close to the central one of Figure 6.5.

This characteristic shows a linearity of 12% over a ± 20 volt range of specimen potential with a sensitivity of 40.4 mV/volt. The measurements were performed at a primary beam current of 5 x 10^{-9} amps and a beam energy of 20 KeV.

Using the multi-electrode specimen described in section 5.6, the effects of transverse fields were investigated. Results similar to those obtained in Chapter 5 were recorded. The cage base plane potential could not be raised to a sufficiently high value to reduce the effects of transverse fields because of power dissipation problems in the magnetic field coils. At this point, the second grid was fitted to the detector and the results described below were obtained.

6.3 Results Obtained Using a Two Electrode System

The detector with the extra grid mounted is shown in Figures 6.1 and 6.2. It was shown analytically in section 4:2 that, as the accelerating potential increases, the net lateral electron deflection at the retarding field plane decreases resulting in an increase in the secondary electron current density within the bundle. This should result in a higher secondary electron current density passing through the aperature in the cage base plate which will give an

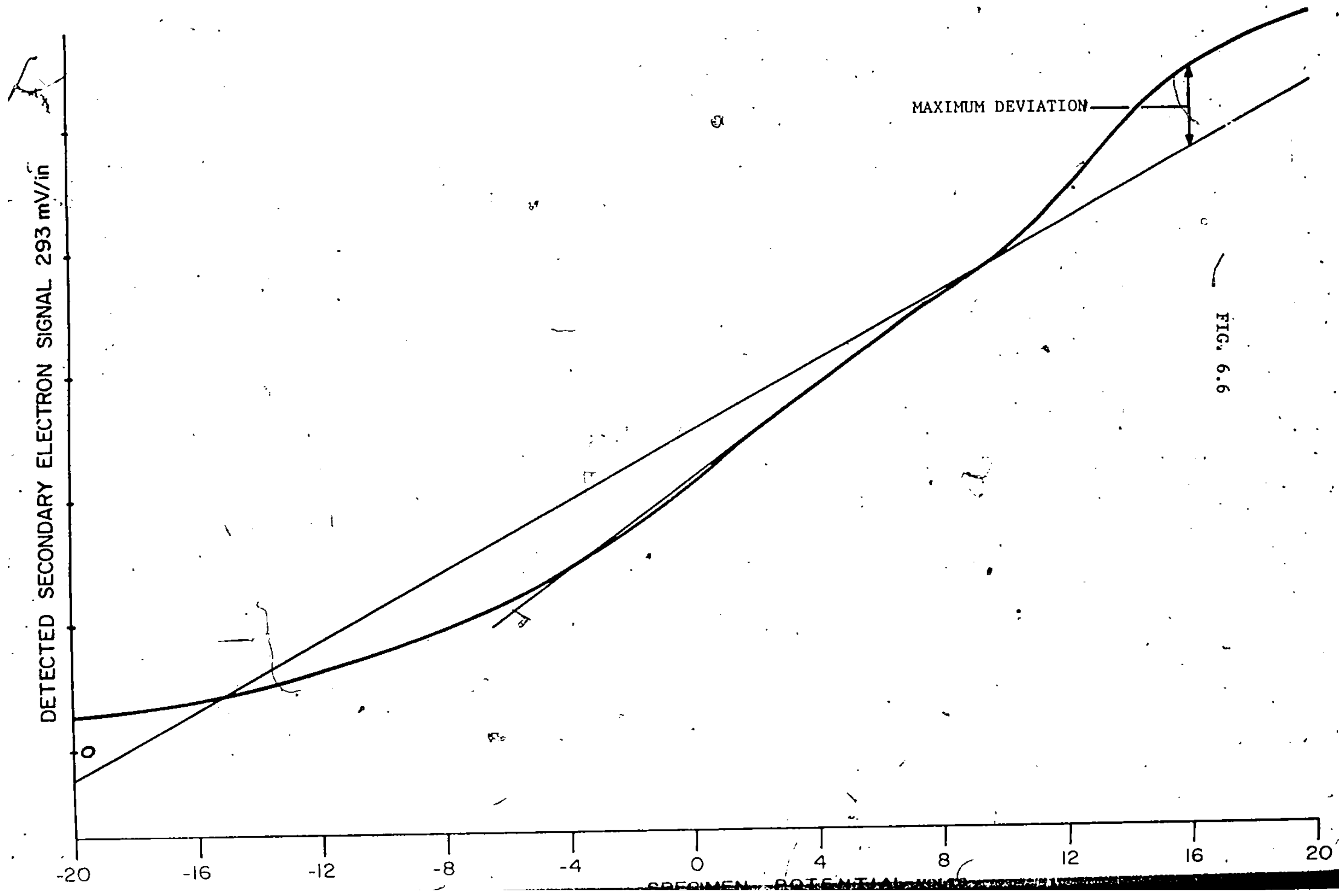

DETECTED SECONDARY ELECTRON SIGNAL 293 mV/in
MAXIMUM DEVIATION
0
-20
-16
-12
-8
-4
0
4
8
12
16
20

FIG. 6.6

Fig. 6.6

This graph plots specimen potential against detected secondary electron current.

Cage potential = 400 volts.

increase in the secondary electron detected signal peak. The curve presented in Figure 6.7 shows the variation in peak signal with accelerating mesh potential. The magnetic field strength was adjusted to give the peak signal at a cage potential of 400 volts. The predicted signal increase is observed up to an accelerating potential of 4 KV after which the signal decreases again. This decrease in signal is probably due to the collection of secondary electrons by the accelerating mesh at high positive potentials. This would result in a decrease in the number of electrons transmitted to the Everhart-Thornley detector and a consequent reduction in the detector output signal.

Because the accelerating field does not affect the energy of the electrons entering the magnetic field because of the retarding field due to the cage base potential, it is expected that the characteristic of output signal versus magnetic field at constant accelerating and cage potentials should be similar to that obtained without the accelerating mesh fitted to the detector (Figure 6.4). These curves are shown in Figure 6.8 for an accelerating potential of 4KV (corresponding to the peak of Figure 6.7) and cage base potentials of 200, 300 and 400 volts. An increase in the peak signal detected is obtained from 200 to 300 volts whereas a decrease is observed from 300 to 400 volts. This was again caused by the shadowing effect discussed in the previous section as the results were obtained at a constant value of cage base tilt angle. A broadening of the peaks at higher values of cage potential was noted, similar to that observed in section 6.3. The distortion of the leading edge of the curve obtained at 400 volts was repeatable but has not been explained. It was not evident when the specimen potential characteristics were plotted.

With a cage potential of 400 volts and an accelerating potential of 4 KV, the characteristic curves of specimen potential versus output signal were plotted on both the leading edge and the trailing edge of the peak by selecting two different values of magnetic field. Figure 6.9 shows these two character-

FIG 6.7

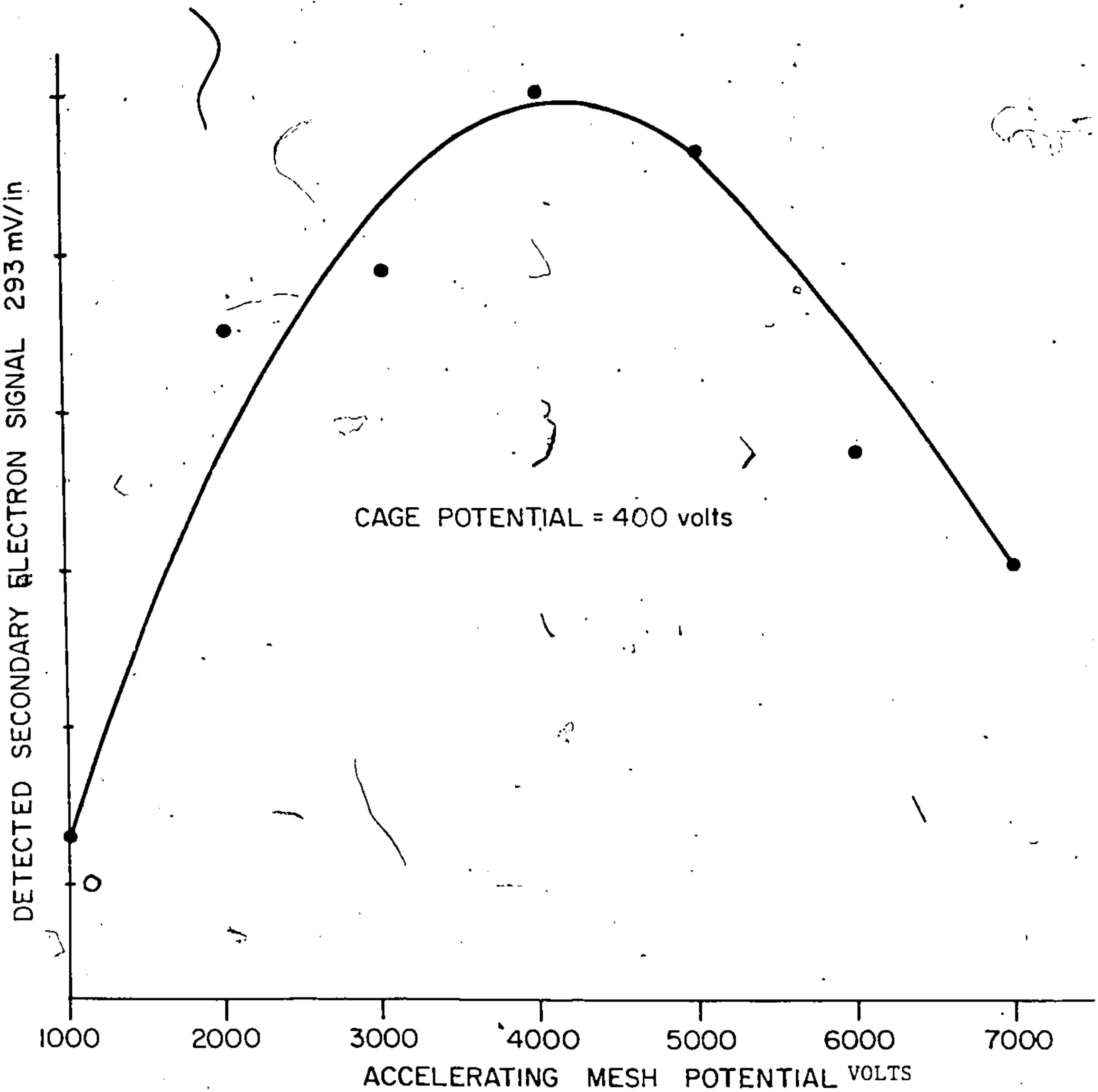
DETECTED SECONDARY ELECTRON SIGNAL 293 mV/in
CAGE POTENTIAL = 400 volts
1000
2000
3000
4000
5000
6000
7000
ACCELERATING MESH POTENTIAL VOLTS

Fig. 6.7

This graph shows accelerating mesh potential versus detected secondary electron signal.

Cage potential = 400 volts

By = 29.6 gauss

Specimen potential = 0.0 volts

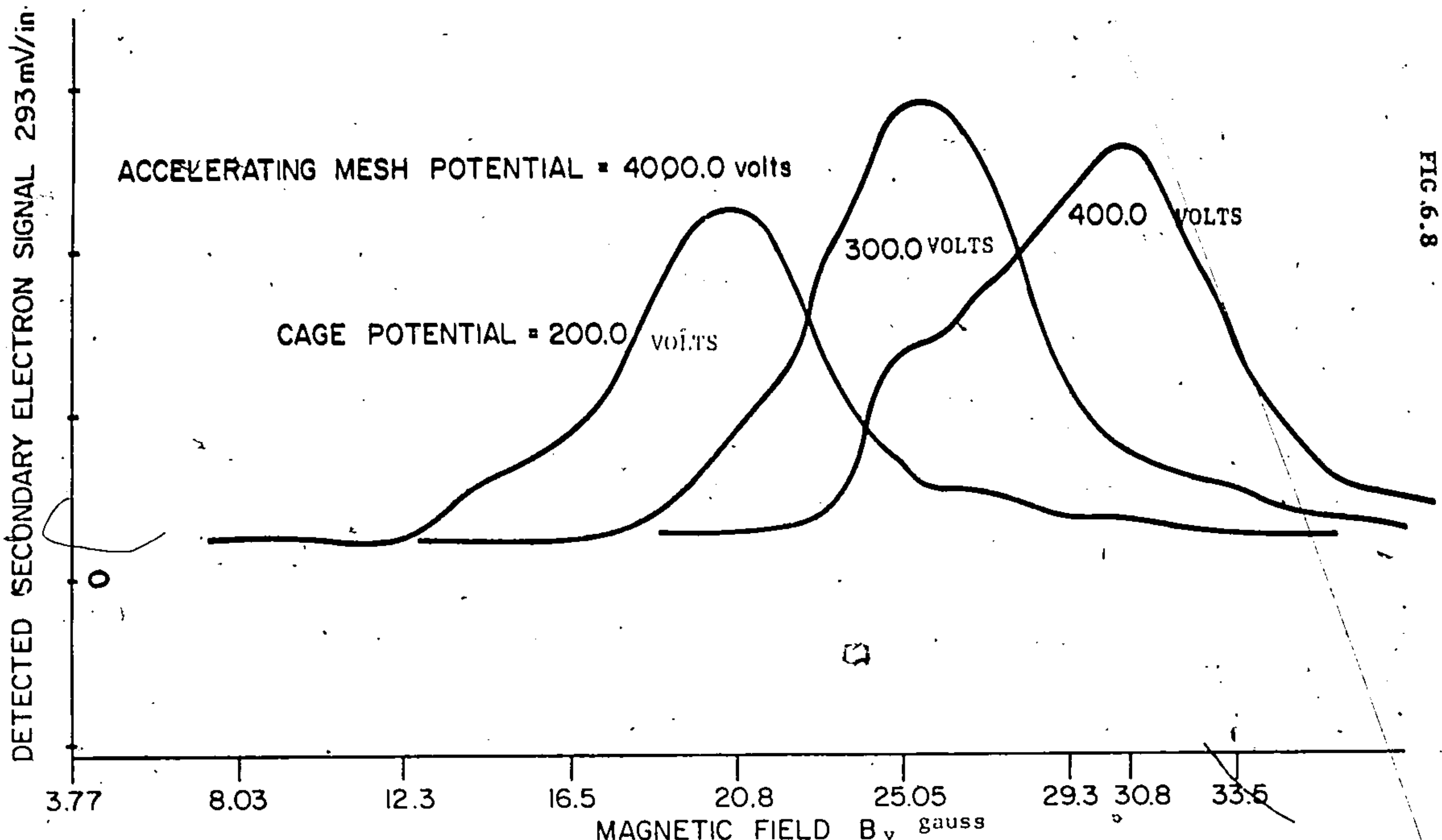
ACCELERATING MESH POTENTIAL = 4000.0 volts
CAGE POTENTIAL = 200.0 VOLTS
300.0 VOLTS
400.0 VOLTS
DETECTED SECONDARY ELECTRON SIGNAL 293 mV/in
0
3.77
8.03
12.3
16.5
20.8
25.05
29.3
30.8
33.5
MAGNETIC FIELD B y gauss

FIG 6.8

Fig. 6.8

This graph shows magnetic field By versus detected secondary electron signal with cage potential as a parameter

Accelerating mesh potential = 4000 volts.

FIG. 6.9

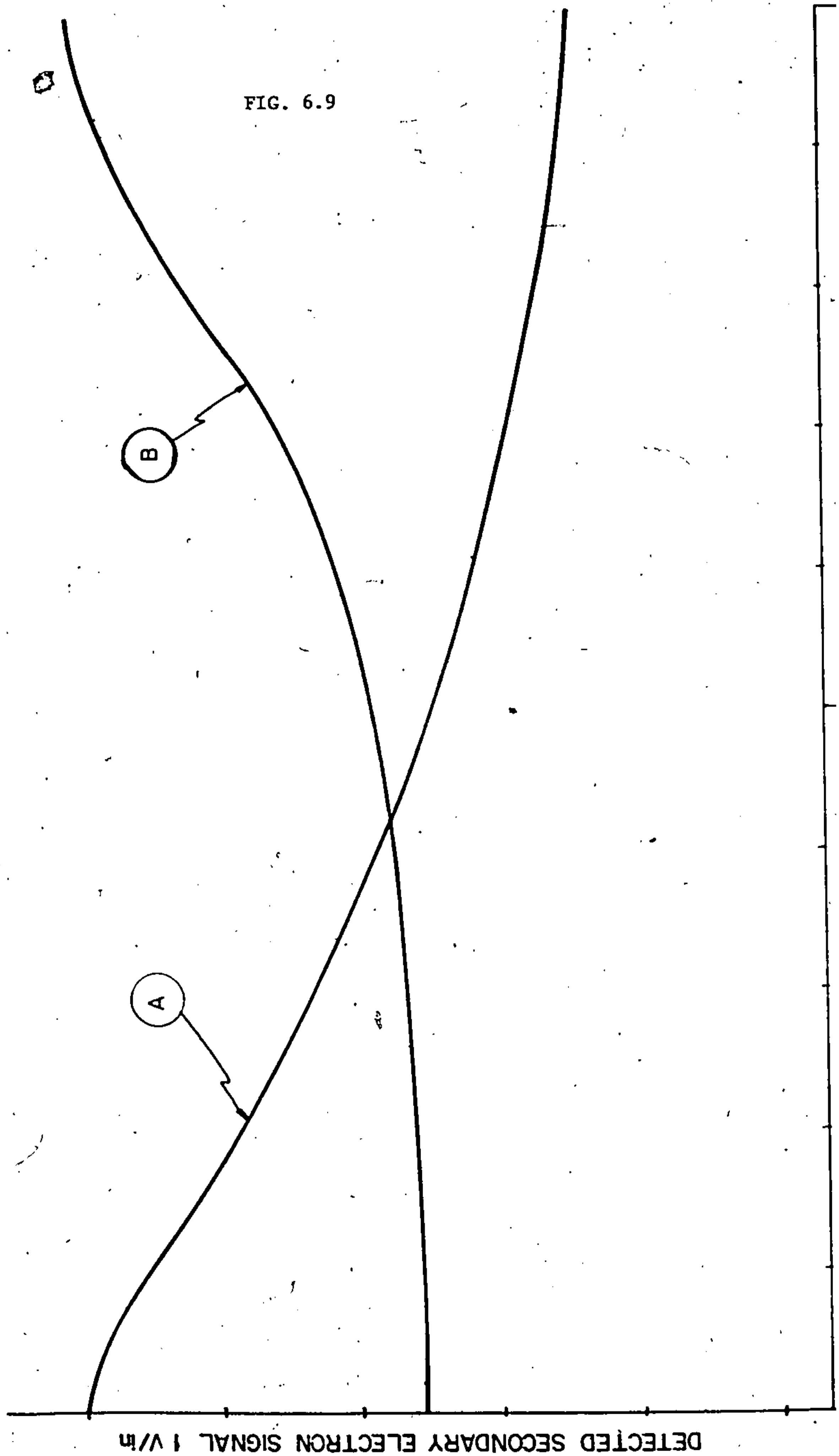

Fig. 6.9

Specimen potential Vd versus detected seondary electron signal is shown in this graph.

Accelerating mesh potential = 4000.0 volts

Cage potential = 400 volts

By $\simeq$ 9.6 gauss

Curve A) Linearity 8.5%

Range ± 20 volts

Sensitivity 110mu/volts

Curve B) Linearity 19.3%

Range ± 20 volts

Sensitivity 67.5 mu/volts

istics. Curve A, obtained from the trailing edge, yields a linearity of 8.5% over a ± 20 volt range with a sensitivity of 110 mV/volt. Curve B, obtained from the leading edge was linear to within 19.3% with a sensitivity of 67.5 mV/volt over the same range. Both curves were obtained at a beam current of 5×10^{-9} amps, and a beam energy of 20 KeV. The rise-time of the measuring system was 30μ secs and an estimated signal to noise ratio of 300 was obtained.

The effectiveness of the detector in controlling transverse field effects, may be judged from the preliminary micrographs shown in Figure 6.10. These micrographs are of a single pad on the surface of the specimen described in Chapter 5. Micrograph a) shows the pad, biased at + 20 volts with respect to the substrate and the other pads which were at ground potential, with an accelerating potential of 1KV. The shadow effect due to transverse fields is present not only at the edges of the pad but also over a large part of the surface of the pad. As the accelerating field is increased, the shadow area is reduced in micrographs b) and c) taken at an accelerating potential of 2KV and 3 KV respectively. In micrograph c), the shadow area is limited to the interface region between the pad and the substrate. In micrograph d), taken at an accelerating potential of 4 KV, the shadow region is further reduced on the left hand side of the pad, but an anomalous shadow re-appears on the right hand side of the pad, around and beneath the bonding wire. Although no detailed explanation of this effect is proposed, it seems apparent that the shadow is associated with the gross topographic change resulting from the presence of the bonding wire.

The measurements made so far in this and the previous chapter have been on an area on the specimen as close as possible to the axis of the aperature in the cage base. In order to determine the suitability of the present detector system for the measurement of surface potentials over the whole area of a specimen, the output signal versus specimen potential characteristic was

FIG. 6.10

(a)

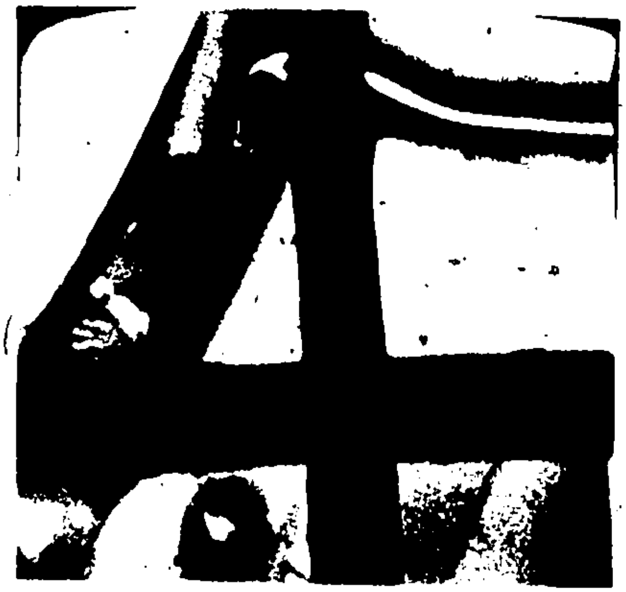

(b)

(c)

(d)

Fig. 6.10

These micrographs show the effect on a transverse field by a high accelerating mesh potential.

a) Accelerating mesh potential = 1000.0 volts

b) 2000. volts

c) 3000. volts

d) 4000. volts

measured at five different points on a specimen. The electron beam was moved 0.005" up, down, to the left and to the right of a central position and the characteristic obtained at each point. These characteristics are shown in Figure 6.11. It is apparent that a large change in the characteristic is produced by varying the measured point on the specimen surface.

The final test carried out on the detector was that of measuring unknown surface potentials. The potential on the base region of the a 2N1893 transistor shown in Figure 6.12 was varied from - 20V to + 0.5 volts and the output signal versus specimen potential characteristic was determined. The base voltage was then set at random values and the voltage set was measured by both the detector and a voltmeter. This was carried out at two different points on the base region; the results are shown in Table 6.13. The first measurement made at each point were accurate to within 4% and 1.6% respectively. A reduction in accuracy was observed with the time spent on anv measurement point. This is attributed to the interfering effects of contamination as observed by other workers (3.2).

6.4 Conclusions

The Scanning Electron Microscope offers a method of production measuring of all the potentials of a micro-electronic circuit or device without damage to the devite. In order to achieve this, a suitable SEM is needed with a voltage sensitive detector and a sophisticated instrumentation system. Surface potential measurements have been demonstrated (refs. 3.2, 3.3, 3.4, 3.5, 3.6, 3.7, 3.8, 3.9, 3.10) using commercially available SEMS, a variety of voltage contrast detectors and elementary instrumentation. However, the performance of these detectors is not sufficient to justify the development of a production system. This thesis has been concerned with the design of a prototype voltage detector which is adequate to justify the development of an overall system.

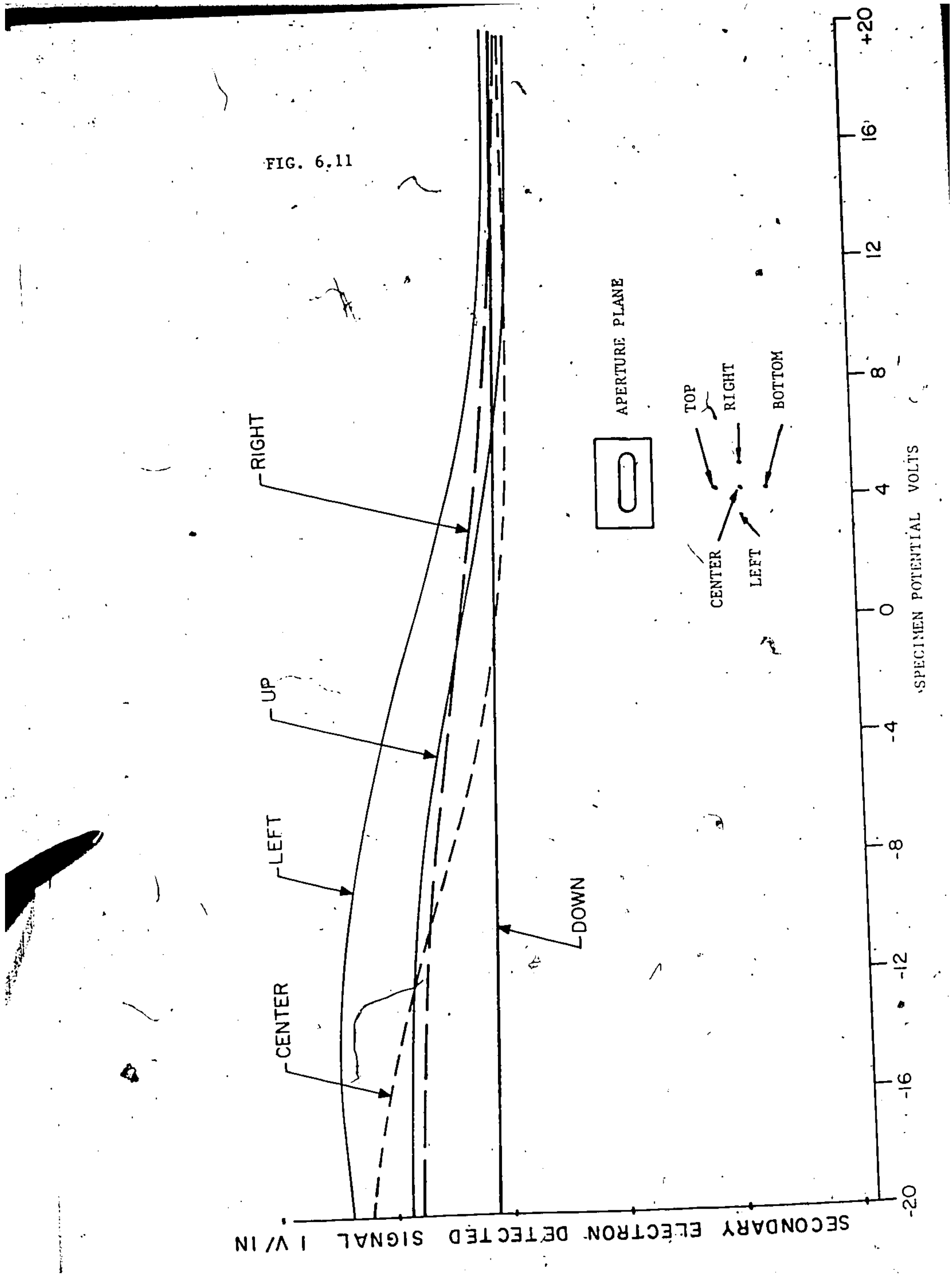

RIGHT
UP
LEFT
CENTER
DOWN
APERTURE PLANE
TOP
RIGHT
BOTTOM
CENTER
LEFT
SPECIMEN POTENTIAL VOLTS
+20
16
12
8
4
0
-4
-8
-12
-16
-20
SECONDARY ELECTRON DETECTED SIGNAL 1 V/IN

FIG. 6.11

Fig. 6.11

This graph shows specimen potential versus detected secondary electrons signal with the primary beam position as a parameter.

FIG. 6.12

TABLE 6.13

	DETECTOR	VOLTMETER
CHARACTERISTIC 1.		
	1) 9.10	9.49
	2) 13.33	15.28
CHARACTERISTIC 2.	DETECTOR	VOLTMETER
	1) 10.0	10.16
	2) 8.84	9.10
	3) 18.00	16.41

Fig. 6.12

This micrograph is of a 2N1893 transistor with the base potential set at - 5.0 volts.

Accelerating mesh potential = 4000. volts

Cage potential = 400 volts

By = 29.6 gauss

Table 6.13

These results are from the voltage measuring experiment indicating a reduction, due to beam contamination, in the measuring accuracy.

The specifications of the detector system are reviewed in Chapter 3, where it is indicated that an overall accuracy of 5% over ± 20 volts and 2 ½% over ± 2 volts is required, with provision for differential measurements of ± 50 mvolts. These figures must be available in the presence of interference of noise and other sources of contrast in the emissive mode of the SEM. In order to obtain this performance, the basic performance of the detector can be improved by electronic instrumentation techniques which improve the linearity and the rejection of unwanted signals. Although linear measurements have been demonstrated using highly non-linear devices, (refs. 3.8, 3.9), it is preferable to use a detector which is reasonably linear for a production system.

The two major sources of unwanted emissive mode signals are transverse fields and detected electrons other than those secondaries emitted from the surface of the specimen. The detector described in this thesis differs from those described in previous publications in that it employs an electron energy selector using a laterial magnetic field in addition to an accelerating electric field to suppress the effects of transverse micro-fields. The preliminary results described above have shown that such a combination of electric and magnetic fields is capable of detecting and measuring changes in specimen surface voltages and does so with a substantial improvement in linearity and sensitivity over previously published works.

The performance of the new detector can be assed by comparison with the work of Plows and Nixon (32) and Banbury and Nixon (37). Regarding linearity, it is important to make comparisons in terms of basic linearity, independent of the instrumentation system with which it is used, because the instrumentation system allows the use of feedback techniques to improve these figures. Plows and Nixon obtained a basic linearity of 12.5% over a 30 volt range where as Banbury and Nixon achieved 13% over a ± 2 volt range. The present detector has already achieved 8% and 2.5% over similar ranges. Noise measurements indicate that the detector can achieve a voltage resolution of 10 mvolts with a bandwidth of 100 kHz, with these figures being more then adequate for the system specifications. Comparative figures from the above references have not be published. Although sensitivity figures have been published, it is not possible to make a comparison of sensitivity without noise and bandwidth figures because the sensitivity is a direct function of the amplifier system associated with the detector.

There are two major areas for improvement of this detector. As indicated in Chapter 3, it is desirable that the detector be able to perform as a conventional emissive-mode detector when voltage contrast measurements are not required. The presence of the magnetic field in the primary beam path reduces the useful magnifications to about X1000 and it is apparent from the preliminary results that the areas over which voltage measurements can be made on a specimen is limited to an area with a diameter of approximately 5 mils. Both of these effects result from inhomogeneities of the magnetic field and improvements in this direction can be the subject of future development.

6.5 Suggestions for Future Work

The most obvious starting point for continuing work on the surface voltage detector is the investigation of the detailed behaviour of the system in order to arrive at the optimum operating conditions. A computer aided analysis of the shape and density distribution of the electron bundle arriving at the aperture plane would allow the optimum values of retarding field, magnetic field and aperture shape and geometry to be determined analytically rather than experimentally. Such an analysis would also help to explain the broadening of the peak widths observed with increasing values of magnetic field (Figure 6.5 and 6.9). The decrease in signal detected above an accelerating potential of 4 kV (Figure 6.7) was explained by the collection of electrons by the accelerating electrode at high positive bias. This should be verified by measuring the current collected by the accelerating mesh as a function of accelerating potential.

Further work on transverse fields is needed in order to determine the conditions under which the detector can and cannot be used to measure surface voltages with an acceptable accuracy. Limits must be placed on the size and proximity of unipotential areas on which measurements can be made as well as in the potentials of such areas.

One of the problems encountered with the present design of the detector is the power dissipation of the magnet coils. This problem could be solved and the detector simplified by the use of permanent magnets in place of the coils. Under these conditions, the detector would operate with a constant magnetic field and retarding field unless small coils were used which could either aid or oppose the permanent magnets in order to produce a change in magnetic field without large power dissipations.

As mentioned earlier (section 6.2), the detector was designed so that a retarding field energy analyser could be tested at a later date. In this case, the magnetic field would be used only to select the secondary electrons of interest. The energy analyser would then relate changes in the energy of these electrons to specimen potential changes. The first section of the detector would be operated with negative feedback to maintain a constant input to the retarding grid analyser and the aperture could be removed.

When these remaining problems have been solved and the detector further developed into its final form, then it can be incorporated into a fully instrumented production, voltage measuring system for use in the micro-electronics industry.

References

2.1 Murata, Malsunkawa, Shimizer, J.J.A.P., 10 (1971) P. 624.

2.2 Koller, Burgess, Phys. Rev. 70, 671 "Secondary Emission from Ge, Si, Bo".

2.3 Bruining, J. H., Physics, 5, 901, "Secondary Emission Part II".

2.4 Warneche, R. J., J. Physics 7, 270, "Secondary Emission of Pure Metals".

2.5 De Boer, Bruining, J. H., Physica 6, 941, "Secondary Electron Emission".

2.6 Sixtus, K., Am. Phys. Lpz., 86, 922 (1928).

2.7 Troloan, L.R. G., Prac. Phys., 49, 392 "Secondary Electron Emission from Complex Surfaces".

2.8 Knoll, M. Theile, R. Z., Phys. 113, 260, "Electron Pictures of the Structure of Surfaces and Thin Layers".

2.9 Bruining, H., Physica 3, 1045.

2.10 Bruining, H., Physica 5, 901.

2.11 Becker, A., Am. Phys. Lpz. 78, 253 (1925).

2.12 Farnsworth, H.E., Phys. Rev., 25, 41 (1925).

2.13 Raene, H. Schanerwitz, G., Z. Phys., 53, 404 (1929).

2.14 Kamaya, K., Kawakatso, H., J. Phys. P vol. 5, 1972.

2.15 Becker, A., Am. Phys. Lpz., 78, 228 (1925).

2.16 Brunsmade, J. B., Phys. Rev., 30, 94 (1972).

2.17 Amelio, G. F., Journal of Vacuum Science and Technology, Vol. 7 #6.

2.18 Everhart, T. E., Pease, S. R., Pederson Report #RTL-66-11 Electronics Research Lab, University of California, May 1966.

2.19 Oatley, C. W. Nixon, W. C., Pease, R. F. W., Advance in Elect. and Elect. Physics, 21, 181, 1965.

2.20 Thornton, P. R., "Scanning Electron Microscope" Chapman and Hall, 1968.

2.21 Everhart, T. E., Thornley, R. F. M., 1960, J. Sci. Instrum. 37, 246.

2.22 Everhart, T. E., Wells, O. C., Oatley, C. W., J. Elect. and Control 7, 97, 1959.

2.23 Shaw, D. A., Ph.D. Dissertation, University College of North Wales, 1970.

2.24 Sulway, D. V., Ph.D. Dissertation, University College of North Wales, 1968.

2.25 Thornton, P. R., Sulway, D. V., Shaw, D. A., IEEE Trans. Electron. Devices, ED-16, 360, 1969.

2.26 Shaw, D. A., Wayte, R. C., Thornton, P. R., Appl. Physics Letters, 8, 289, 1966.

2.27 Tousimes, A. J., Martin, L., "Electron Probe Microanalysis", Academic Press, 1969.

3.1 Saparin, G. V., Spivak, G. V., Sedov, W. N., Kamalova, L. F., Academy of Sciences of U.S.S.R., Physical Series 32, P. 879.

3.2 Plows, G. S., Nixon, W. C., Eng. Dept. University of Cambridge, to be published.

3.3 Flemming, J. P., Ward, E. W., Electronics Letters, 1970, Vol. 6 #1, P. 7.

3.4 Gopinath, G. A., Sanger, C. C., Journal of Physics E., Vol. 4, 1970.

3.5 Driver, M. C., Proc. SEM Symp. IIT Research Inst., Chicago, Ill. 60616.

3.6 Wells, O. C., Bremer, C. G., J. of Sci. Inst., 1968 Series 2, Vol. 1, P. 902.

3.7 Bandbury, J. R., Nixon, W. C., 1970, Proc. 3rd annual SEM Symp. Chicago, 60616.

3.8 Beaulieu, R. P., Black, T. M., Cox, C. D., Proc. IEEE Symp. on Reliability, 1971.

3.9 Black, T. M., Ma.Sc. Dissertation, University of Ottawa, 1972.

3.10 Gopinath, A., Sanger, C. C., Journal of Physics E., 2, 742-749.

3.11 Everhart, T. E., Stereoscan, Scanning Electron Microscope Colloquim, April 1970.

3.12 Peace, R. F. W., Dissertation, Cambridge University, (Ph.D.) 1964.

3.13 Rose, A., Advances in Electronics, Academic Press, 131-166, 1948.

4.1 Harman, W. H., "Electron Motion", McGraw Hill, 1953.

APPENDIX I

The Motion of Electrons in Electrostatic Fields

To completely understand the operation of the proposed detector design, an analysis of electron motion in electrostatic and magnetic fields was carried out. The basic equations used in this analysis (see Chapter 4) are developed below.

If we consider a two dimensional electric field, the differential equations governing electron motion in such a field are (A1):

$$\frac{d^2z}{dt^2} = \frac{e}{m} Ez$$

$$\frac{d^2x}{dt^2} = \frac{e}{m} Ex$$

where e is the charge of the electron and m is its mass. The field Ez is generated between the specimen surface z = 0 x = 0 and a planar electrode at $z = z_A$. The transverse field components Ex and Ey and the entrance or exit angle of the transverse field, AMF, are used with Saparin's (3.1) approximations of this field to give

$$Ex = Eo\ e^{-z/2d} \text{ Cos (AMF)}$$

$$Ez = Eo\ e^{-z/2d} \text{ Sin (AMF)}$$

where d is the separation of the two surface electrodes generating the transverse field and Eo is the strength of the transverse field at z = 0. Therefore, the equations of motion become, by substitution:

$$\frac{d^2z}{dt^2} = \frac{e}{m} (Eo\ e^{-z/2d} \text{ Sin (AMF)} + EzA) \quad (1)$$

$$\frac{d^2x}{dt^2} = \frac{e}{m} Eoe^{-z/2D} \text{ Cos (AMF)} \quad (2)$$

These differential equations may be solved using a digital computer and a special purpose programming language known as an analogue simulator. The programme used is SL-1 which was prepared by Xerox to operate on their Sigma 7 computers.

The primary function of the language is the solution of sets of ordinary or partial differential equations. The first step in setting up an SL-1 program is to describe the system to be simulated in terms of equations representing the system events. The differential equations developed in this section serve that purpose. The dynamic functioning of the described system is simulated by repeated digital integration of the system equations. The repetition rate is specified in terms of an increment of the independent variable t.

Explicit structure blocks of the SL-1 program of major interest are the Initial, Dynamic and Terminal regions. The Initial region contains statements for initializing the simulation, and for information that is to be fed out once at the beginning of the simulation run only. The Dynamic region is where the actual simulation takes place. It contains two types of substructure, the derivative and the parallel sections. Each derivative section contains only simulation equations that are to be integrated with the same algarithms and integration step size. There may be as many derivative sections as there are algarithms and step sizes used. The parallel sections contain other simulation equations that do not require integration. In the terminal section, tests, which determine if the specified simulation goals have been fulfilled are executed. If these tests fail, the program returns to the dynamic region and starts a new pass through this region. When the tests are passed, the program will proceed to the terminal region where the necessary wrap-up operations are performed.

The SL-1 program written to simulate electron trajectories in electrostatic fields is shown in this appendix. The differential equations derived are included in the Dynamic section with the following initial conditions supplied.

$$ZDI = \left.\frac{dZ}{dt}\right|_{t=0} = VZ = 5.93 \times 10^5 \sqrt{\text{Electron Emission Energy}}\ \text{Sin (angle of electron emission)}$$

$$XDI = \left.\frac{dx}{dt}\right|_{t=0} = Vx = 5.93 \times 10^5 \sqrt{\text{Electron Emission Energy}}\ \text{Cos (Angle of electron emission)}$$

$$XI = x\Big|_{t=0}^{t\,=\,0}$$

APPENDIX 2

The Motions of Electron in a Magnetic Field

The differential equations governing the motion of an electron in a magnetic field may be developed from equations 4.4 in Harman (A2-1) (if Bz and Bx are equal to zero) to be

$$\frac{d^2x}{dt^2} = -\frac{e}{m}\left(+ By \frac{dz}{dt}\right) \tag{1}$$

$$\frac{d^2y}{dt^2} = 0 \tag{2}$$

$$\frac{d^2Z}{dt^2} = -\frac{e}{m}\left(- By \frac{dx}{dt}\right) \tag{3}$$

where e is the charge on the electron and m is its mass.

Multiplying Eq. 1 by dt and integrating gives:

$$\frac{dx}{dt} = -\frac{e\ By}{m} Z + C \tag{1'}$$

where C may be evaluated from the initial condition that

$$\frac{dx}{dt} = Vx \qquad (t = 0\ z = 0) \tag{A2-1}$$

Therefore C = Vx and equations may now be substituted into equation 3 to give

$$\frac{d^2z}{dt^2} = -\frac{e}{m}\left(+By^2\frac{e}{m} Z - By\ Vx\right) \tag{3'}$$

$$\frac{d^2z}{dt^2} + \left(\frac{e}{m}\ By\right)^2 Z = +\frac{e}{m} By\ Vx)$$

One solution obvious by inspection is:

$$Z = +\frac{Vx}{By}\left(\frac{m}{e}\right)$$

However, any solution of the characteristic equation of 3'

$$\frac{d^2z}{dt^2} + \left(\frac{e}{m} By\right)^2 Z = 0 \tag{4}$$

may be added to this and the sum will also be a solution of Eq. 3'. The solutions of Eq. 4 are trignometric functions and hence the total solution including the constants is:

$$Z = C_1 \cos \frac{eBy}{m} t + C_2 \text{ Sin } \frac{eBy}{m} t + \frac{Ux}{By} \left(\frac{m}{e}\right) \qquad (5)$$

The constants C_1 and C_2 may be evaluated using the initial conditions that $Z\Big|_{t=0} = 0$ and $\frac{dz}{dt}\Big|_{t=0} = U$: The constants are

$$C_1 = \frac{-m}{e} \frac{Ux}{By} \quad \text{and} \quad C_2 = + \frac{m\ Uz}{e\ By}$$

Therefore Eq. (5) becomes

$$Z = - \frac{m}{e} \frac{Ux}{By} \text{ Cos } \frac{eBy}{m} t + \frac{m}{e} \frac{Uz}{By} \text{ Sin } \frac{eBy}{m} t + \frac{Ux}{By} \left(\frac{m}{e}\right) \qquad (5')$$

Substituting Eq. 5' into equation 3', integrating with respect to t and applying the initial conditions that $x\Big|_{t=0} = 0$, the equation for x is obtained as follows

$$x = \frac{-e}{m} \text{ UxBy Sin } \frac{e}{m} \text{By } t \ \frac{-e}{m} \text{ UxBy Cos } \frac{e}{m} \text{Byt} + \frac{mUz}{eBy}$$

Equation 2 may be simply integrated twice and by applying the conditions that

$\frac{dy}{dt}\Big|_{t=0} = Uy$ and $y\Big|_{t=0} = 0$ we obtain:

$$y = Vyt$$

Therefore, the final equations are:

$$x = - \frac{e}{m} \text{ VxBy Sin} \frac{e}{m} \text{ Byt } \frac{-e}{m} \text{ Vz Cos } \frac{e}{m} \text{ Byt} \pm \frac{mVz}{eBy}$$

$$y = Vyt$$

$$Z = - \frac{m}{e} \frac{Vx}{By} \text{ Cos } \frac{eBy}{m} t + \frac{m}{e} \frac{Vz}{By} \text{ Sin } \frac{eBy}{m} t + \frac{Vx}{By} \left(\frac{m}{e}\right)$$

The values of the parameters Vx, Vy and Vz may be determined from the energy of the electrons and the angle of entrance of the electron when it enters the magnetic field using the expressions:

$$Vx = 5.93 \times 10^5 * \sqrt{\text{Electron Energy}} * \text{Cos}(\beta) * \text{Cos}(\alpha)$$
$$Vy = 5.93 \times 10^5 * \sqrt{\text{Electron Energy}} * \text{Cos}(\beta) * \text{Sin}(\alpha)$$
$$Vz = 5.93 \times 10^5 * \sqrt{\text{Electron Energy}} * \text{Sin}(\beta)$$

where the coordinate system is described with the aid of Figure A2.

A2-1 W. W. Harman "Electronic Motion" McGraw Hill, 1953.

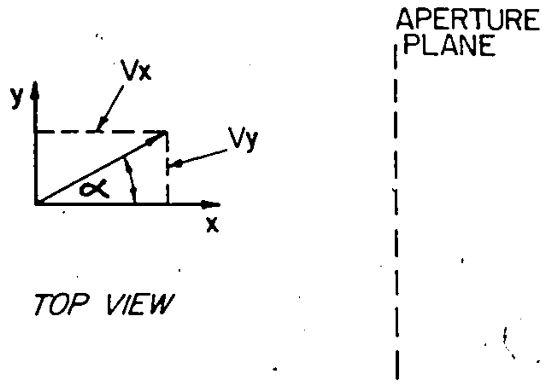

TOP VIEW

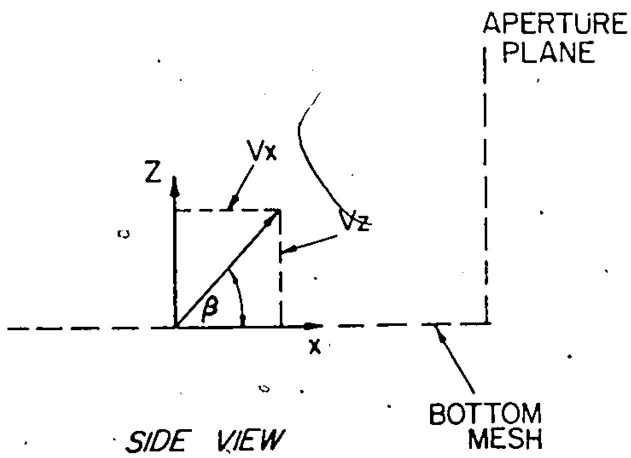

SIDE VIEW

A VOLTAGE CONTRAST DETECTOR FOR USE IN THE SCANNING ELECTRON MICROSCOPE

Abstract

The Scanning Electron Microscope in its secondary electron emissive mode can be used to measure surface potentials of micro-electronics devices if unwanted signals can be suppressed and monotisity achieved. The thesis describes the design of an energy selective detector, which achieves a high degree of suppression of unwanted signals, a basic linearity of 8% over a ±20 volts range and a resolution of 10 mvolts with a bandwidth of 100K Hz.

T.M. Black